

AD 653723

CHEMICAL PHYSICS OF SURFACE REACTIONS OF METALS

Earl A. Gulbransen  
Richard L. Tallman

Westinghouse Research Laboratories  
Pittsburgh, Pennsylvania 15235

FINAL REPORT

Contract: Nonr-4949(00)

May 31, 1967

Period Covered: June 1, 1965 to May 31, 1967

Office of Naval Research  
Material Sciences Division  
Washington, D. C. 20360

For public use; its  
distribution is unlimited.

ARCHIVE COPY

DDC  
RECEIVED  
JUN 27 1967  
B

ACCESSION for		
OPSTI	WHITE SECTION <input checked="" type="checkbox"/>	
DDC	GRAY SECTION <input type="checkbox"/>	
UNANNOUNCED	<input checked="" type="checkbox"/>	
JUSTIFICATION <i>per file can</i>		
BY		
DISTRIBUTION/AVAILABILITY CODES		
DIST.	AvAIL.	and/or SPECIAL
1		

REPRODUCTION IN WHOLE OR IN PART IS PERMITTED  
FOR ANY PURPOSE OF THE UNITED STATES GOVERNMENT

This research was sponsored by the Office of  
Naval Research, Material Sciences Division,  
under Contract Number Nonr-4949(00), Req. No.  
NR-036-0641.

CHEMICAL PHYSICS OF SURFACE REACTIONS OF METALS

Earl A. Gulbransen  
Richard L. Tallman

Westinghouse Research Laboratories  
Pittsburgh, Pennsylvania 15235

FINAL REPORT

Contract: Nonr-4949(00)

May 31, 1967

Period Covered: June 1, 1965 to May 31, 1967

Office of Naval Research  
Material Sciences Division  
Washington, D. C. 20360

## CHEMICAL PHYSICS OF SURFACE REACTIONS OF METALS

Earl A. Gulbransen  
Richard L. Tallman

Westinghouse Research Laboratories  
Pittsburgh, Pennsylvania 15235

### ABSTRACT

A survey is made of studies at the Westinghouse Research Laboratories on the structure of oxide films and the formation of localized oxide growths on iron. Special attention is given to the recent studies using selected-area electron diffraction to determine the morphological structures characteristic of oxide whiskers and pointed blade-like oxide platelets.

Filamentary whisker growths are formed when iron is oxidized in dry oxygen at 400° to 500°C. Long, blade-like platelets are formed at 450°C in atmospheres containing both water vapor and a trace of oxygen. The oxide whiskers and the blade-like platelets produce fiber-texture patterns showing exclusively  $\alpha\text{-Fe}_2\text{O}_3$  diffraction and a  $[\bar{1}\bar{1}20]$  fiber axis. Selected-area diffraction patterns of individual growths show the same fiber axis and indicate (1) that the most simple whiskers have a single axial screw dislocation, and (2) that the blades are twinned on the blade-face plane,  $(\bar{1}101)$ .

Growth mechanisms based on easy paths for diffusion along the axial dislocation in the oxide whisker and along the twin plane in the oxide blade-like platelet are proposed. Some calculations relevant to the internal diffusion mechanism in whiskers are presented.

## TABLE OF CONTENTS

	<u>Page</u>
Abstract . . . . .	1
Table of Contents . . . . .	ii
List of Figures. . . . .	v
List of Tables . . . . .	vi
1. Purpose . . . . .	1
2. Thermochemical Analyses . . . . .	2
3. Oxide Nucleation . . . . .	6
3.1 Thin Film Range - Normal Pressure . . . . .	6
3.2 Thin Film Range - Low Oxygen Pressure. . . . .	7
3.3 Orientation of Oxide Films on Iron. . . . .	9
3.4 Picture of Initial Oxide Formation. . . . .	9
4. Phenomenological Studies on Oxide Whiskers and Platelets .	11
4.1 Introduction . . . . .	11
4.2 Oxide Whiskers . . . . .	12
4.3 Pointed Blade-Shaped Oxide Platelets . . . . .	17
4.4 Reaction with Pure Water Vapor . . . . .	19
4.5 Mechanism of Oxide Platelet Formation. . . . .	21
4.6 Study of the $O_2/H_2O$ Ratio . . . . .	21
4.7 Rounded Oxide Platelets . . . . .	22
4.8 Blunted Blade-Shaped Oxide Platelets . . . . .	24
5. Studies Using Selected-Area Electron Diffraction. . . . .	27
5.1 Introduction . . . . .	27
5.2 Oxide Whiskers . . . . .	28
5.2.1 Analyses of Single Oxide Whisker Patterns . .	28
5.2.2 Analyses of Streaked Reflections . . . . .	31
5.2.3 Axial Twist Calculation . . . . .	34
5.2.4 Strain Energy of a Whisker . . . . .	35

	<u>Page</u>
5.2.5 Diffraction from a Rod with an Axial Screw Dislocation. . . . .	35
5.2.6 Comparison with Earlier Work . . . . .	35
5.3 Pointed Blade-Shaped Platelets. . . . .	36
5.3.1 Morphological Description . . . . .	36
5.3.2 Analyses of Selected-Area Diffraction Patterns . . . . .	38
5.3.3 Discussion of Platelet Morphology . . . . .	46
5.3.4 Anomalous Diffraction . . . . .	48
5.3.5 Comparison with Earlier Work . . . . .	49
5.3.6 Novel Character of $\alpha$ -Fe <sub>2</sub> O <sub>3</sub> Platelet Structure . . . . .	50
6. Transport Mechanisms of Localized Growths. . . . .	51
6.1 Arguments for Internal Diffusion . . . . .	51
6.2 Growth Rates. . . . .	52
6.3 Growth of Whiskers with Axial Screw Dislocations. .	53
6.3.1 Estimation of the Diffusion Coefficient for Axial Diffusion in Whiskers . . . . .	53
6.3.2 Comparison with Measured Diffusion Coefficients for Iron in $\alpha$ -Fe <sub>2</sub> O <sub>3</sub> . . . . .	57
6.3.3 Comparison with Diffusion Coefficients in Other Materials . . . . .	58
6.3.4 Consideration of Radial Growth by Lattice Diffusion. . . . .	59
6.4 Transport Mechanisms for Blade-Like Platelet Growth.	63
7. Summary of Information on Growth Morphology and Mechanisms. . . . .	65
8. High Vacuum System Development . . . . .	67
9. Replica Development . . . . .	69
10. Appendices	
I. Geometry of Whiskers on a Wire . . . . .	70
II. $\alpha$ -Fe <sub>2</sub> O <sub>3</sub> Crystal Structure . . . . .	74
III. $\alpha$ -Fe <sub>2</sub> O <sub>3</sub> Unit Cells . . . . .	77

	<u>Page</u>
IV. Transformation of Indices. . . . .	80
V. Interfacial and Other Angles in $\alpha\text{-Fe}_2\text{O}_3$ . . . .	83
VI. Systematic Absences in the Diffraction from $\alpha\text{-Fe}_2\text{O}_3$ . . . . .	85
VII. List of Interplanar Spacings. . . . .	87
VIII. Intensities and d-spacings for Selected Iron Oxides . . . . .	91
IX. Whisker Geometry--Screw Dislocation in a Rod .	96
X. Strain Energy of a Whisker . . . . .	100
XI. Diffraction from a Rod with an Axial Screw Dislocation. . . . .	102
XII. Driving Forces for Iron Diffusion in $\alpha\text{-Fe}_2\text{O}_3$ Growth. . . . .	104
XIII. Relationship Between the Fick's Law Diffusion Coefficient and the Mobility. . . . .	108
XIV. Radial Diffusion Through the Wall of an Infinitely Long Right Circular Cylindrical Pipe with a Constant Free Energy Difference and Radial Growth - Whisker Growth. . . . .	110
11. References. . . . .	113

# LIST OF FIGURES

	<u>Page</u>
1. Oxidation mechanism. . . . .	10
2. Stress corrosion reactor system. . . . .	13
3. Specimen types. . . . .	14
4. Fine oxide whiskers . . . . .	16
5. Blade-shaped oxide platelets. . . . .	18
6. Rounded oxide platelets . . . . .	23
7. Blunted blade-shaped oxide platelets . . . . .	25
8. Effect of electron beam heating on blunted blade-shaped oxide platelets. . . . .	26
9. Selected-area electron diffraction, $\alpha$ -Fe <sub>2</sub> O <sub>3</sub> whisker . .	29
10. Twist of unbent $\alpha$ -Fe <sub>2</sub> O <sub>3</sub> whisker results in streaked 2nd layer line . . . . .	32
11. Pointed blade-like platelets. . . . .	37
12. Electron diffraction, pointed blade-like platelets . .	37
13. Selected-area electron diffraction of $\alpha$ -Fe <sub>2</sub> O <sub>3</sub> platelets.	40
14. Selected-area electron diffraction of $\alpha$ -Fe <sub>2</sub> O <sub>3</sub> platelets.	41
15. Selected-area electron diffraction of $\alpha$ -Fe <sub>2</sub> O <sub>3</sub> platelets.	42
16. Platelet diffraction and image tip angle. . . . .	44
17. $\alpha$ -Fe <sub>2</sub> O <sub>3</sub> pointed blade-like platelet morphology. . . .	47
18. Model of whisker growth. . . . .	54
19. High vacuum system for H <sub>2</sub> O-O <sub>2</sub> oxidation. . . . .	68
20. Whiskers on a wire. . . . .	71
21. $\alpha$ -Fe <sub>2</sub> O <sub>3</sub> unit cells . . . . .	79
22. Lattice distortion by single screw dislocation in a cylindrical rod. . . . .	97



# LIST OF TABLES

	<u>Page</u>
1. Thermochemical Calculations, Iron-Oxygen and Iron-Water Vapor Reactions. . . . .	3
2. Thermochemical Calculations, Interoxide Equilibria . . .	4
3. Interplanar Spacings, Whisker Growths on Iron Reacted with Dry O <sub>2</sub> . . . . .	17
4. Summary of Data on Oxide Whiskers. . . . .	19
5. Summary of Data, Pointed Blade-Shaped Oxide Platelets . .	20
6. Summary of Data, Rounded Oxide Platelets . . . . .	22
7. $\alpha$ -Fe <sub>2</sub> O <sub>3</sub> d-values, Intensities, and Indices. . . . .	39
8. Diffusion Coefficient Data from Hauffe . . . . .	60
9. Radial Growth by the Lattice Diffusion of Iron. . . . .	61
10. Crystallographic Data for $\alpha$ -Fe <sub>2</sub> O <sub>3</sub> . . . . .	76
11. Transformation of Indices for Lattice Planes . . . . .	82
12. $\alpha$ -Fe <sub>2</sub> O <sub>3</sub> Angles. . . . .	84
13. $\alpha$ -Fe <sub>2</sub> O <sub>3</sub> Interplanar Spacings . . . . .	88
14. $\alpha$ -Fe <sub>2</sub> O <sub>3</sub> Useful Hexagonal Dimensions . . . . .	90
15. Diffraction Data for FeO, Fe <sub>3</sub> O <sub>4</sub> , $\gamma$ -Fe <sub>2</sub> O <sub>3</sub> , and $\alpha$ -Fe <sub>2</sub> O <sub>3</sub> . .	92

## 1. PURPOSE

The discovery of oxide nuclei<sup>1,2</sup> and of oxide whiskers<sup>3,4</sup> and platelets<sup>5</sup> growing during the oxidation of many metals came as a surprise to many workers in the field of oxidation and corrosion. The picture of oxidation of metals assumed the presence of a uniform, coherent oxide film with the reaction occurring by the diffusion of oxygen or metal through lattice defects in the oxide. Dislocations, stress, and impurity atoms in the metal lattice were not considered in the theory.

The formation of sub-microscopic growths such as oxide nuclei and oxide whiskers and platelets suggests that the simple picture is not complete. Increasingly more powerful techniques provide for the investigation of the small-scale structures of metals and oxide films. The information to be obtained includes crystal shape and orientation, stress, dislocation structure, fault and twin planes, and impurity distribution and precipitates in the metal and oxide lattices. These factors can have important effects on oxidation and other surface reactions. Some of these factors may cause localized corrosion which is important in the technical application of metals and alloys.

The availability of oxide nuclei and oxide whiskers and platelets for study by electron diffraction and by electron microscopy makes possible a determination of some of the structural and kinetic details of their growth mechanisms. Results on these growths may be carried over to a study of the general oxidation mechanism. In particular, the kinetics of metal and oxygen transport through oxide lattices and through well-defined crystal imperfections can be studied by the use of localized crystal growths.

## 2. THERMOCHEMICAL ANALYSES

Thermochemical calculations are useful as a guide in discussing the oxidation reactions of iron in oxygen and in water vapor. The existence of the oxides, the sequence of oxides in the oxidation process, and the diffusion of iron or oxygen across an oxide film or oxide crystal depend on the thermochemical equilibrium values for the free energies of the particular oxides involved.

Thermochemical equilibrium does not exist for a metal undergoing oxidation. The reactions which do occur are those that are thermochemically and kinetically feasible. Conditions approaching equilibrium may exist at certain interfaces after the rapid period of the initial oxidation reaction. Thus, the concentrations of iron in ferrous oxide at the Fe-FeO interface, at the FeO-Fe<sub>3</sub>O<sub>4</sub> interface, and at the Fe<sub>3</sub>O<sub>4</sub>-Fe<sub>2</sub>O<sub>3</sub> interface may be estimated from thermochemical data and the iron-oxygen phase diagram.<sup>6</sup>

Thermochemical calculations are made for the five equilibria involved in the reaction of iron with oxygen and water vapor using data from the JANAF tables.<sup>7</sup> The equilibrium data are expressed in terms of  $\log_{10} K$  where  $K$  is the equilibrium constant and  $\log_{10} P_{O_2}$  where  $P$  is the pressure of oxygen gas in atmospheres. Wustite "Fe<sub>0.947</sub>O" is used in all of the calculations for ferrous oxide.

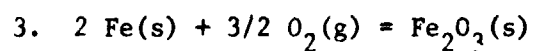
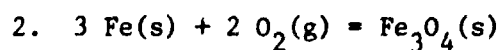
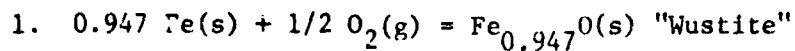
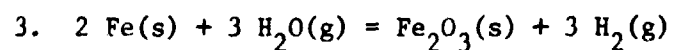
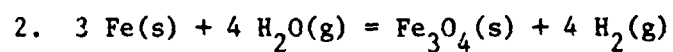
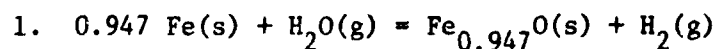
Tables 1 and 2 show the reactions together with the equilibrium calculations. Low equilibrium oxygen pressures are found over the temperature range of 298°K to 1300°K. The direct water vapor-metal reactions are not as favorable as the direct oxidation reactions.

Table 2 shows that both the reduction of Fe<sub>2</sub>O<sub>3</sub> with Fe to form Fe<sub>3</sub>O<sub>4</sub> and the oxidation of Fe<sub>3</sub>O<sub>4</sub> to form Fe<sub>2</sub>O<sub>3</sub> are thermodynamically

TABLE 1

## THERMOCHEMICAL CALCULATIONS

## Iron-Oxygen and Iron-Water Vapor Reactions

A. Direct Reactions with  $O_2(g)$ B. Direct Reactions with  $H_2O(g)$ 

Temp °K	Reactions					
	$A_1$ $-\log P_{O_2}$	$A_2$ $-\log P_{O_2}$	$A_3$ $-\log P_{O_2}$	$B_1$ $\log K$	$B_2$ $\log K$	$B_3$ $\log K$
298	85.89	89.13	86.84	2.90	18.06	10.12
400	62.18	64.15	62.31	1.85	11.33	5.75
500	48.34	49.56	47.99	1.28	7.57	3.32
600	39.16	39.87	38.47	0.95	5.21	1.80
700	32.60	32.98	31.69	0.72	3.63	0.79
800	27.70	27.85	26.63	0.66	2.54	0.07
900	23.89	23.88	22.70	0.45	1.76	-0.44
1000	20.84	20.71	19.58	0.36	1.17	-0.82
1100	18.33	18.11	17.02	0.28	0.69	-1.13
1200	16.24	15.94	14.88	0.22	0.29	-1.38
1300	14.46	14.11	13.07	0.17	-0.039	-1.59

TABLE 2

## THERMOCHEMICAL CALCULATIONS

## Interoxide Equilibria

C.  $\text{Fe}_3\text{O}_4 - \text{Fe}_2\text{O}_3$ 

1.  $4 \text{Fe}_2\text{O}_3(\text{s}) + \text{Fe}(\text{s}) = 3 \text{Fe}_3\text{O}_4(\text{s})$
2.  $2 \text{Fe}_3\text{O}_4(\text{s}) + 1/2 \text{O}_2(\text{g}) = 3 \text{Fe}_2\text{O}_3(\text{s})$
3.  $2 \text{Fe}_3\text{O}_4(\text{s}) + \text{H}_2\text{O}(\text{g}) = 3 \text{Fe}_2\text{O}_3(\text{s}) + \text{H}_2(\text{g})$

D.  $\text{FeO} - \text{Fe}_3\text{O}_4$ 

1.  $\text{Fe}_3\text{O}_4(\text{s}) + 0.788 \text{Fe}(\text{s}) = 4 \text{Fe}_{0.947}\text{O}(\text{s})$
2.  $3.17 \text{Fe}_{0.947}\text{O} + 0.415 \text{O}_2(\text{g}) = \text{Fe}_3\text{O}_4(\text{s})$
3.  $3.17 \text{Fe}_{0.947}\text{O} + 0.83 \text{H}_2\text{O}(\text{g}) = \text{Fe}_3\text{O}_4(\text{s}) + 0.83 \text{H}_2(\text{g})$

E.  $\text{Fe}_{0.947}\text{O} - \text{Fe}_2\text{O}_3 - \text{Fe}_3\text{O}_4$ 

1.  $1.19 \text{Fe}_{0.947}\text{O}(\text{s}) + 0.937 \text{Fe}_2\text{O}_3(\text{s}) = \text{Fe}_3\text{O}_4(\text{s})$

Results of Calculations  
Reactions

Temp °K	$C_1$ $\log_{10} K$	$C_2$ $-\log_{10} P_{\text{O}_2}$	$C_3$ $\log_{10} K$	$D_1$ $\log_{10} K$	$D_2$ $-\log P_{\text{O}_2}$	$D_3$ $\log_{10} K$	$E_1$ $\log_{10} K$
298	13.71	68.57	-5.76	-6.46	101.49	8.87	5.09
400	11.00	47.64	-5.42	-3.93	71.67	5.47	3.71
500	9.44	35.41	-5.18	-2.44	54.23	3.50	2.92
600	8.43	27.22	-5.02	-1.42	42.58	2.21	2.38
700	7.76	21.34	-4.91	-0.77	34.46	1.37	2.03
800	7.32	16.87	-4.86	-0.29	28.41	0.76	1.79
900	7.04	13.31	-4.84	+0.05	23.79	0.32	1.62
1000	6.81	10.50	-4.81	+0.26	20.39	0.11	1.51
1100	6.59	8.23	-4.77	+0.45	17.26	-0.21	1.41
1200	6.40	6.34	-4.73	+0.59	14.82	-0.40	1.32
1300	6.24	4.76	-4.69	+0.70	12.77	-0.56	1.25

avored.  $\text{Fe}_3\text{O}_4$  is not oxidized in appreciable amounts by  $\text{H}_2\text{O}(\text{g})$  to  $\text{Fe}_2\text{O}_3$  at any temperature unless hydrogen is removed.

Table 2 shows  $\text{Fe}_3\text{O}_4$  can be reduced by Fe to form  $\text{Fe}_{0.947}\text{O}$  only below 873°K (600°C).  $\text{Fe}_{0.947}\text{O}$  can be oxidized by  $\text{O}_2$  to form  $\text{Fe}_3\text{O}_4$  at all temperatures. In the absence of iron and oxygen  $\text{Fe}_3\text{O}_4$  can form from  $\text{Fe}_{0.947}\text{O}$  and  $\text{Fe}_2\text{O}_3$  at all temperatures.

The calculations given here do not take into account the non-stoichiometric compositions of the oxides. Variations in composition occur depending upon the presence of other phases and the temperature. The equilibria data given here present only the approximate values calculated from readily available thermodynamic data.<sup>7</sup>

### 3. OXIDE NUCLEATION

#### 3.1 THIN FILM RANGE - NORMAL PRESSURE

Micro-structural studies of gas-metal reaction became possible with the development of the electron microscope in the late 1930's and early 1940's. We define the micro-structure of oxide films by the following factors: (1) crystal structure, (2) crystal size and habit, (3) crystal orientation relative to the metal, (4) presence of twins, dislocations and other defects, and (5) presence of stress in the metal-oxide system.

Visual and optical microscopic observations of surface reactions are the oldest methods for the study of the chemical activity of surfaces. Catalysis and corrosion scientists have long recognized that certain sites on surfaces were especially reactive. However, the nature of these reaction sites commonly remains undetermined because of lack of resolving power of their techniques and the difficulties inherent in defining the surface and the chemical environment at the surface.

In the field of oxidation, Phelps, Gulbransen, and Hickman<sup>8</sup> reviewed the literature in 1946 on the micro-structure of oxide films on the common metals. An extensive electron-optical study was made also on the micro-structure of thin oxide films formed on a number of the common metals including iron, nickel, iron-based alloys, and stainless steels. Several of the results will be mentioned.

The oxidation of iron at 250°C in dry oxygen for 30 minutes produced a continuous oxide film consisting of irregularly-shaped oxide crystals 500 to 1500 Å in size.

These crystals were partially oriented to the metal. Transmission and reflection electron diffraction analyses of the oxides show the spinel,  $\text{Fe}_3\text{O}_4$ , and hexagonal  $\alpha\text{-Fe}_2\text{O}_3$  were formed. Nickel

oxidized at 500°C for 20 minutes showed a micro-structure similar to that found on iron at 250°C. The oxide film was NiO which was nearly randomly oriented to the metal.

We concluded in 1946 that most metals oxidized at temperatures of 200° to 500°C at 0.1 to 1 atm oxygen pressure formed granular oxide films for oxide thicknesses which could be studied at that time by electron-optical methods, i.e. about 500 Å. The films contained thicker and thinner sections indicating a multilayer structure. Oxide crystals were nucleated on the initial metal surface covered by the room temperature oxide film and on top of the first layer of oxide crystallites.

The oxide crystals 500 to 1800 Å in breadth mentioned above are much smaller than the metal grains. The surface density of such crystals is large, about  $10^{10} \text{ cm}^{-2}$ .

The crystal size was a function of both time and temperature. Some evidence was found for preferred orientation of the oxide crystallites although many oxide films showed no preferred orientation with respect to the metal grain. We concluded that most oxide films were not uniform in crystal thickness.

### 3.2 THIN FILM RANGE - LOW OXYGEN PRESSURES

The oxide nucleation processes were found to be a function of pressure in the early 1950's by Bardolle and Bénard.<sup>1</sup> These workers studied the initial stage of oxide formation on carefully annealed and electropolished ARMCO iron between 650° and 850°C in vacuums of  $10^{-1}$  to  $10^{-3}$  torr. At pressures between  $10^{-1}$  and  $10^{-2}$  torr at 850°C many oriented oxide crystals were formed on an individual metal grain. Under none of the conditions studied was the oxide on the surface of the metal in the form of one single crystal. However, the ensemble of oxide crystals on each metal grain had a definite crystal pattern which suggested a definite orientation of the crystals to the metal grain. For this oxidation condition the oxide crystals were much thicker than those studied by Gulbransen and Hickman at lower temperatures.



At pressures of  $10^{-2}$  to  $10^{-3}$  torr only a few well-oriented oxide nuclei were formed. The shapes of the individual crystallites could then be studied and were found to depend on the orientation of the metal crystals. The space between the oxide crystallites was occupied by a thin film of randomly-oriented oxide crystals.<sup>9</sup>

Gulbransen, McMillan, and Andrew<sup>2</sup> extended the studies of Bardolle and Bénard.<sup>1</sup> Electron-optical methods were used and the oxide crystals formed during oxidation were covered with a thin plastic film and removed electrochemically from the metal. A high purity iron was used and the oxidation conditions were carefully controlled. A vacuum microbalance was used to determine the extent of reaction.

An electron micrograph of the oxide stripped from an iron specimen oxidized at 850°C to an average thickness of 752 Å at a pressure of  $2 \times 10^{-3}$  torr of oxygen showed oxide crystals of about 1 micron in size and well oriented to the metal grain. The oxide crystals formed in rows across the metal grain. The spacings between the rows of oxide crystals were between 0.5 and 1.0 microns. At higher oxygen pressures and for higher oxygen additions the individual oxide crystals grew to a larger size, filling in the voids between the rows of oxide crystallites. The density of oxide crystals was of the order of  $10^8 \text{ cm}^{-2}$ .

Circular oxide growth patterns occurred on some of the grains. We related these growth patterns to the presence of inclusions in the metal grain. The line growth pattern of oxide nucleation caused us much concern. It was concluded that further studies should be made using high-vacuum annealing of the iron instead of pure hydrogen annealing. Gulbransen and Andrew,<sup>10</sup> using high-vacuum-annealed pure iron, showed that the oxide crystallites occurred in a nearly random distribution. However, each crystal was oriented to the metal grain. The pattern of oxide nucleation could be changed by variations in the annealing processes.

### 3.3 ORIENTATION OF OXIDE FILMS ON IRON

The orientation of FeO on  $\alpha$ -Fe was studied by Mehl and McCandless<sup>11</sup> and by Bardolle and Bénard<sup>1</sup> using X-ray diffraction. Gulbransen and Ruka<sup>12</sup> studied the same problem using reflection electron diffraction and, in addition, studied the orientation of  $\text{Fe}_3\text{O}_4$  on  $\alpha$ -Fe. All of the results suggest that the cube plane of FeO and  $\text{Fe}_3\text{O}_4$  grows on the cube plane of  $\alpha$ -Fe, while the [100] direction of the oxide lies parallel to the [110] direction in the metal.

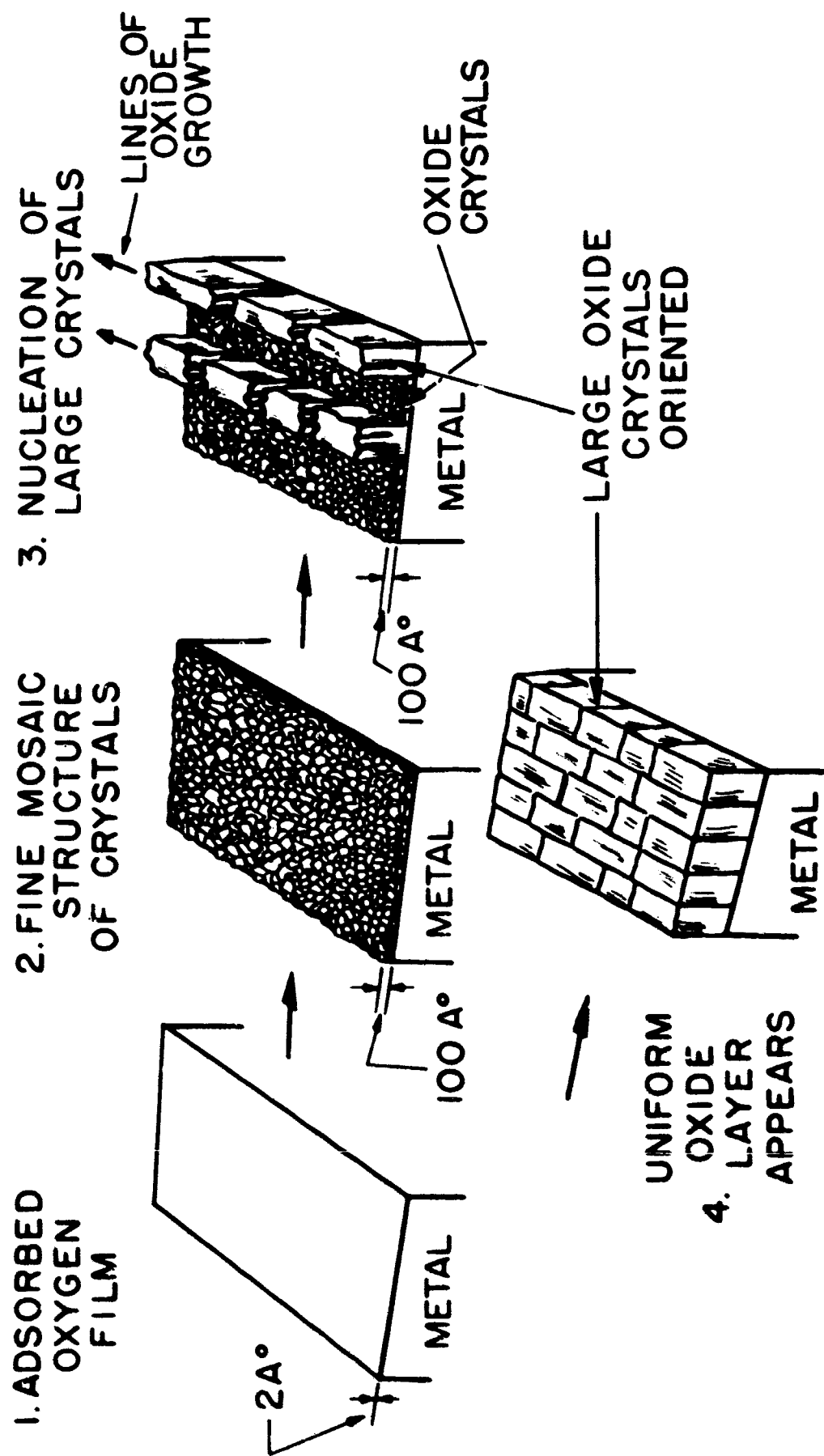
### 3.4 PICTURE OF INITIAL OXIDE FORMATION

Our concept<sup>2,10</sup> of the initial stages of the oxygen reaction is shown in Figure 1. It may be postulated that the first step involves a chemisorbed layer of oxygen atoms. This would be a very transitory stage at 850°C with the quantity of oxygen available. The formation of a film consisting of small oxide crystallites of the order of the thickness of the oxide film is postulated to occur as the reaction continues to a thickness of 100 Å. The next stage of oxidation appears to be nucleation and growth of larger crystals along certain rows of the metal grain. Along these growth sites a lower free-energy barrier appears to exist for the formation and growth of new oxide crystals.

The properties of these linear growth sites suggest that they represent a substructure in the metal which is influenced by the annealing environment. Hydrogen and impurities in the hydrogen gas appear to order the sites for oxide nucleation on pure iron. The mechanism of this process is not clear.

These larger oxide crystals are well oriented to the structure of the metal grain. As oxidation continues, these crystals grow and new ones are formed completing the mosaic structure. This is shown in step d of Figure 1. Finally, a granular oriented oxide film is formed. Although the oxide crystals are oriented, there are many oxide crystals on each metal grain.

Fig. 1 OXIDATION MECHANISM



#### 4. PHENOMENOLOGICAL STUDIES ON OXIDE WHISKERS AND PLATELETS

##### 4.1 INTRODUCTION

The formation of long filaments or whiskers of oxide during the oxidation of metals was first observed by Pfefferkorn<sup>3</sup> in Germany and by Takagi<sup>4</sup> in Japan in the early 1950's. Both workers studied the edges of wires and of fine holes in metal sheets after oxidation using transmission electron microscopy. At this early date the metals used and the reaction conditions were poorly defined. The oxide whiskers were formed after considerable oxidation of the metal had occurred.

On first consideration, one might suggest that oxide nuclei and oxide whiskers could grow from the same nucleating sites on the metal as the initial oxide nuclei in low-pressure oxidation. It is impossible to judge from the shapes and growth characteristics whether the same sites are involved since the conditions of growth of nuclei on a nearly bare surface are very different from the conditions of growth found in thick oxide films. There is no experimental information available relating oxide nucleation and oxide whisker formation.

We began the study of oxide whiskers in 1957 for the purpose of understanding localized corrosion and oxidation on iron and stainless steel. It was hoped to relate localized corrosion processes to the phenomena of stress corrosion.

In the early work, five factors were considered important in planning the experiments and in discussing the growth of oxide whiskers and platelets. These are: (a) the crystal structure, (b) the crystal morphology and size, (c) the orientation of the oxide crystal with respect to the underlying interface, (4) the nature of the reaction site in the metal or on the oxide, and (5) the mechanism of growth.

A vacuum microbalance reaction system<sup>13</sup> was used in many of the early experiments involving the reaction with dry oxygen at 0.1 atm pressure. A liquid nitrogen cooled trap was used to lower the water vapor concentration to a dew point of  $-196^{\circ}\text{C}$ . The furnace system was controlled to  $\pm 1^{\circ}\text{C}$ . This reaction system was used to react iron specimens where minimum water vapor concentrations were required. A second reaction system<sup>14</sup> was used for reaction of wire or tensile test specimens under stress in steam, in mixtures of steam and oxygen, or in mixtures of steam, oxygen, and HCl vapor. Figure 2 shows the apparatus. Oxygen is bubbled through a heated flask of water or dilute HCl solutions. The gas atmosphere is passed over the specimens mounted in the furnace as shown in Figure 2.

Disc, wire, and tensile test specimens shown in Figure 3 were used. The edge of the hole in the disc or tensile specimen and the edge of the wire specimen were studied in the electron microscope. The wire and tensile test specimens could be pre-stressed or reacted under stress. The stress level at the small hole in the tensile specimen is approximately three times that of the stress in the adjacent metal.

An EMU-3D RCA electron microscope was used. This instrument was used at 100 kV and had facilities for both direct transmission electron diffraction and selected-area electron diffraction. The relative rotations of the selected-area electron diffraction patterns were determined by the use of selected-area images and the selected-area diffraction patterns of asbestos fibers.

#### 4.2 OXIDE WHISKERS

In addition to the normal oxide film, fine oxide whiskers form on annealed iron in dry oxygen atmospheres at temperatures of  $400^{\circ}$  to  $500^{\circ}\text{C}$ . A few small fan-shaped oxide platelets form in the early stages of oxidation before oxide whiskers.

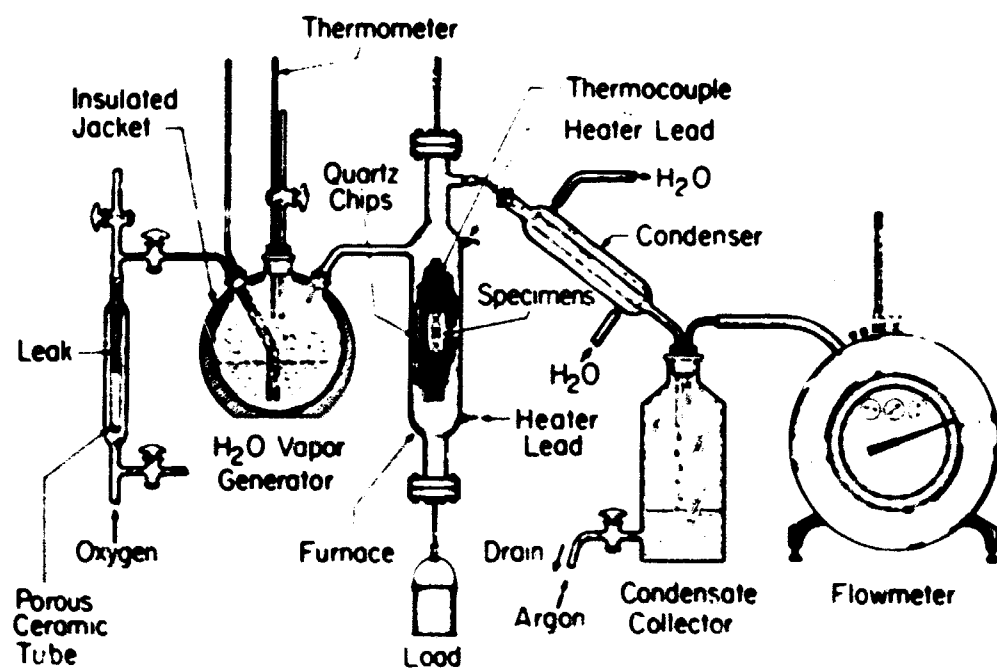


FIG. 2 Stress corrosion reactor system

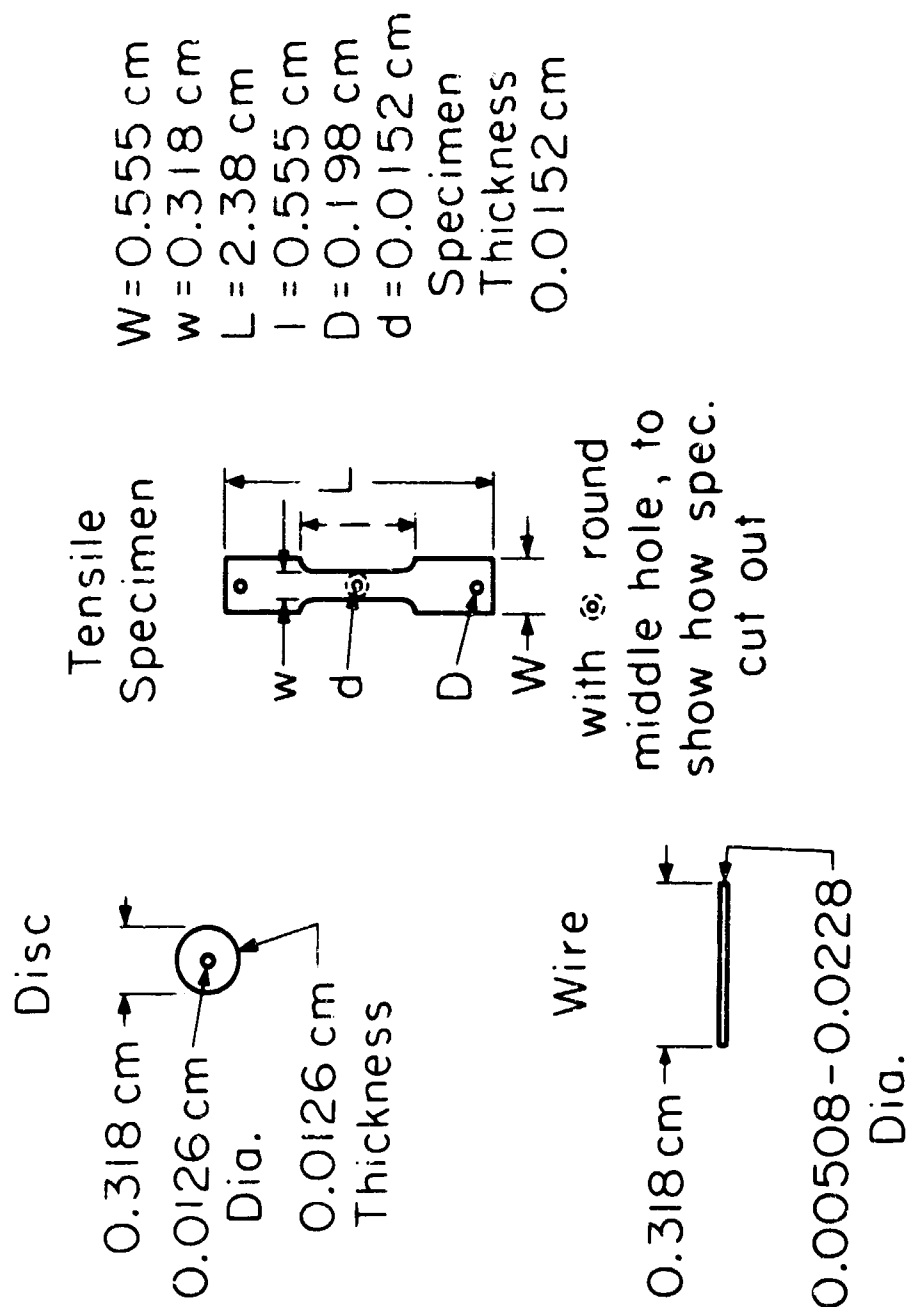


Fig. 3 Specimen types

Figure 4 shows an electron micrograph of an oxidized disc of "Puron" grade of iron. The iron was reacted for 48 hours in an atmosphere of dry oxygen at 76 torr. The oxide whiskers were 150 Å or more in diameter, excluding contamination, and 15,000 Å in average length. Some grew to 75,000 Å in length. A surface density of about  $10^8 \text{ cm}^{-2}$  was estimated. The geometry of whiskers growing on a wire is discussed in Appendix I.

To show that oxide whiskers are not due to impurities in the reacting gas phase a special static reaction system was built in which the reacting gases and the product gases were monitored by sensitive mass spectrometer methods.

The reaction chamber consisted of a zirconia tube and a quartz frame for supporting the annealed iron wires. The high vacuum valve and high vacuum gasket were attached to the zirconia tube but removed from the high temperature zone. The tube could be outgassed at 650°C and pumped to  $10^{-6}$  torr prior to moving the mounted iron wires into the reaction zone and to the addition of specified quantities of mass spectrometrically analyzed gases. Changes in both composition and quantity of gas resulting from the reaction could be established.

Vacuum-annealed and etched pure iron wires were reacted at 400°C with pure  $\text{O}_2$  at 620 torr for 48 hours. Electron micrographs showed the formation of oxide whiskers 150 Å in diameter and having an average length of 8000 Å. Electron diffraction patterns taken by the transmission method of the oxidized wire gave a pattern of  $\alpha\text{-Fe}_2\text{O}_3$ . The interplanar spacings are shown in Table 3. A discussion of the  $\alpha\text{-Fe}_2\text{O}_3$  structure and further details of the intensities and lattice spacings are given in Appendices II through VIII.

Mass spectrographic analysis of the reaction gases showed the formation of  $3.0 \times 10^{19} \text{ H}_2$  molecules during reaction. Originally  $4.4 \times 10^{21} \text{ O}_2$  molecules were present in the reaction system. The  $\text{H}_2$  gas could arise from the etching treatment and could be released during oxidation. The experiment shows that a trace of water vapor is not





Fig. 1 Fine oxide whiskers formed on "Puron"  
at 500°C in dry oxygen for 48 hours.  
No applied stress. Micron length  
shown.

RM 15321

TABLE 3

Interplanar Spacings, Whisker Growths on Iron Reacted with Dry O<sub>2</sub>  
400°C, 48 hrs.

Visual Intensity I/I <sub>0</sub>	d (experimental)	d (calculated)
50	3.674 Å	3.6795 Å
100	2.699	2.6973
70	2.511	2.5158
50	2.208	2.2050
30 broad	1.933	1.8398
50	1.695	1.6933
40	1.487	1.4851
40	1.456	1.4525
20	1.310	1.3101

important in the growth of oxide whiskers on iron. The role of small quantities of hydrogen in the metal on the growth process of oxide whiskers has to be studied

A summary of the properties and conditions of formation of oxide whiskers is given in Table 4.

#### 4.3 POINTED BLADE-SHAPED OXIDE PLATELETS

When annealed or cold-worked iron was reacted with water vapor atmospheres containing oxygen, pointed blade-shaped oxide platelets form. Figure 5 shows the genesis of blade-shaped oxide platelets when iron was reacted with 10% water vapor and 90% argon mixture. Traces of oxygen were present in the argon gas. Figure 5a shows that both oxide whiskers and blade-shaped platelets were formed after 2 hours of reaction. The whiskers were about 150 Å in diameter and averaged 10,000 Å in length. The oxide platelets were about 150 Å thick, 1000 to 1500 Å wide and grew

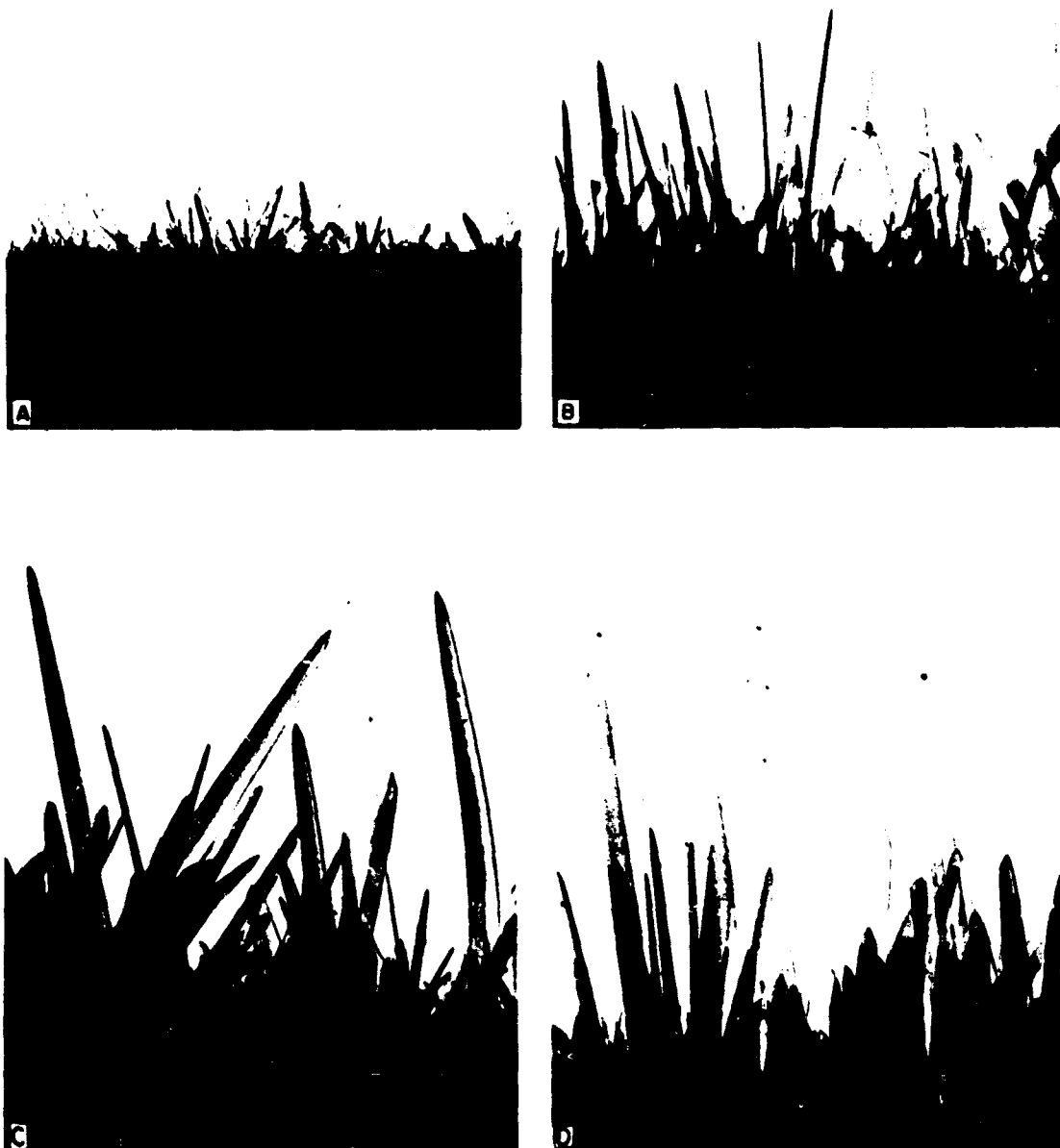


Fig. 5 - Blade-shaped oxide platelets formed on annealed pure iron in 10%  $H_2O$  and 90% argon at  $400^\circ C$ . Micron length shown.

(A) 2 hours

(B) 6 hours

(C) 12 hours

(D) 23 hours

TABLE 4

Summary of Data on Oxide Whiskers

1. Diameter  $\sim 150 \text{ \AA}$ ;
  2. Lengths up to  $4 \times 10^5 \text{ \AA}$ ;
  3. Density up to  $10^8 \text{ cm}^{-2}$ ;
  4. Weight of  $10^5 \text{ \AA}$  whisker =  $9.25 \times 10^{-15} \text{ g}$ ;
  5. Crystal structure -  $\alpha\text{-Fe}_2\text{O}_3$  - single crystal;
  6. Site area -  $1.77 \times 10^{-12} \text{ cm}^2$  (cross section);
  7. Percent surface covered for density  $10^8 \text{ cm}^{-2} = 0.0177$ ;
  8. Conditions - dry oxygen, no stress, pure metal, random sites on oxides or metal;
  9. Stress at root = 3.1 psi for  $4 \times 10^5 \text{ \AA}$  whisker 150  $\text{\AA}$  diameter;
  10. Thickness - nearly independent of time;
  11. Melting of tip - prevents further growth;
  12. Effect of  $\text{H}_2$  - reduced to metal lump.
- 

to lengths up to 10,000  $\text{\AA}$ . Figure 5b shows that most of the whiskers were absent after 6 hours and only oxide platelets were formed. Figures 5c and 5d show that the size of the oxide platelets increases with time. After 23 hours of reaction the platelets were 2500 to 6000  $\text{\AA}$  wide and up to 70,000  $\text{\AA}$  long with a surface density of  $10^8 \text{ cm}^{-2}$ .

Table 5 shows a summary of the properties and conditions of formation of the blade-shaped oxide platelets on iron specimen reacted with steam and argon at 400°C for 7 hours. The interplanar spacings could be correlated exactly with the calculated values for  $\alpha\text{-Fe}_2\text{O}_3$ .

#### 4.4 REACTION WITH PURE $\text{H}_2\text{O}$ VAPOR

Thermodynamic calculations from Tables 1 and 2 show that water vapor in the absence of oxygen does not react with  $\text{Fe}_3\text{O}_4$  to form  $\alpha\text{-Fe}_2\text{O}_3$  unless hydrogen is removed. Earlier experiments had shown that blade-shaped oxide platelets were formed in water vapor plus argon. To test the effect of traces of oxygen in the argon gas, experiments were

TABLE 5

Summary of Data,  
Pointed Blade-Shaped Oxide Platelets

1. Thickness  $\sim 150 \text{ \AA}$ ;
2. Widths up to  $1.5 \times 10^4 \text{ \AA}$ ;
3. Lengths up to  $9 \times 10^4 \text{ \AA}$ ;
4. Density up to  $10^8 \text{ cm}^{-2}$ ;
5. Weight =  $5.3 \times 10^{-13} \text{ g}$  for platelet  $9 \times 10^4 \text{ \AA}$  long and  $1.5 \times 10^4 \text{ \AA}$  wide;
6. Crystal structure  $\alpha\text{-Fe}_2\text{O}_3$  ( $400^\circ\text{C}$  temperature of formation);
7. Site area -  $2.3 \times 10^{-10} \text{ cm}^2$  for platelet  $9 \times 10^4 \text{ \AA}$  long,  $1.5 \times 10^4 \text{ \AA}$  wide and  $150 \text{ \AA}$  thick;
8. Percent of surface covered for  $10^8 \text{ cm}^{-2} = 2.25$ ;
9. Conditions -  $\text{H}_2\text{O} + \text{O}_2$ , stress or unstressed metal, probably oriented sites, pure metal;
10. Thickness - nearly independent of time.

made with pure  $\text{H}_2\text{O}$  vapor. Distilled  $\text{H}_2\text{O}$  was injected into the high vacuum system and further purified of oxygen and other gases by repeated freezing and pumping prior to introduction into the reaction chamber. The specimens were heated at  $425^\circ\text{C}$  for 45 hours at a pressure of 6 torr. Electron microscope studies showed no evidence of oxide whiskers or platelet growths although the wires were covered with a black oxide. The absence of oxide platelet growth may be attributed to the lower total oxygen content obtainable in a static reaction system, thus preventing the formation of  $\alpha\text{-Fe}_2\text{O}_3$ .

Mass spectrometric analysis of the gases after reaction showed  $4.4 \times 10^{19}$  molecules of  $\text{H}_2\text{O}$ ,  $1.26 \times 10^{18}$  molecules of  $\text{H}_2$ ,  $5 \times 10^{17}$  molecules of  $\text{CO}$ , and  $1.2 \times 10^{18}$  molecules of  $\text{CO}_2$ . The oxygen level was less than  $4 \times 10^{15}$  molecules, which was the sensitivity of the instrument.

The oxygen associated with the observed  $H_2$  would form an oxide film of about 6000 Å on the  $1 \text{ cm}^2$  surface of iron.

We conclude that small quantities of oxygen are required to form blade-like  $\alpha\text{-Fe}_2\text{O}_3$  platelets on iron.

#### 4.5 MECHANISM OF BLADE-LIKE OXIDE PLATELET FORMATION

Figure 5 suggests that iron exposed to water vapor and traces of oxygen forms oxide whiskers in the first stage of reaction and blade-like oxide platelets at later stages of oxidation.

The fact that whisker growth is replaced by platelet growth suggests that the whisker growth point sites have been replaced by line sites producing platelets. Either the line sites are new or they result from growth of the point sites. The hydrogen atoms act to cause this effect either (1) at or about the sites, or (2) in or on the platelets. The hydrogen atoms could be involved in the platelet twin interface structure, for example, allowing platelets to grow where only whiskers could grow in the absence of water vapor. The most simple hypothesis is that the point sites are transformed into line sites by the direct action of the hydrogen.

The thickness of the oxide platelets remains nearly constant with time and is nearly the same as that of the whiskers formed in dry oxygen atmospheres. The shape of the blade-like oxide platelets indicate the width of the platelets is a function of time or extent of reaction.

#### 4.6 STUDY OF THE $O_2/H_2O$ RATIO

Experiments were made to study the effect of  $O_2$  to  $H_2O$  ratio on the formation of localized oxide crystals on iron. Blade-like platelets were the predominant crystal habit formed after reaction at  $450^\circ\text{C}$  for 48 hours in  $O_2/H_2O$  ratios of 9/1 and 30/1 in a dynamic reaction system. To prevent the growth of oxide platelets the  $O_2/H_2O$  ratio must be increased to large values. On the other hand blade-like platelets can form for very small  $O_2/H_2O$  ratios but not in pure water.

These studies showed that the total amount of oxide in the oxide platelets was over 250 times the amount of oxide in the oxide whiskers when the iron was reacted with dry oxygen for the same temperature and reaction conditions.

#### 4.7 ROUNDED OXIDE PLATELETS

Thin, rounded oxide platelets were formed when cold-worked iron was reacted with dry oxygen. Figure 6 shows an electron micrograph of the localized oxide growths formed after oxidation of cold-drawn iron wire at 400°C for 48 hours in 760 torr of dry oxygen.

Thin, rounded oxide platelets grew with faces approximately parallel to the axis of the wire to a height of 40,000 Å and to lengths up to 70,000 Å. The thickness of the platelets was estimated to be of the order of 150 Å, about the same as that found for the blade-shaped oxide platelets and oxide whiskers. The thickness appears uniform over the platelet and the same for a large number of platelets examined. These platelets are characterized by bend contours.

Table 6 shows a summary of the properties and conditions of formation of rounded oxide platelets.

TABLE 6

Summary of Data, Rounded Oxide Platelets

1. Thickness  $\sim 150$  Å;
2. Widths up to  $2 \times 10^5$  Å;
3. Lengths up to  $1.5 \times 10^5$  Å;
4. Density  $\sim 10^6$  cm<sup>-2</sup>;
5. Weight =  $3.1 \times 10^{12}$  g for  $2 \times 10^5$  Å long and  $1.5 \times 10^5$  Å wide platelet;
6. Crystal structure -  $\alpha$ -Fe<sub>2</sub>O<sub>3</sub>;
7. Site area -  $3 \times 10^{-9}$  cm<sup>2</sup> for platelet  $2 \times 10^5$  Å wide and  $1.5 \times 10^5$  Å long;
8. Percent of surface covered for  $10^6$  cm<sup>-2</sup> = 0.3%;
9. Conditions - O<sub>2</sub>, metal in stressed conditions, impurities in metal;
10. Thickness - nearly independent of time.



Fig. 6 - Rounded oxide platelets formed on cold-worked pure iron in 1 atm of dry oxygen at 400°C for 48 hours. Micron length shown.



#### 4.8 BLUNTED BLADE-SHAPED OXIDE PLATELETS

Reaction of high purity annealed and etched iron wires in an atmosphere of 10%  $H_2O$  + 90% (He + 1000 ppm  $O_2$ ) at 400°C for 4 hours has shown a new crystal habit. Instead of pointed blade-shaped oxide platelets, as in the case of 4.3, blunted blade-shaped platelets are formed. The blunted end is characteristic of these platelets even from the early stages of reaction. Figure 7 shows a typical electron micrograph. The blunted end has a chisel-shaped appearance. However, the thickness of the material as revealed by the contrast in electron micrographs is nearly constant.

The possibility that these platelets are not solid and uniform in cross section is shown in Figure 8. Here the blunted blade-shaped platelets were heated in the electron beam. The helium gas trapped in the blade-shaped crystal expanded and formed gas bubbles in or ruptured the platelets leaving the platelet wall exposed. Many smaller bubbles were formed on the flat faces of other oxide platelets. The shape of these bubbles and ruptured platelets indicates that the platelets have an internal surface where helium was collected between the crystal faces and that the oxide was ductile.

The experiments using helium as a carrier gas suggest that oxide platelets and whiskers have internal boundaries or axial screw dislocations. The essential feature of the suggested growth mechanism is that the internal defects provide paths for rapid diffusion of iron at rates large compared to normal lattice diffusion. The true nature of the internal defects can be further revealed by selected-area electron diffraction.



Fig. 7 - Blunted blade-shaped oxide platelets formed on annealed pure iron in 10%  $H_2O$  + (He + 1000 ppm  $O_2$ ) at 400°C and 5 hours.

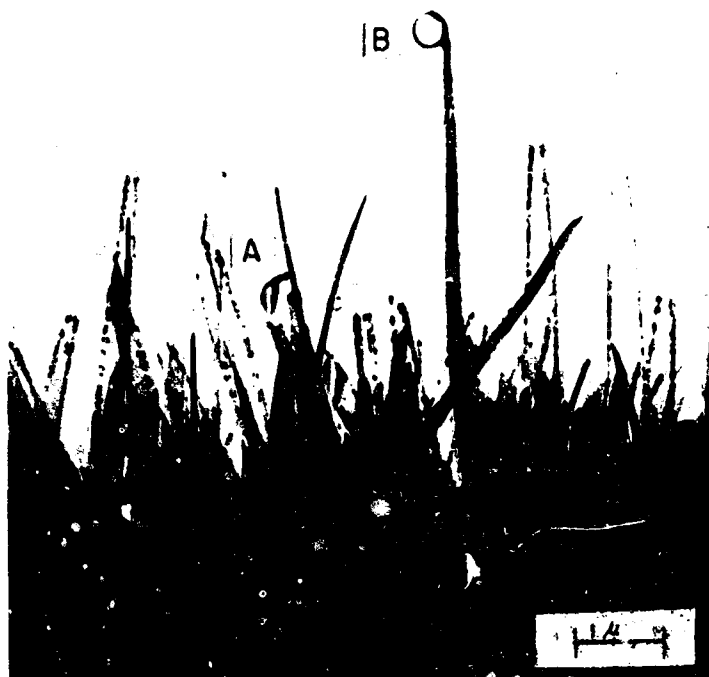


Fig. 8 - Effect of electron beam heating on blunted blade-shaped oxide platelets, A. ruptured platelet, B. hollow bubble.

## 5. STUDIES USING SELECTED-AREA ELECTRON DIFFRACTION

### 5.1 INTRODUCTION

The phenomenological aspects of the growth of oxide whiskers and platelets has been discussed in some detail in section IV. The development of the selected-area electron diffraction method made possible crystallographic studies on single oxide whiskers and platelets. To correctly evaluate the selected-area electron diffraction patterns it was essential to bring together the structural information on the iron oxides. This was done in Appendices:

- II  $\alpha\text{-Fe}_2\text{O}_3$  Crystal Structure,
- III  $\alpha\text{-Fe}_2\text{O}_3$  Unit Cells,
- IV Transformation of Indices
- V Interfacial and Other Angles in  $\alpha\text{-Fe}_2\text{O}_3$ ,
- VI Systematic Absences in the Diffraction from  $\alpha\text{-Fe}_2\text{O}_3$ ,
- VII List of Interplanar Spacings,
- VIII Intensities and d-Spacings for Selected Iron Oxides.

In order to make possible a more ready recognition of the geometrical relations indicated by the indices shown on our selected-area electron diffraction patterns and elsewhere, we have chosen the face-centered rhombohedral F unit cell shown in Figure 21 of Appendix III.

Figure 21 shows top and front views and dimensions for the unit cells of  $\alpha\text{-Fe}_2\text{O}_3$  and its isomorphs. The four conventional unit cells in common use are shown at the right and left in Figure 21. The conventional structural hexagonal and rhombohedral unit cells are shown at the left in the figure. Four indices are used to describe a set of lattice planes in terms of the hexagonal unit cell. The conventional morphological unit cells are shown at the right, together with the morphological rhombohedral parameters.

The  $a$  parameter is twice that for the conventional morphological rhombohedral unit cell. The rhombohedral F cell angle  $\alpha$  is nearly  $90^\circ$ . It is this approximation to a face-centered cube which makes the rhombohedral F cell convenient. This cell is used in all indexing of our selected area diffraction patterns and is referred to whenever the unit cell system is not identified. Conventional structural hexagonal and rhombohedral indices will also be given.

## 5.2 OXIDE WHISKERS

### 5.2.1 Analyses of Single Oxide Whisker Patterns

Figure 9 shows a selected-area electron diffraction pattern from an iron oxide whisker measuring 1.5 microns in the selected area image. The pattern is indexed with the rhombohedral F unit cell. The orientation of the projection of the axis of the whisker lies normal to the layer lines of the pattern shown in Figure 10, i.e. in the  $[\bar{2}20]$  direction. This whisker axis is  $[\bar{1}\bar{1}20]$  and  $[\bar{1}01]$  in the conventional structural hexagonal and structural rhombohedral indices, respectively. In each system, this direction is normal to lattice planes of the same indices.

An analysis of the diffraction spots in Figure 9 shows two nets, a net normal to the  $[111]$  direction and a net normal to the  $[110]$  direction. (By "net" we mean two-dimensional lattice.) The angles between rows of spots are within  $1^\circ$  of the angles between rows of index points in the reciprocal lattice of  $\alpha\text{-Fe}_2\text{O}_3$ . The sections of whisker giving the two reciprocal lattice nets lie at  $32.4^\circ$  to one another.

Both nets of Figure 9 include the origin,  $\bar{2}20$ , and  $2\bar{2}0$ . We conclude, therefore, that the rotation axis of the pattern is  $[\bar{2}20]$ . The same conclusion results from the fact that the spots of each layer line are indexed by points in a corresponding reciprocal lattice net normal to  $[\bar{2}20]$ .

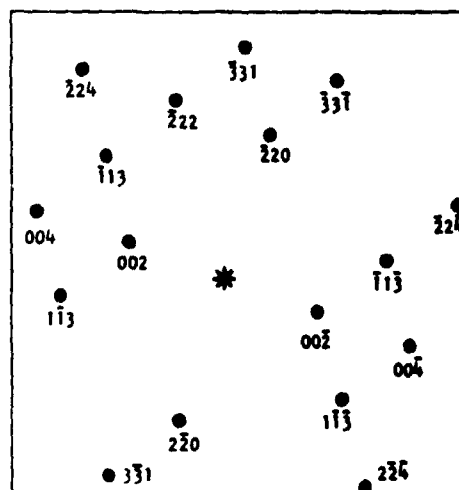
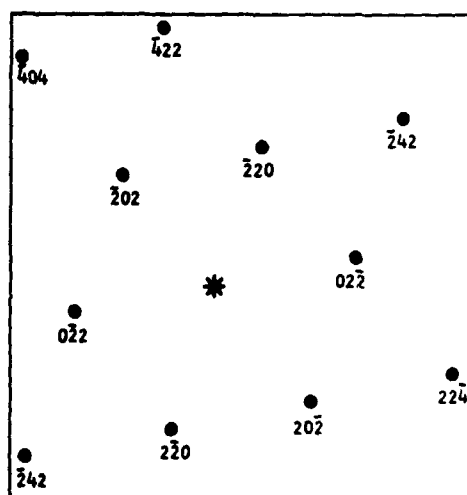
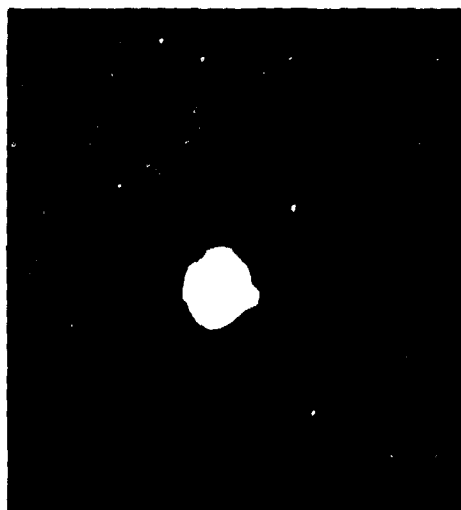


Fig. 9 - Selected-area electron diffraction,  $\alpha$ -Fe<sub>2</sub>O<sub>3</sub> whisker, 1.5  $\mu$  long,  $10^{-15}$  g. Indexed with a face-centered rhombohedron,  $\alpha = 85.7^\circ$ . Nets normal to [111] and [110] included.

Two additional oxide whiskers which have been studied satisfactorily by selected-area electron diffraction are of interest. In one, two new nets of spots, normal to the  $[001]$  and  $[\bar{1}\bar{1}2]$  directions, respectively, were found. The rotation axis of the oxide whisker was  $[\bar{2}20]$ . The whisker axis was proved to be the rotation axis as follows: The whisker axis lies in a plane perpendicular to the pattern of the second oxide whisker different from the plane of the whisker axis for the whisker giving the pattern shown in Figure 9. These two planes intersect in the  $[\bar{2}20]$  rotation axis. If the whisker axis is the same in the two cases, it is  $[\bar{2}20]$ .

The same rotation axis,  $[\bar{2}20]$ , was found for the third indexed pattern. The axis was far from perpendicular to the beam direction, however. Again the projections of the whisker and rotation axes coincide in the pattern. This is a more common type of diffraction pattern than that shown in Figure 9. Bent, kinked, and apparently multiple whiskers introduce further complications.

The three different selected area patterns which were indexed include very weak extra diffraction spots on the layer lines. Some of the spots correspond in position in the pattern to the systematically absent diffraction from planes of the form  $\{11\bar{1}\}$ , but most of the spots could not be indexed. The anomalous spots were also found by Takagi.<sup>4</sup>

Since the whisker axis and the rotation axis coincide we are led to hypothesize that the whisker is twisted. This is consistent with the diffraction patterns of individual whiskers, in that they show a limited rotation by including diffraction represented by appropriately limited sectors of the reciprocal lattice. Since no grain boundaries are commonly revealed by diffraction contrast in the micrographs, any grain boundaries which may exist must be such that the contrast is difficult to observe. The probability that a small number of untwisted crystals might lie in the special orientations in the beam indicated by the diffraction patterns of individual whiskers is negligible. Thus, the most simple whiskers do not contain grain boundaries.

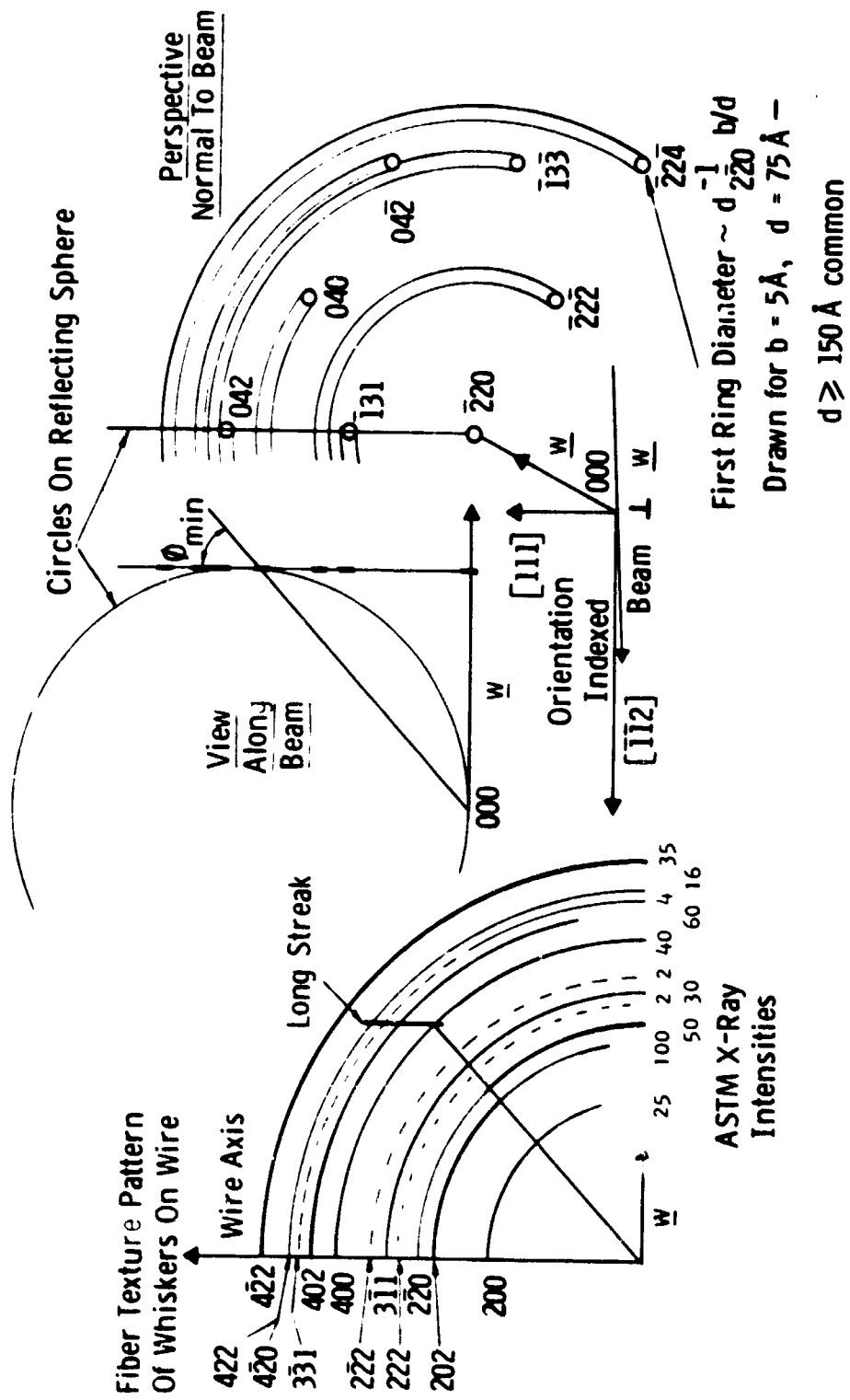
### 5.2.2 Analyses of Streaked Reflections

The electron diffraction patterns for whiskers on a wire as recorded from the whole beam without lenses between the specimen and the plate, as opposed to selected area diffraction patterns, show less distorted diffraction from more whiskers. The distribution of whiskers with respect to angles in the beam is maximal for whiskers nearly normal to the wire axis and to the beam. This is true because such whiskers extend more into the beam and, furthermore, because of the distribution of whisker angles to the surface. Since the electron micrographs show the character of whisker orientation distribution, the texture pattern has not been analyzed completely for such information in this work. However, some less striking details resulting from the axial twist of the whiskers have proved to be of interest. One would not expect the axial twist to affect the intensity distributions about the diffraction rings for large numbers of whiskers, because such a specimen, assuming no epitaxial effects and no twist, would show random orientation about the fiber axis (i.e., about the normal to the wire or other surface shadow). The number of whiskers in the beam may be far from statistical in this sense, and the high density of spots on the rings may result from the twist. The possibility of quantitatively determining that this is so has not been explored. Some of the intensity variation on the arcs is shown roughly in Figure 10.

Figure 10 shows how the axial twist results in the streaking of reflections found between the 400 and 402 ( $02\bar{2}4$  and  $11\bar{2}6$ ) rings in the regions of the pattern equivalent to that about the one long streak indicated. At the right of Figure 10 the reciprocal lattice net second from the origin along the whisker axis is shown for an orientation to be found in a short section of a whisker of axis W. The beam and whisker orientations are indicated. The first ring in the disk-like intensity region which exists about each spot according to Wilson's<sup>15,16,17</sup> theory has been drawn large, as for a small whisker. The rotation of the net by the twist (without bending) passes the intensity regions through a line on the reflecting sphere in the Ewald construction. This line is



Fig. 10—Twist of unbent  $\alpha$ -Fe<sub>2</sub>O<sub>3</sub> whisker  
results in streaked 2nd layer line  
(Indexing for rhombohedral F,  
 $a = 7.3976 \text{ \AA}$ ,  $\alpha = 85.715^\circ$ )



shown in the view along the beam at the center of Figure 10, where the view is like a view from the right of the right-hand section. The rotation thus results in an integration by the beam giving a radial distribution about  $\bar{2}20$  of the absolute square of the electron wave function in a sector of the reciprocal lattice net. Under favorable conditions this diffraction can be observed as a streak extending, as illustrated, across the 400 and  $4\bar{2}0$  rings. Streaks between the 400 and 402 rings are more common, and spots in these rings are streaked along the same directions in these regions. If the whiskers were all parallel, these streaks would be in the second layer line of the fiber pattern.

The angle  $\phi$  made by these streaks with the radius to the 040 spots indexed for the arbitrary axis and reciprocal lattice section illustrated is given by

$$\tan \phi = [1 - \sin^2 \gamma (1 + \tan^2 \phi_{\min})]^{-1/2} \tan \phi_{\min},$$

where  $\gamma = (90^\circ - \omega)$  and  $\omega$  is the angle of the whisker to the beam. Thus  $\phi = \phi_{\min}$  for  $\omega = 90^\circ$ ,  $\gamma = 0^\circ$ .  $\phi$  increases somewhat parabolically with  $\gamma$ , as follows:

$\gamma$ :	$0^\circ$	$10^\circ$	$20^\circ$	$30^\circ$
$\phi$ :	$46.99^\circ$	$47.95^\circ$	$51.1^\circ$	$57.6^\circ$

Since  $\gamma > 30^\circ$  is uncommon,  $47^\circ < \phi < 58^\circ$  is to be expected. Long streaks were measured most accurately at  $51^\circ 12'$ ,  $50^\circ 26'$ , and  $51^\circ 54'$ .

The effect of bending of the whole length about the  $[111]$  axis for the section giving the 042 reflection would increase  $\phi$ . Bending about a direction parallel to the  $\bar{2}20$ , 040 line of the section of whisker giving the 040 reflection would decrease  $\phi$ . Such bending is equivalent to a rotation. It can be seen that the positions of the streaks and their angles correspond to rotation primarily about  $[\bar{2}20]$ . This serves to confirm the selected area diffraction results.

### 5.2.3 Axial Twist Calculation

A detailed discussion of the geometry of a screw dislocation in a rod is given in Appendix IX. A summary of this discussion is given here.

The axial twist  $\alpha$  can be calculated from an equation given by Eshelby,<sup>18</sup>

$$\alpha = K b/A$$

Here  $b$  is the length of the Burgers vector,  $A$  is the cross section area, and  $K$  is a constant which depends on the shape of the cross section.  $K = 1$  for an elliptical cross section with central dislocation.

If we approximate the cross sectional area  $A$  with the area of a circle of the whisker image diameter, we can calculate the axial twist and compare this with the observed twist. The full length of whisker in the selected area image for the pattern of Figure 9 was  $1.5 \mu$ . The diameter, including the contamination layer, was about  $300 \text{ \AA}$ . Assuming the smallest Burgers vector, with length given by the minimum repeat distance along the whisker axis,  $5.03 \text{ \AA}$ , the axial twist is calculated to be  $41^\circ$  per micron. The sections of whisker for which the two reciprocal lattice nets of Figure 9 are normal to the beam are at  $32.4^\circ$  to one another by rotation about the whisker axis. If at most these two sections lie at the ends of the  $1.5 \mu$  whisker section, the axial twist is not less than  $22^\circ$  per micron; thus the  $5.03 \text{ \AA}$  Burgers vector is likely.

There are many reasons for a discrepancy between the calculated and observed axial twist: (1) both the cross section and the axial twist were not accurately determined, (2) the elastic anisotropy of  $\alpha\text{-Fe}_2\text{O}_3$  may be important and should be included in the theory, (3) the dislocation strain may have a planar character which would alter the strain distribution near the core, (4) the discrete atomic structure and the decreased stress at high strain near the dislocation should result in a slightly smaller twist than that calculated by the simple formula of Eshelby, and (5) surface stresses may decrease the axial twist.

#### 5.2.4 Strain Energy of a Whisker

A detailed discussion is given in Appendix X. The expression for the strain energy of a screw dislocation in a twisted rod is given by Friedel.<sup>19</sup> Cottrell<sup>20</sup> and Weertman and Weertman<sup>21</sup> provide estimations of the entropy contribution for the formation of a screw dislocation. They conclude that dislocations are unstable. The strain energy, even near the melting point, outweighs the entropy contribution to the free energy.

For a whisker of 100 Å radius with a hole radius of 5 Å and a shear modulus of  $10^{12}$  dynes cm<sup>-2</sup>, the strain energy is 0.09 kcal/mole. For a rod of these dimensions about 95% of the strain energy is contained in a half of the volume of the crystal within the radius  $R/\sqrt{2}$ .

#### 5.2.5 Diffraction from a Rod with an Axial Screw Dislocation

Wilson<sup>15</sup> has given a theoretical treatment of the diffraction from a cylindrical crystal with an axial screw dislocation. Wilson's mathematical description of the crystal fails to take into account the axial twist, probably because it was not generally recognized at that time. For the real case of a cylindrical crystal with an axial screw dislocation, such as a whisker, the axial twist may be as important as the screw dislocation. Appendix XI presents a more detailed discussion of the special diffraction effects.

#### 5.2.6 Comparison with Earlier Work

Miyake<sup>22</sup> reported in 1937 a preferred orientation in the electron diffraction pattern of  $\alpha$ -Fe<sub>2</sub>O<sub>3</sub> formed on an oxidized iron specimen. He stated that the (10 $\bar{1}$ ) structural rhombohedral plane was parallel to the surface. Apparently lack of knowledge of the existence of oxide whiskers precluded a complete interpretation. The (10 $\bar{1}$ ) structural rhombohedral plane given by Miyake is normal to the whisker axis we have determined.

Takagi<sup>4</sup> determined the growth axis of localized  $\alpha$ -Fe<sub>2</sub>O<sub>3</sub> growths using diffraction patterns of individual growths. That Takagi's work preceded the general recognition of axial twist apparently explains his failure to recognize the rotation pattern. Takagi oxidized pure iron in flowing dry oxygen, but not so dry as to prevent the formation of oxide platelets. He observed that whiskers and sometimes smaller blades grew from broken bases of blades. This and other observations suggested that growth is from the top. Takagi postulated a screw dislocation mechanism for the localized growths. He considered surface diffusion to provide the transfer of metal.

Bigot<sup>13</sup> and Talbot and Bigot<sup>14</sup> failed to correctly analyze their selected-area electron diffraction patterns of  $\alpha$ -Fe<sub>2</sub>O<sub>3</sub> whiskers and platelets. They gave no indexing for their whisker rotation patterns. Instead they determined the whisker axis on the basis that the most intense spots are aligned parallel to the smallest dimension of the crystal. They gave incorrectly the structural hexagonal direction  $[10\bar{1}0]$  as the whisker axis without supporting data. The most intense arc in the fiber texture pattern for whiskers on an oxidized iron surface is at 90° to the surface in the  $11\bar{2}0$  ring. This results from the preferred orientation of the  $(11\bar{2}0)$  planes, which are normal to the  $[11\bar{2}0]$  whisker axis. Thus, the most intense arc is on a normal to the  $[10\bar{1}0]$  direction, but this is not the whisker axis.

### 5.3 POINTED BLADE-SHAPED PLATELETS

#### 5.3.1 Morphological Description

Figure 11 shows an electron micrograph of an assembly of blade-like oxide platelets formed on annealed pure iron when reacted in 10% water vapor and 90% argon containing a trace of oxygen for 25 hours at 400°C. Blade-like platelets grown under other reaction conditions using water vapor and oxygen exhibit similar lengths, thicknesses, and ratios of width to length. Differences are found in the tip shapes, in the



Fig. 11 - Pointed blade-like platelets at the edge of an iron wire after 24 hours at 450°C in 10% H<sub>2</sub>O in argon with a trace of oxygen.



Fig. 12 - Selected-area mode,  $\alpha$ -Fe<sub>2</sub>O<sub>3</sub> pointed blade-like platelets at the edge of a wire.

presence of striated growth patterns on the faces, and in the presence of curvature in the plane of the oxide platelet. Electron diffraction analyses of many of these platelets suggest that all of such platelets have essentially the same structure.

Figure 12 shows a selected area diffraction pattern for a number of blade-like platelets at one edge of an oxidized wire. Such fiber texture patterns are satisfactorily indexed by the  $\alpha\text{-Fe}_2\text{O}_3$  unit cell. This confirms the results of an earlier study<sup>5</sup> in which the electron diffraction pattern for platelets was found to be the  $\alpha\text{-Fe}_2\text{O}_3$  powder diffraction pattern. Table 7 shows the  $d_{hkl}$  values, the intensities, and the three indexing systems for  $\alpha\text{-Fe}_2\text{O}_3$ . The conventional structural rhombohedral P and hexagonal indices and the face-centered rhombohedral F indices are given. The geometry of the rhombohedral F system is readily understood as a small distortion of cubic geometry. The indices used, unless otherwise indicated, refer to the rhombohedral F system.

In Figure 12 the regions of greatest intensity lie in the 202 ring. Arcs of weak  $1\bar{1}1$  reflections together with possible  $111$  spots, both forbidden, are apparent near the center.

### 5.3.2 Analyses of Selected Area Diffraction Patterns

Eight different selected area patterns have been indexed. Six of these are shown in Figures 13, 14, and 15. The axis of the blades was found to be  $[\bar{2}20]$ , i.e.  $[\bar{1}\bar{1}20]$  and  $[\bar{1}01]$  in the conventional structural hexagonal and rhombohedral systems, respectively. This axis is the fiber axis of the fiber texture patterns from surfaces with dense growths of blades.

The most striking characteristic of the blade diffraction is that resulting from the reciprocal lattice rods normal to the blade face. This face is  $(11\bar{1})$ , and the rods show a distorted hexagonal pattern corresponding to the three-fold symmetry of the  $\langle 111 \rangle$  body

TABLE 7

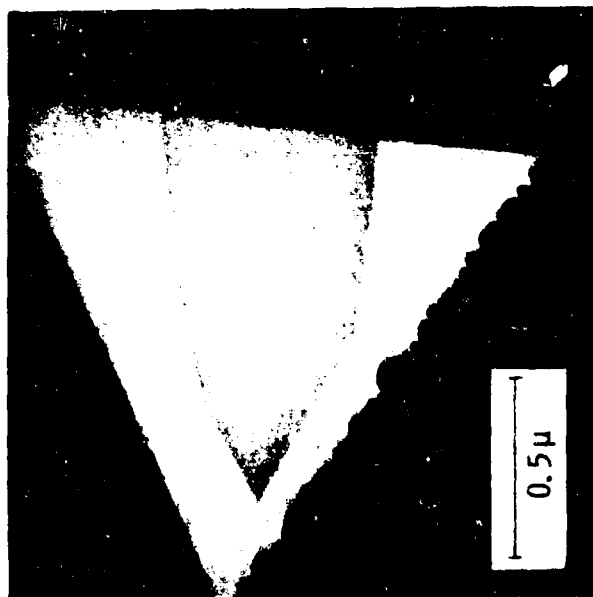
 $\alpha$ -Fe<sub>2</sub>O<sub>3</sub> d-values, Intensities,<sup>25</sup> and Indices

$I/I_0$	$d_{hk11}^b$	Indices		
		Hexagonal $hkil$	Rhomb. P $hkl$	Rhomb. F $hkl$
---	4.5790 <sup>a</sup> Å	0003	111	111
---	4.1536 <sup>a</sup>	10 $\bar{1}$ 1	100	1 $\bar{1}$ 1
25	3.6795	01 $\bar{1}$ 2	110	200
100	2.6973	10 $\bar{1}$ 4	211	202
50	2.5158	11 $\bar{2}$ 0	10 $\bar{1}$	2 $\bar{2}$ 0
---	2.3240 <sup>a</sup>	01 $\bar{1}$ 5	221	311
2	2.2895	0006	222	222
30	2.2050	11 $\bar{2}$ 3	210	3 $\bar{1}$ 1
---	2.1519 <sup>a</sup>	02 $\bar{2}$ 1	11 $\bar{1}$	3 $\bar{1}$ 1
2	2.0768	202 $\bar{2}$	200	2 $\bar{2}$ 2
40	1.8398	02 $\bar{2}$ 4	220	400
---	1.7893 <sup>a</sup>	10 $\bar{1}$ 7	322	313
---	1.7071 <sup>a</sup>	20 $\bar{2}$ 5	311	3 $\bar{1}$ 3
60	1.6933	11 $\bar{2}$ 6	321	402
4	1.6353	21 $\bar{3}$ 1	20 $\bar{1}$	3 $\bar{3}$ 1
---	1.6016	12 $\bar{3}$ 2	21 $\bar{1}$	4 $\bar{2}$ 0
6	1.5976	01 $\bar{1}$ 8	332	422
---	1.5263 <sup>a</sup>	0009	333	333
35	1.4851	21 $\bar{3}$ 4	310	4 $\bar{2}$ 2
---	1.4582 <sup>a</sup>	02 $\bar{2}$ 7	331	511
35	1.4525	30 $\bar{3}$ 0	2 $\bar{1}$ $\bar{1}$	2 $\bar{4}$ 2
---	1.4126	1235	320	5 $\bar{1}$ 1

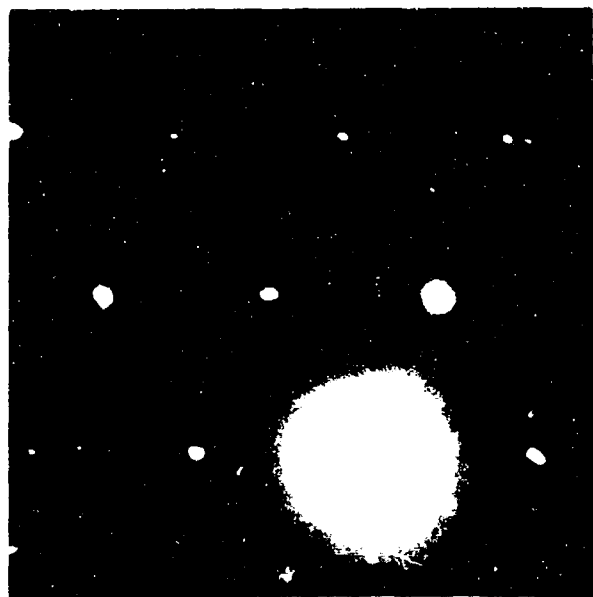
a. Absent for  $\alpha$ -Fe<sub>2</sub>O<sub>3</sub> for  $h\bar{h}0l$ :  $l = 2m$  required.

b. Calculated from the hexagonal dimensions,<sup>25</sup>  $a = 5.0317$ ,  
 $c = 13.737$  Å.





a



b

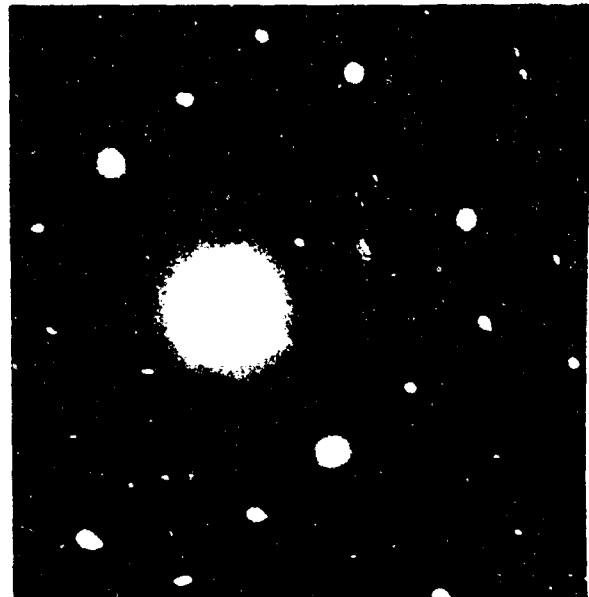
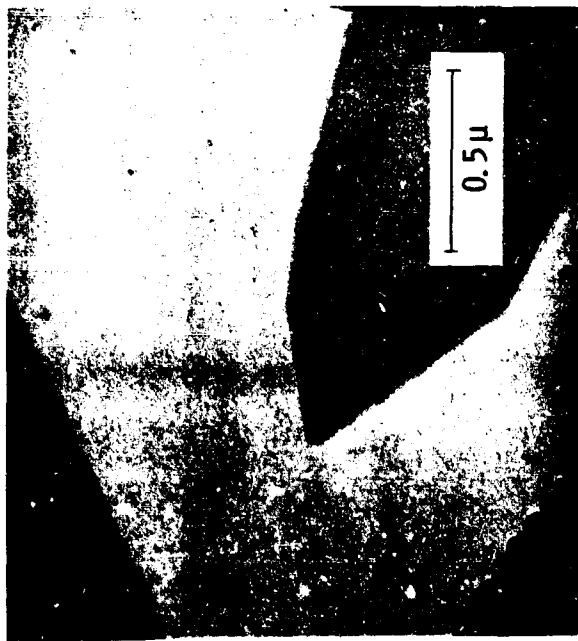


Fig. 13 - Selected-area electron diffraction of  $\alpha$ - $\text{Fe}_2\text{O}_3$  platelets, indexed with face-centered rhombohedron,  $\alpha = 85.7^\circ$ . Images rotated +145 to +148° relative to diffraction.



a



b

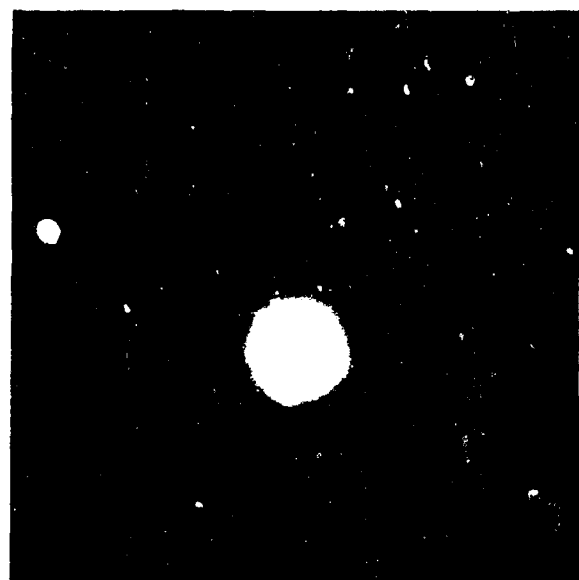
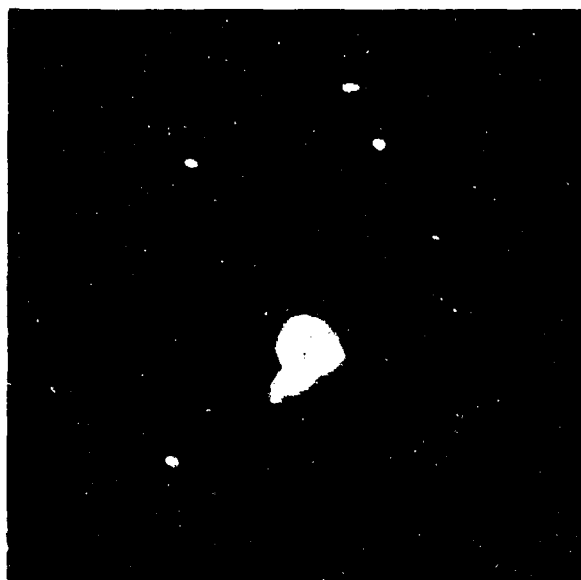


Fig. 14 - Selected-area electron diffraction of  $\alpha$ -Fe<sub>2</sub>O<sub>3</sub> platelets, indexed with face-centered rhombohedron,  $\alpha = 85.7^\circ$ . Images rotated + 145 to 148° relative to diffraction.



diagonal of a cube. Figure 16 shows at lower left the nearly hexagonal electron diffraction pattern, or cross section of the reciprocal lattice, obtained with the beam normal, or nearly normal, to the blade face. All the rods produce spots in all the patterns, and all the spots correspond to rods. Thus the diffraction patterns in general result from a tilt of the rods in the beam and are based on a correspondingly distorted and enlarged hexagon. To be precise, however, the curvature of the reflecting sphere results in the rows of the pattern being concave in the direction of the tilt of the blade face from the position normal to the beam.

The angle measured at the tip of the blade image can be calculated from the tilt, which can be calculated from the dimensions of the pattern. The images and patterns in every case conform at least approximately to the expected geometry, and the conformity is exact to well within the errors in measurement where calculations have been made. The indexing of the selected area diffraction patterns can be accomplished with the aid of a reciprocal lattice model, and with drawings of the reciprocal lattice nets normal to the growth axis, showing the nets for both twin orientations. The mirror plane intersects each such net in a mirror line normal to the reciprocal lattice rods. Thus the mirror twin of a reciprocal point lies on the same rod. The indexing was most readily accomplished by indexing two intense spots correctly as consistent with the growth axis projection, thus fixing the reflecting sphere approximately. Then each of the other intense spots was found at the intersection of the reflecting sphere with the appropriate rod of the appropriate drawing. Each drawing, or net, corresponds to a row of spots normal to the projection of the blade axis; and each rod of a drawing, to a point in the corresponding row.

Figure 13a shows the pattern obtained when the beam is nearly normal to the blade face, also illustrated in Figure 16. Figure 13b shows the pattern when the blade is tilted about its axis so that the beam is nearly normal to the three-fold axis. The twin indices, where they are necessary, given for twinning by two-fold rotation about the normal to the blade face, are underlined in all these patterns.

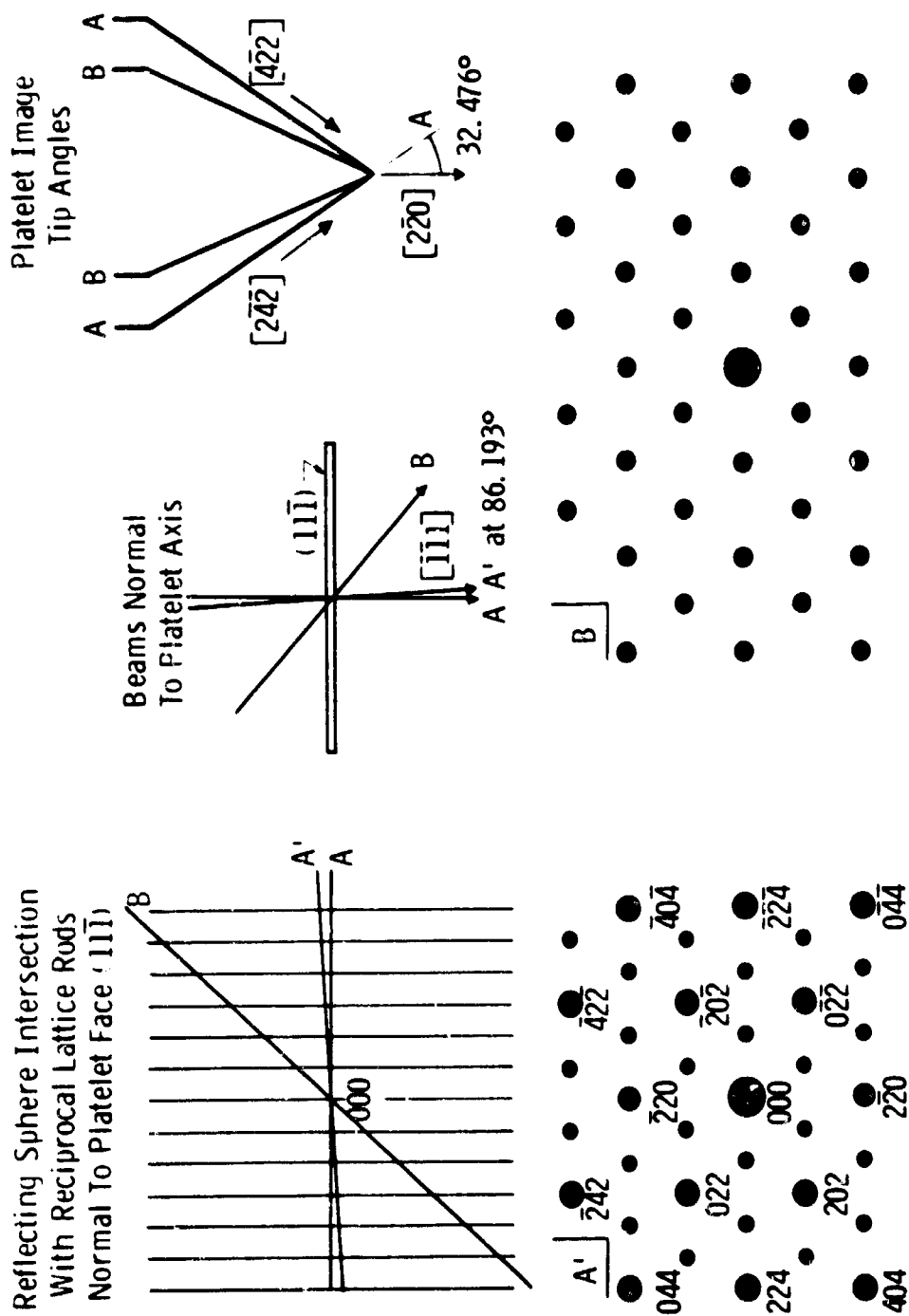


Fig. 16—Indexed spots in net normal to  $[111](\alpha\text{-Fe}_2\text{O}_3 \text{ rhombohedral F indexing})$ ; all other spots also observed.

Figure 14a results from a slight tilt of the blade approximately about  $[112]$  (normal to the blade axis and in the blade face). It is thus closely related to Figure 13a in dimensions and indexing. Figure 13b results from a slightly greater tilt approximately about  $[112]$ . The four central indexed spots are indexed the same in each case. Such anomalies are explained as follows: Only two geometrical (infinitesimal) points and the origin can lie on the reflecting sphere at once, and in general none lie exactly on the sphere (except the origin). The extent along the rods of the interference regions associated with the index points is believed to be the principal cause of the high intensities observed in so many spots. No tilting of the specimen stage was attempted--the patterns are for different blades as they were found.

The pattern of Figure 15a shows indexed point rows at a little less than  $90^\circ$  which would be found normal to one another (and indexed otherwise) in the untwinned lattice. Extreme distortion of the hexagonal pattern is illustrated in this figure. The "first layer line" in this pattern passes through  $\bar{2}02$  and  $200$ . Figure 15b shows another distorted hexagonal pattern. In this pattern,  $\bar{4}00$  to  $400$  is the zero layer line.

We conclude that most of the selected area diffraction patterns can be indexed only for two crystals with orientations related by mirroring on the blade face plane  $(11\bar{1})$ . The blade face has the corresponding indices,  $(\bar{1}101)$  and  $(010)$ , using the conventional structural hexagonal and rhombohedral unit cells. The twinning may be present, but is not required in indexing the patterns for a few special orientations, e.g. Figure 13a.

In order that the indices given refer to right-handed coordinate systems, the twins are related by a two-fold rotation about the normal to the twin plane. In the  $\alpha\text{-Fe}_2\text{O}_3$  blade-like platelet, the twins are also related by a two-fold rotation about  $[112]$ , which lies in the mirror plane normal to the blade axis,  $[\bar{2}20]$ .

The  $\alpha\text{-Fe}_2\text{O}_3$  blade-like platelet morphology is shown in Figure 17. In Figure 17, we use the more conventional structural rhombohedral unit cell for presenting the results. The blade face and blade axis are indexed also by the structural hexagonal unit cell.

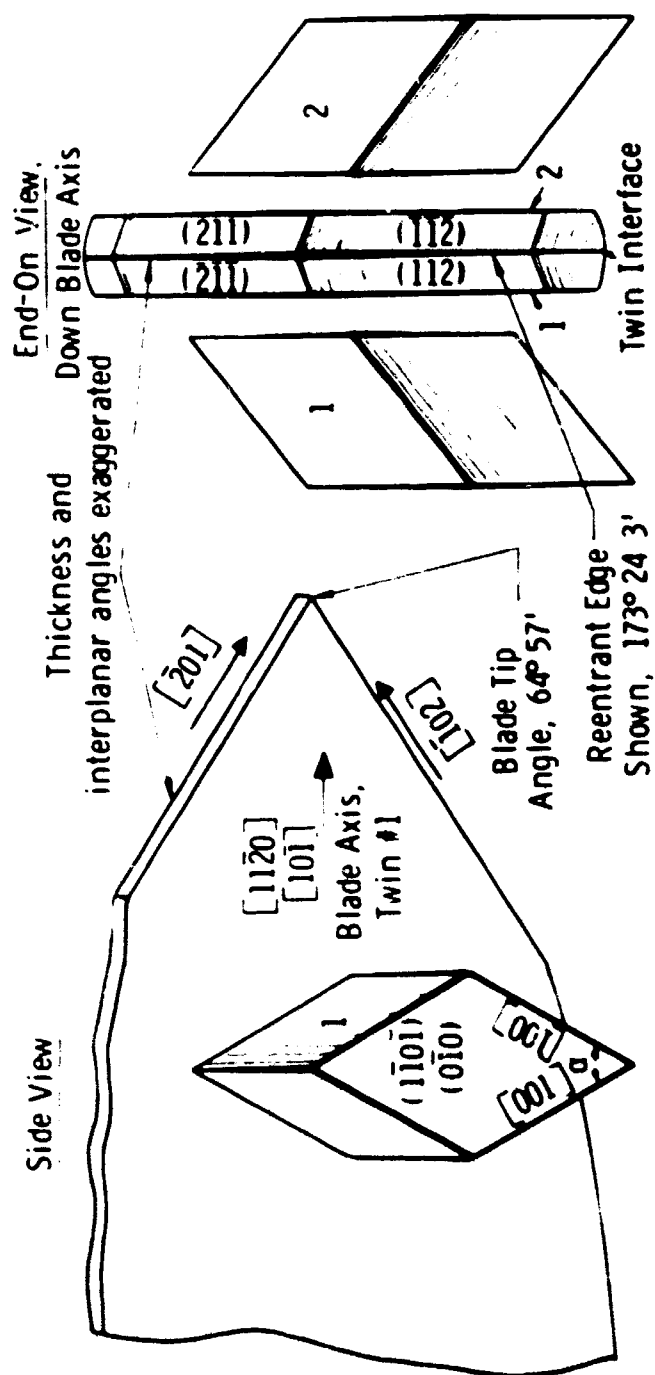
The orientation of the twins is shown in Figure 17. The blade tip angle, roughly determined from electron micrographs, indicates that the blade tip edges can be described as follows: In the face-centered rhombohedral F unit cell, the blade tip edges lie along  $[\bar{1}\bar{2}\bar{1}]$  and  $[2\bar{1}\bar{1}]$  directions. The blade tip angle is calculated to be  $64^\circ 57'$ , which compares to the  $60^\circ$  angle found in the cubic system. Figure 17 shows the blade tip edges lying along  $[\bar{2}01]$  and  $[\bar{1}02]$  in the structural rhombohedral unit cell.

The two blade tip edge directions are equivalent, but not with respect to the blade. The tip edge directions given are the intersections of planes in mirror orientation to one another which intersect in reentrant edges at one tip edge and non-reentrant edges at the other. These planes are indexed  $(202)$  and  $(0\bar{2}\bar{2})$  in the face-centered rhombohedral system, planes which are normal to  $(11\bar{1})$  in the cubic system. Figure 17 shows the indexing of the tip edge in the structural rhombohedral unit cell. The reentrant edge angle is  $173^\circ 24.3'$ .

### 5.3.3 Discussion of Platelet Morphology

General features of the blade-like platelet morphology remain undetermined. First, the number of twins has not been determined. There may be more than one twin interface. Second, the structure of the twin interface has not been determined. It is not known whether a mirror plane exists in the structure. (Only the twin orientations are known to be related by a mirror plane.) Third, the tip faceting has not been observed. The planes shown as facets in Figure 17 do not necessarily occur as facets.

Fig. 17— $\alpha$ - $\text{Fe}_2\text{O}_3$  pointed blade-like platelet morphology (actual number of twins is undetermined)  
Structural rhombohedral unit cell pictured,  $a = 5.4228 \text{ \AA}$ ,  $\alpha = 55^\circ 17'$



Unit cells as oriented in Twins 1 and 2.  
Twinning is by mirroring on (010), or  
by rotation about normal to (010), as  
indexed here, or by rotation about  
[101], all equivalent.



The asymmetry of the tip could explain an asymmetrical tip image for the case of a two-twin blade. For three twins, the structure would have a two-fold axis along its length, so that no asymmetry in the tip would be predicted.

Many blade images show a line down the center to the tip with usually uniform but different transmission of electrons on opposite sides of the line. This line appears to be the trace of the tip point. The asymmetry of the tip may result in a thickness difference because the growth mechanisms at the two tip edges are not identical. For example, growth steps may nucleate more readily at the reentrant edge. That the center line results only from the tip growth mechanism is suggested by the absence of this line for blades with rounded tips. The features of the blade faces result from thickness contrast and some thickness variations are traces of the tip edges.

Except for the effect of the apparent thickness variation across the center line, the uniform contrast of the well-formed unbent blades and the bend contours of the few highly bent blades suggest nothing more complex than the simple twinned morphology. The dark field images obtained show either the whole blade in nearly uniform contrast or bend contours, further confirming that the twins extend across the whole surface of the blade.

#### 5.3.4 Anomalous Diffraction

In addition to the reciprocal lattice rods on which lie all the  $\alpha\text{-Fe}_2\text{O}_3$ -indexed points, it appears from weak unindexed spots that parallel to each of these rods are two satellite rods. These satellite rods are positioned along the blade axis at one sixth of the repeat distance between the index rods. The reflections associated with these rods appear slightly elongated normal to the blade axis.

### 5.3.5 Comparison with Earlier Work

Bigot<sup>23</sup> and Talbot and Bigot<sup>24</sup> failed to correctly analyze their selected-area electron diffraction patterns of  $\alpha$ -Fe<sub>2</sub>O<sub>3</sub> blade-like platelets. Bigot<sup>23</sup> attributes diffraction patterns of blade-like platelets to  $\gamma$ -Fe<sub>2</sub>O<sub>3</sub> without presenting numerical data. They comment that the pattern dimensions are too small for the (0001) structural hexagonal plane of  $\alpha$ -Fe<sub>2</sub>O<sub>3</sub>. The indexing corresponds to a beam directed along [110] of cubic  $\gamma$ -Fe<sub>2</sub>O<sub>3</sub>. The expected angles for  $\alpha$ -Fe<sub>2</sub>O<sub>3</sub> are 60°, and for  $\gamma$ -Fe<sub>2</sub>O<sub>3</sub>, 54°44'.

The relative pattern dimensions are only slightly distorted from those to be expected for orientation of the beam parallel to the  $\alpha$ -Fe<sub>2</sub>O<sub>3</sub> [110] face-centered rhombohedral direction. A curvature of the rows parallel to [1120] or [220], (structural hexagonal and rhombohedral indices, respectively) results from the angle of the beam to the reciprocal lattice rods. This curvature is expected for a thin  $\alpha$ -Fe<sub>2</sub>O<sub>3</sub> crystal with (111) faces and with the beam along [110]. The direction of curvature indicates the (111) orientation in the beam. That the misalignment of the beam from [110] is not in the (1120) structural hexagonal plane follows from the fact that the symmetry of the intensities is lost and the pattern is skewed, or sheared, two degrees. The angle of 022 to 422 in the (011) plane of the cubic system is 54°44', whereas the corresponding angles by Bigot's indexing measured in Bigot's pattern are about 51°25' and 54°30'. The corresponding angles in  $\alpha$ -Fe<sub>2</sub>O<sub>3</sub> should be 53°49'. The measured angles differ from 53°49' as a result of the skewed nature of the pattern. This distortion also results in discrepancies of up to 3% in the relative d-spacings calculated from the pattern.

The corresponding spacings for  $\gamma$ -Fe<sub>2</sub>O<sub>3</sub> are about 13-16% greater than those for  $\alpha$ -Fe<sub>2</sub>O<sub>3</sub>. It would appear that such a variation in the instrument constant for selected area diffraction was accepted by Bigot in indexing the pattern as  $\gamma$ -Fe<sub>2</sub>O<sub>3</sub>.

Some of the details of the intensities in Bigot's pattern are not simply interpreted; but otherwise, the pattern can be indexed for  $\alpha\text{-Fe}_2\text{O}_3$ . Twinning is neither required nor precluded in this indexing.

#### 5.3.6 Novel Character of the $\alpha\text{-Fe}_2\text{O}_3$ Platelet Structure

Palache<sup>6</sup> et al. state that lamellar twinning on  $\{10\bar{1}1\}$  is common in natural corundum ( $\alpha\text{-Al}_2\text{O}_3$ , sapphire) and natural hematite ( $\alpha\text{-Fe}_2\text{O}_3$ ). The indices used are morphological hexagonal and are the indices of the morphological rhombohedral surfaces  $\{100\}$ . The twinning we have studied in  $\alpha\text{-Fe}_2\text{O}_3$  blade-like platelets is on the structural rhombohedral surfaces. These are the morphological hexagonal  $\{02\bar{2}1\}$  and morphological rhombohedral  $\{11\bar{1}\}$  planes.

We have not found any evidence in the literature for twinning on the rhombohedral planes of the structural rhombohedron for  $\alpha\text{-Fe}_2\text{O}_3$  or isomorphous minerals. We conclude that this is not a common twinning relation for the crystal growth mechanisms of minerals, which involve some type of deposition. We suggest that if the blade-like platelet growth proceeds by a surface transport mechanism, the same morphology should be found in minerals. That is, if the mobile species of a surface transport mechanism deposit  $\alpha\text{-Fe}_2\text{O}_3$  preferentially where the twin plane intersects the surface, the species of mineral deposition processes should find the same sites suitable for deposition. The nucleation of such twins might also be expected to be favored.

## 6. THE TRANSPORT MECHANISMS OF LOCALIZED GROWTHS

### 6.1 ARGUMENTS FOR INTERNAL DIFFUSION

Three mechanisms have been put forward for the growth of oxide whiskers: (1) surface diffusion to the tip of the whisker, (2) extrusion from the oxide, and (3) growth by internal diffusion in a hole or screw dislocation.

The possibility that the  $\alpha\text{-Fe}_2\text{O}_3$  whiskers or blades result from some extrusion process seems unlikely because the growths are so uniform and are apparently of high crystalline perfection. Furthermore Takagi<sup>4</sup> has observed growth from the tip.

It is also unlikely that  $\alpha\text{-Fe}_2\text{O}_3$  whiskers and platelets could grow by a surface transport mechanism, as suggested by Takagi,<sup>4</sup> from a surface with competing  $\alpha\text{-Fe}_2\text{O}_3$  surface growth mechanisms. The hypothesis of a surface growth mechanism would require that other growth mechanisms or the existence of  $\alpha\text{-Fe}_2\text{O}_3$  crystals growing by only mechanisms other than the mechanism of whisker tip growth be very limited. The existence of species and mechanisms for surface transport of iron sufficient to produce the rapid growth rates and the extreme lengths of the  $\alpha\text{-Fe}_2\text{O}_3$  whiskers is not known and is unlikely because of the stability of the  $\text{Fe}_3\text{O}_4$  from which the iron would be transported. Furthermore, the nucleation of  $\alpha\text{-Fe}_2\text{O}_3$  on  $\text{Fe}_3\text{O}_4$  is a common phenomenon and involves only a change from cubic close-packing to a distorted hexagonal close-packing of oxygen in the  $\alpha\text{-Fe}_2\text{O}_3$  lattice together with a change in the iron positions. One cannot readily propose that the driving force for rapid diffusion to the  $\alpha\text{-Fe}_2\text{O}_3$  whisker tips can be provided by high concentrations of iron species mobile on the  $\text{Fe}_3\text{O}_4$  surfaces.

There is evidence that surface transport is negligible in the absence of growth about the areas of contact between whiskers or blades which touch one another. This is readily observable for pairs of whiskers which grow about one another in a loose spiral. A reduction of surface free energy should provide the driving force for growth about some of the areas where the whiskers are in contact. Areas of contact might provide ready sites for the nucleation of growth on the whisker surfaces. No such local thickening or growth between the whiskers is observed, however.

The vapor transport of iron by species resulting from the reaction of  $\text{Fe}_3\text{O}_4$  or  $\text{Fe}_2\text{O}_3$  with oxygen or water vapor (except for high density steam) is not a commonly recognized phenomenon. That the long history of technical application and laboratory experimentation with iron and steel has failed to introduce into the literature readily available evidence of such vapor transport provides a good argument that no important vapor transport exists.

Rapid growth rates of about  $10^{-6}$  cm/sec would require an iron species vapor pressure at  $500^\circ\text{C}$  of at least about  $10^{-4}$  torr. This is based on the incidence rate on 100 times the growing surface, with an accommodation coefficient of one. Realistic estimates would be higher. Excluding the possibility of surface diffusion would alone increase the estimate to  $10^{-2}$  torr, much more than could have remained undetected.

## 6.2 GROWTH RATES

Good measurements of the growth rates of oxide whiskers or platelets are not yet available. Pease and Ploc<sup>27</sup> have observed initial growth rates at  $500^\circ\text{C}$  of over  $0.2 \mu/\text{min.}$ , an average rate over five minutes. Takagi<sup>4</sup> observed growth rates up to  $2 \mu/\text{min.}$  at  $700^\circ\text{C}$  in the first minute. Whether the growth observed in these cases should be classified as whiskers or platelets cannot be determined from the information given.

### 6.3 GROWTH OF WHISKERS WITH AXIAL SCREW DISLOCATIONS

The morphological studies presented demonstrate that the most simple oxide whiskers are single crystals of high crystalline perfection and show axial twist. The latter property is strong evidence for a screw dislocation at the center of the whisker. Fig. 18 shows a model for the whisker growth on iron. The whisker contains an internal hole or screw dislocation core where grain boundary or internal surface diffusion of iron occurs along a gradient in chemical potential.

Most of the growth occurs by reaction with oxygen atoms or ions at the tip of the whisker. Since the diameter is nearly uniform, it follows that cationic mobility is much smaller in the lattice than along the dislocation.

The structure of the sections where the cation diffusion rate is high cannot be given at this time. It may be that information on these structures is contained in the anomalous diffraction. The structure in the immediate vicinity of the screw dislocation must show ions either displaced by the strain into some distortion of the  $\alpha\text{-Fe}_2\text{O}_3$  structure, or otherwise positioned, possibly in some disordered structure. In either type of structure, diffusion coefficients would be expected to be different from those in the much less distorted structure of more than half of the cross section of the whisker. This outer region probably exhibits the bulk or lattice ionic diffusion coefficients.

Appendix IX describes the lattice distortion in a rod with an axial screw dislocation.

#### 6.3.1 Estimation of the Diffusion Coefficients for Axial Diffusion in Whiskers

Appendix XII provides values for the chemical potential difference driving the transport of iron which results in whisker (and platelet) growth. Appendix XIII provides the relationship whereby the flux and the driving force can be used to calculate a diffusion coefficient,

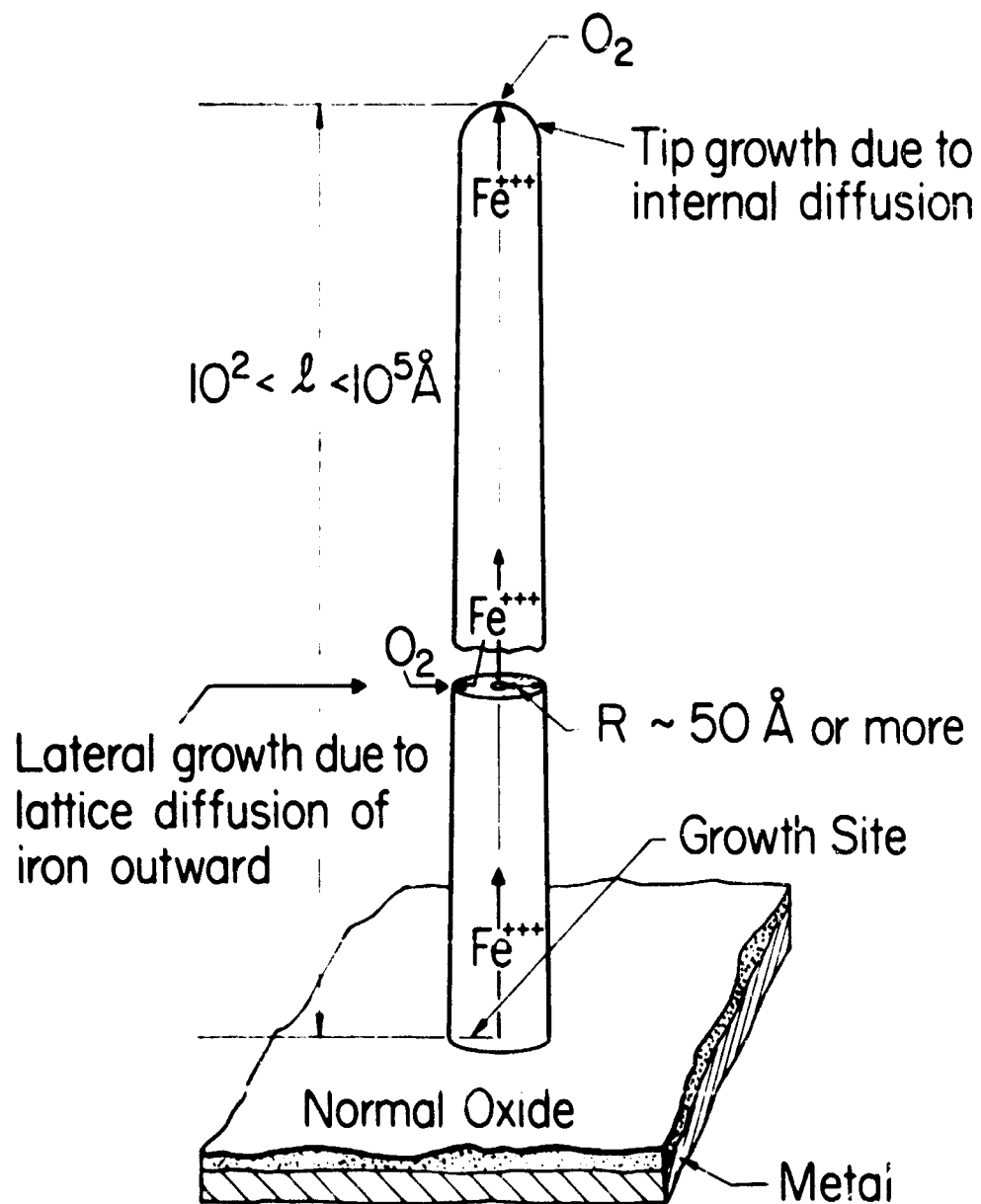


Fig. 19—Model of whisker growth during the oxidation of iron at 400°C in dry  $O_2$

$$D_i = - \frac{RTJ}{n_i \frac{\partial \mu_i}{\partial x}} \left( 1 + \frac{\partial \ln \gamma_i}{\partial \ln n_i} \right). \quad (1)$$

Rewriting in terms of atomic energies, we have

$$D_i = - \frac{NkT}{\frac{\partial \mu_i}{\partial x}} \left( \frac{J}{n_i} \right) \left( 1 + \frac{\partial \ln \gamma_i}{\partial \ln n_i} \right). \quad (2)$$

This could be usefully rewritten by substituting, from Appendix XII,

$$\frac{\partial \mu_i}{\partial x} = \frac{\Delta \mu_i}{\Delta x} = - \frac{n_2}{n_1} RT \frac{\Delta \ln p_{O_2}^{1/2}}{\Delta x}.$$

The value of the flux of iron atoms,  $J$ , can be calculated from the whisker growth rate,  $\dot{l}$ , and an arbitrary cross section for the dislocation core,  $\pi r^2$ , as follows:  $J = \dot{l} (Z/r)^2$ , where  $n$  is the number density of iron atoms in  $\alpha\text{-Fe}_2\text{O}_3$ ,  $3.984 \times 10^{22} \text{ cm}^{-3}$ , and  $Z$  is the radius of the whisker. The value of  $n_i$  varies with the chemical potential; however, one may make use of an approximation  $n_i = n$  for the calculation of  $D$  from (2). Note that  $(J/n_i)$  is the arrival rate of iron atoms,  $J\pi r^2$ , divided by the number density along the dislocation line,  $n_i \pi r^2$ . Such a concentration, in atoms  $\text{cm}^{-1}$ , could be used to eliminate the arbitrary core cross section.

The core of the dislocation need not have the composition of the perfect lattice (however, local equilibrium would mean local equality of ionic activities). The variation in chemical potential along the core may simply correspond to a variation in the iron concentration,  $n_i$ , increasing from the tip to the base. If the structure of the core is an ordered one, and if it has a constant repeat distance along the dislocation, then a smaller  $n_i$  near the tip would mean iron vacancies in the core lattice. Iron vacancies are accompanied by positive holes ( $\text{Fe}^{+4}$ ,  $\text{O}^-$ , or  $\text{O}_2^-$ ) or a decrease in the number of free electrons ( $\text{Fe}^{++}$ ). If, on the



other hand, the core does not have an ordered structure, these electronic species would not necessarily be associated with vacancies. The iron atom motion might be described by cooperative atomic movements rather than by vacancy movement. In addition to diffusion, a liquid-like core might flow in a pressure gradient, with both iron and oxygen moving to the tip.

Whatever the real mechanism, it is useful to estimate the diffusion coefficient for comparison with diffusion data. We do not have good values of  $J$  and  $Z$  as functions of  $t$  and  $T$ . We will estimate  $\dot{i} = 10^{-6}$  cm sec $^{-1}$  and  $Z = 10^{-6}$  cm at  $t = 10^{-4}$  cm, for  $T = 800^\circ\text{K}$ . This is a somewhat arbitrary, probably high estimate of the largest growth rate to be expected. Comparing the data given by Takagi,<sup>4</sup> the diffusion coefficient calculated from these data might be large by a factor of ten because  $\dot{i}$  and  $Z$  are larger than might be the case.

The average speed of the iron atoms along the dislocation is

$$J/n = \dot{i} (Z/r)^2 = 10^{-6} \text{ cm sec}^{-1} 10^4/3^2 \\ = 1.11 \times 10^{-3} \text{ cm sec}^{-1},$$

where  $r = 3 \times 10^{-8}$  cm has been chosen arbitrarily as the core radius.

From Appendix XII,  $\Delta u_1/N = -3.09 \times 10^{-12}$  ergs/atom Fe. Taking  $\Delta x = r$ , (although  $\Delta x > r$ ), we have

$$- \frac{1}{N} \frac{\partial u_1}{\partial x} = - \frac{1}{N} \frac{\Delta u_1}{\Delta x} = 3.09 \times 10^{-8} \text{ dynes.}$$

Assuming  $\frac{J \ln \gamma_{\text{Fe}}}{\ln n_{\text{Fe}}} = 0$ , and substituting in equation (2), we have, for iron in the whisker core,

$$D_w = \frac{1.38054 \times 10^{-16} \text{ erg } ^\circ\text{K}^{-1} \cdot 800^\circ\text{K} \cdot 1.11 \times 10^{-3} \text{ cm sec}^{-1}}{3.09 \times 10^{-8} \text{ dynes}} \\ = 3.97 \times 10^{-9} \text{ cm}^2 \text{ sec}^{-1}$$

The mobility is  $B_W = D_W/kT = \frac{1.11 \times 10^{-3} \text{ cm/sec}}{3.09 \times 10^{-8} \text{ dyne}} = 3.59 \times 10^4 \text{ cm sec}^{-1} \text{ dyne}^{-1}$ .

The electrical conductivity of the ferric ions of this arbitrary core cross section is calculated to be  $33.0 \text{ ohm}^{-1} \text{ cm}^{-1}$ . The electrical conductance by the iron in a length of core may be greater, under some conditions, than the electronic conductance of the whisker.

### 6.3.2 Comparison with Measured Diffusion Coefficients for Iron in $\alpha\text{-Fe}_2\text{O}_3$

Hagel<sup>28</sup> provides a review of data on ionic diffusion in hematite. He quotes the lattice diffusion coefficient of iron,  $4 \times 10^5 \exp(-112,000/RT)$ , determined by Lindner.<sup>29</sup> Values calculated from this expression are  $4.28 \times 10^{-30} \text{ cm}^2 \text{ sec}^{-1}$  and  $1.00 \times 10^{-25} \text{ cm}^2 \text{ sec}^{-1}$  at 700°K and 800°K, respectively.

If one assumes that the diffusion in dislocations (both edge and screw) is effectively that through  $10^8 \text{ cm}^{-2}$  screw dislocations normal to the cross section, then the diffusion coefficient normal to the cross section, at 800°K, is  $10^8 \text{ cm}^{-2} \times (3 \times 10^{-8} \text{ cm})^2 \times 3.97 \times 10^{-9} \text{ cm}^2 \text{ sec}^{-1} = 1.12 \times 10^{-15} \text{ cm}^2 \text{ sec}^{-1}$ . This is greater than the extrapolated lattice diffusion coefficient,  $10^{-25} \text{ cm}^2 \text{ sec}^{-1}$ , by a factor of  $10^{10}$ , and is equal to that measured by Lindner<sup>29</sup> at about 1200°K (926.85°C).

This value,  $10^{-15} \text{ cm}^2 \text{ sec}^{-1}$ , exceeds values of the diffusion coefficient measured by Coble<sup>30</sup> below 950°C (1223.15°K) using the shrinkage on sintering. At 750°C (1023.15°K), Coble measured a diffusion coefficient of  $10^{-18} \text{ cm}^2 \text{ sec}^{-1}$ , much less than the  $10^{-15} \text{ cm}^2 \text{ sec}^{-1}$  calculated above for 526.85°C (300°K). Thus screw dislocations with diffusion characteristics like those in the whiskers did not add significantly to the diffusion measured. Since the  $\text{Fe}_2\text{O}_3$  particles used by Coble averaged only 1300 Å in diameter, simple dislocations could be

effective only in rare instances of small-angle grain boundaries between the particles. The particles were too small to contain significant concentrations of dislocations.

In the case of Lindner's measurements<sup>29</sup> in the range 950° to 1250°C, the tracer diffusion measured may have been essentially lattice diffusion even in the presence of a significant dislocation density. This might result if the diffusion in the dislocation were like that along an idealized row of atoms, for which the correlation factor<sup>31</sup> is ideally zero. Such would be the case if the vacancies associated with a dislocation were confined to a row, i.e., the vacancy distribution outside the row would be uniform.

A further hypothesis required to explain the small measured diffusion coefficients is that neither edge dislocations nor grain boundaries in general provide paths for diffusion with diffusion coefficients comparable to that calculated for whisker diffusion. If the twin boundary of the platelet provides a comparable diffusion path, one would expect the same of other grain boundaries. It seems excessive to hypothesize that the correlation factors are near zero for all dislocations and grain boundaries.

### 6.3.3 Comparison with Diffusion Coefficients in Other Materials

Hauffe<sup>32</sup> provides tables of diffusion coefficients including pre-exponential factors  $D_0$  cm<sup>2</sup> sec<sup>-1</sup> and activation energies  $AD$  kcal/g-atom. The diffusion coefficient for iron in the whisker core,  $D_w$ , was estimated above to be about  $4 \times 10^{-9}$  cm<sup>2</sup> sec<sup>-1</sup>. This was judged to be probably large, because the growth rate was purposefully chosen large. Nevertheless, many diffusion coefficients can be calculated to be as great or greater at 800°K. Some of these are for interstitials, for which no vacancies need be created. Others are for matrices which apparently have large vacancy concentrations and small activation energies for vacancy migration. These materials are soft, or may be near a melting point or other transition. It may be that some of the diffusion coefficients

Hauffe lists were incorrectly measured, and some may show large grain boundary or dislocation diffusion. Table 8 lists data from Hauffe together with calculations of diffusion coefficients at 800°K from the  $D_0$  and  $AE$  values. This data suggests that the value  $4 \times 10^{-9} \text{ cm}^2 \text{ sec}^{-1}$  is not excessive. The core can be considered to provide easy iron mobility and a high effective vacancy concentration.

Such a large diffusion coefficient may be unknown for triply-charged cations in solid oxides. Grieveson and Turkdogan<sup>13</sup> estimate from data on molten FeO the self-diffusivity of iron at 1550°C to be  $(1.5 \pm 0.5) \times 10^{-6} \text{ cm}^2 \text{ sec}^{-1}$ . If this is written  $1.46 \times 10^{-4} \exp(16,800 \text{ cal/mole/RT})$ , the value at 800°K is  $3.97 \times 10^{-9} \text{ cm}^2 \text{ sec}^{-1}$ . We have no compelling argument for such an activation energy. The values calculated from Hauffe's table for FeO and Fe<sup>2+</sup> at 800°K are in the range of  $D_w$ . This suggests that the whisker diffusion need not involve special mechanisms such as the crowdon mechanism, or flow in a pressure gradient.

It should be kept in mind, however, that the whisker growth rate, the core cross section, and therefore,  $D_w$ , are not known accurately. It remains to be seen whether  $D_w$  can be predicted satisfactorily from some acceptable model of the core structure.

#### 6.3.4 Consideration of Radial Growth by Lattice Diffusion

Equation (7) of Appendix XIV gives the time required for a whisker to grow by radial diffusion of iron from radius  $Z_0$  to  $Z$ .

$$t - t_0 = \frac{2 r^2 [x^2 (\ln x - 1/2) - x_0^2 (\ln x_0 - 1/2)]}{3 D_1 \ln p_{O_2}}$$

where  $r$  is the radius of the core, in which  $a_1$  is constant,  $x = (Z/r)$ , and  $x_0 = (Z_0/r)$ . Assuming equilibrium with the oxygen in air at the surface,  $\log_{10} p_{O_2} = -0.678$ . Assuming equilibrium with  $\text{Fe}_3\text{O}_4$  at the core provides a maximum activity gradient and a minimum time. Table 9 lists values of  $D_1 = 4 \times 10^{-5} \exp(-112,000/RT)$  and  $\log_{10} p_{O_2}$  between

TABLE 8

Diffusion Coefficient Data from Hauffe  
(Calculated Values in Parentheses)

Diffusing Metal	Medium	Range t °C	$D_0$ cm <sup>2</sup> sec <sup>-1</sup>	$\Delta U$ kcal mole <sup>-1</sup>	$D$ cm <sup>2</sup> sec <sup>-1</sup>	T °K
---	---	---	---	---	---	---
Cd <sup>++</sup>	AgBr	2-4 mol %	---	---	$0.9 \times 10^{-4}$	672
Pb <sup>++</sup>	AgCl	0.63 mol % PbCl <sub>2</sub>	---	---	$2.4 \times 10^{-7}$	542
Sb <sup>+++</sup>	AgSbS <sub>2</sub>	---	---	---	$4 \times 10^{-7}$	673
Cu	Ge	700-900	$1.9 \times 10^{-4}$	4.1	$(1.4 \times 10^{-5})$	800
Li	Ge	---	$2.5 \times 10^{-3}$	11.8	$(1.2 \times 10^{-3})$	800
Fe	Si	900-1400	$6.2 \times 10^{-3}$	20.0	$(2.2 \times 10^{-8})$	800
K <sup>+</sup>	SiO <sub>2</sub>	300-500	0.18	31.7	$(4.0 \times 10^{-10})$	800
Ag <sup>106</sup>	$\alpha$ -Ag <sub>2</sub> SO <sub>4</sub>	430-700	2.4	26.7	$(1.3 \times 10^{-7})$	800
Ag <sup>106</sup>	$\beta$ -Ag <sub>2</sub> S	179	$1.4 \times 10^{-2}$	11.1	$(1.4 \times 10^{-5})$	800
Ag <sup>106</sup>	$\alpha$ -Ag <sub>2</sub> S	200-400	$2.8 \times 10^{-4}$	3.45	$(3.2 \times 10^{-4})$	800
Fe <sup>55</sup>	CaFe <sub>2</sub> O <sub>4</sub>	800-1200	0.4	72.0	$(0.9 \times 10^{-20})$	800
Fe <sup>55</sup>	FeO	699-983	0.118	29.7	$(0.9 \times 10^{-9})$	800
Fe <sup>55</sup>	Fe <sub>3</sub> O <sub>4</sub>	799-987	5.2	55.0	$(5.2 \times 10^{-15})$	800
Fe <sup>55</sup>	$\alpha$ -Fe <sub>2</sub> O <sub>3</sub>	900-1300	$4.0 \times 10^5$	112.0	$(1.0 \times 10^{-25})$	800
Fe <sup>55</sup>	ZnFe <sub>2</sub> O <sub>4</sub>	800-1300	$8.5 \times 10^2$	82.0	$(1.9 \times 10^{-20})$	800
Fe <sup>55</sup>	FeS	799-900	$(1.2 \times 10^{-3})$	(20.4)	$(3.16 \times 10^{-9})$	800

air and the  $\text{Fe}_3\text{O}_4$  interface. Times are given, for growth by radial lattice diffusion of iron, from a radius  $Z_0 = 100\text{\AA}$  to  $Z = 150\text{\AA}$ , for core radii  $r = 3, 10, \text{ and } 30\text{\AA}$ .

TABLE 9  
Radial Growth by the Lattice Diffusion of Iron

T°K	t°C	$D_1$	$\Delta \log_{10} P_{O_2}$	Times $t-t_0$		
				3 $\text{\AA}$	10 $\text{\AA}$	30 $\text{\AA}$
800	526.85	$1.00 \times 10^{-25}$	16.190	26,300	17,800	10,100 yrs
1100	826.85	$2.23 \times 10^{-17}$	7.554	134	90.6	51.3 min
1200	926.85	$1.60 \times 10^{-15}$	5.666	2.49	1.69	0.956 min

This calculation, which assumes the maximum  $D_1$  independent of oxygen activity, shows the dependence of the rate of radial growth on the choice of  $r$  to be relatively unimportant. At 800°K, essentially no radial growth occurs in the minutes or hours of reaction time. Any tapering of the whiskers should not be ascribed to lattice diffusion except perhaps near the high temperature limit. In the absence of lattice and surface diffusion, the whisker cross section defines an effective tip cross section. That is, the shape of the whisker behind an effective tip length has been determined for the duration of oxidation in the laboratory. Takagi<sup>4</sup> measured a smooth increase in minimum whisker thickness from about 60 $\text{\AA}$  at 450°C to 650 $\text{\AA}$  at 900°C. This and Takagi's further observations on whisker thicknesses may be explained as the result of diffusion from the core to the edge of the tip carrying iron farther at higher growth rates to give greater thicknesses.

The upper limit of temperature for the observation of whiskers, 900°C, may result from the effect of radial lattice diffusion of iron. Radial lattice diffusion would decrease the iron activity gradient along the whisker core, thus decreasing the length growth rate. It may be that iron lattice diffusion affects the unknown process which delivers iron to the base of the whisker.

Hagel<sup>28</sup> has measured the diffusion of oxygen in  $\alpha$ -Fe<sub>2</sub>O<sub>3</sub>. His value,  $D_2 = 2.04 \exp(-77,900/RT)$ , was measured in the temperature range 900-1250°C at 125 torr oxygen pressure. He assumes  $D_2$  varies as  $p_{O_2}^{-1/6}$  according to the equation,



Salmon,<sup>34</sup> however, has found his  $\alpha$ -Fe<sub>2</sub>O<sub>3</sub> composition data to be interpreted by a relation which would give  $p_{O_2}^{-1/4}$  dependence. It is not clear that this relation has been determined unambiguously by Salmon. His derivation refers to iron interstitials rather than to oxygen vacancies, whereas we assume the latter here.

The value of  $D_2$  at 800°K and 125 torr according to Hagel's  $D_2 = 2.04 \exp(-77,900/RT)$  is  $1.07 \times 10^{-21} \text{ cm}^2 \text{ sec}^{-1}$ . Pressure dependence  $p_{O_2}^{-1/6}$  and  $p_{O_2}^{-1/4}$  give values  $5.12 \times 10^{-19}$  and  $1.10 \times 10^{-17} \text{ cm}^2 \text{ sec}^{-1}$ , respectively at  $p_{O_2} = 10^{-16.868}$ , the equilibrium pressure at the Fe<sub>3</sub>O<sub>4</sub>-Fe<sub>2</sub>O<sub>3</sub> interface. Thus  $D_2$  may be greater than  $D_1$  by a factor of  $5 \times 10^6$  to  $1.1 \times 10^8$  at that interface. An upper limit on the diffusion of oxygen into the whisker can be obtained by taking the maximum  $D_2$ , which is that at the Fe<sub>3</sub>O<sub>4</sub> interface, and the maximum activity gradient. As before, the core is assumed to have the Fe<sub>3</sub>O<sub>4</sub> interface activity. This upper limit on the oxygen diffusion rate into the  $r = 3 \text{ Å}$  core of a whisker of 130 Å radius at 800°K is equivalent to a fractional increase in cross section per hour of  $1.08 \times 10^{-2}$  or 0.236 for pressure dependences of  $p_{O_2}^{-1/6}$  and  $p_{O_2}^{-1/4}$ , respectively. These values are equivalent to the growth of cylinders of 3.5 Å and 16 Å diameter, respectively, at the core per minute.

Assuming a constant activity gradient along the core length, the  $p_{O_2}^{-1/4}$  oxygen diffusion upper limit for a  $\mu$  whisker of 130 Å radius growing at 0.355  $\mu$ /min is equivalent to 0.56% of the iron diffusion along the core. Thus the radial oxygen lattice diffusion at 800°K is not necessarily expected to decrease significantly the iron activity gradient along the core. At about 850°C, however, the lattice diffusion of oxygen

in  $\alpha\text{-Fe}_2\text{O}_3$  at its lower limit in equilibrium with air could produce a radial diffusion rate into the whisker core equivalent to the rate of axial diffusion of iron. Thus it may be the oxygen lattice diffusion which determines the upper temperature limit for whisker growth by eliminating the iron activity gradient. This effect may be evidenced by the decrease in whisker growth rate with increasing temperature above 700-750°C found by Takagi.<sup>4</sup> Whether oxygen diffuses rapidly along the whisker core is not suggested by the whisker growth phenomenon and is not known otherwise.

#### 6.4 THE TRANSPORT MECHANISMS FOR BLADE-LIKE PLATELET GROWTH

The blade-like platelets grow by the internal transport of iron to the tip. Their limited thickness can readily be understood as a result of internal diffusion along a plane interface. Platelet thickness would be expected to taper from the base if platelets grew by surface diffusion. Platelet surfaces, as revealed by thickness contours, are commonly at least slightly imperfect, so that further growth could occur readily; but platelets generally appear uniform in thickness along the lengths observed.

The model for growth of blade-shaped oxide platelets is shown in Figure 17. The platelet must contain one or more twin interfaces. These provide paths for the internal diffusion of iron atoms which results in the growth.

The flat elongated structure of the blade-like platelets indicates that there are several ionic diffusion coefficients operating. The lattice diffusion of iron normal to the blade face is small, so that the blade remains thin. The transport at the twin interface normal to the blade axis is greater; so that the blade grows more broad as it grows longer. The transport at the twin interface and along the blade axis is greatest, so that the blade grows long. Transport over the tip surface is small, so that the blade grows thin.



Since the ferric ions fill only two-thirds of the octahedral holes in  $\alpha\text{-Fe}_2\text{O}_3$ , the remaining holes are available for diffusion of ferric ions. At the twin interface holes may be positioned more favorably for iron atom diffusion than in the perfect  $\alpha\text{-Fe}_2\text{O}_3$  structure. The paths along the blade axis are far more favorable. A convincing model for the twin interface allowing rapid diffusion in one direction is needed. The twin interface acts like a row of dislocations in allowing rapid growth in one direction.

## 7. SUMMARY OF INFORMATION ON GROWTH MORPHOLOGY AND MECHANISMS

The whiskers and blade-like iron oxide platelets observed by electron microscopy to have grown so as to extend out of the oxide films on the surface of pure iron have been studied. Electron diffraction from the oxidized surface by large numbers of these growths show that the outgrowths consist of  $\alpha\text{-Fe}_2\text{O}_3$ . Such fiber-texture patterns show the fiber axis to be  $[\bar{1}\bar{1}20]$ , in agreement with the selected-area electron diffraction patterns. The latter show also that the whiskers have an axial twist and that the blades are twinned on the blade face plane, the (010) structural rhombohedral surface. The straight edges at the blade tip have prominent crystallographic directions. The asymmetry of the blade image in outline and in contrast corresponds to the asymmetry of the twinned structure. The most simple whiskers have a single axial screw dislocation with a  $5.03 \text{ \AA}$  Burgers vector. The whiskers are distinguished from the platelets by their whisker-like shape. These shape differences are believed to correspond to the structural differences we have determined, the whiskers having axial screw dislocations without twinning, and platelets having twinning without dislocations.

It has not yet been determined, however, that the rounded platelets which show bend contours have the same twin structure as the blades, and the bending is not understood.

Anisotropy in the diffusion of iron in the twin interface, together with apparently negligible lattice diffusion of iron, is believed to result in the blade shape. Iron leaving the interface at the tip is incorporated into growth on the tip edge surfaces. Similarly, in the case of the whisker, iron is transported in the screw dislocation core.

Some lattice diffusion of iron is suggested by a slight candle-like taper. However, the radial lattice diffusion of iron predicted from measurements at higher temperatures is not significant except in a small temperature range below about 900°C, above which whiskers are not observed. Much more diffusion of oxygen is predicted. Oxygen diffusion may decrease the growth rate, especially above about 700°C.

That water vapor is necessary for the development of platelet growth is interpreted as an effect on the growth site. Determination of the nature of the growth site and the driving forces would permit a more satisfactory appraisal of the significance of these growths.

## 8. HIGH VACUUM SYSTEM DEVELOPMENT

Fig. 19 shows the vacuum system as it has been rebuilt. This rebuilding was desirable primarily to replace the zeolite and copper foil traps with liquid nitrogen traps. Zeolite and copper traps are ineffective during bakeout, and require bakeout for reactivation. As a consequence of this modification feature, the metal specimen surfaces will be protected from exposure to the diffusion pump oil during the bakeout.

Defective valves were replaced with better valves, and larger tubing, 1" and 1-1/4" O.D., was used where possible. The number of valves was reduced, and the hydrogen leak was brought into the bakeout oven.

Furthermore, the water reservoir was rebuilt with short large-diameter tubing so as to allow more rapid freezing-out of water in successive purification steps. Fig. 19 shows the system after the water has been introduced and the glass line to the water reservoir closed. Lines in the section with the water reservoir are then heated with tapes and the valves in that section remain closed.

The section marked "Specimen Counterweights" is a manifold of six hanging tubes in which glass-encapsulated magnets hang on wires running to the specimens. Magnets on the outside are used to raise and lower the specimen tubes in the reaction tube. The specimens are fixed in short pieces of fused quartz tubing. The specimens now in use are 0.1 inch wide iron foil ribbons.

Doc. d. 3632

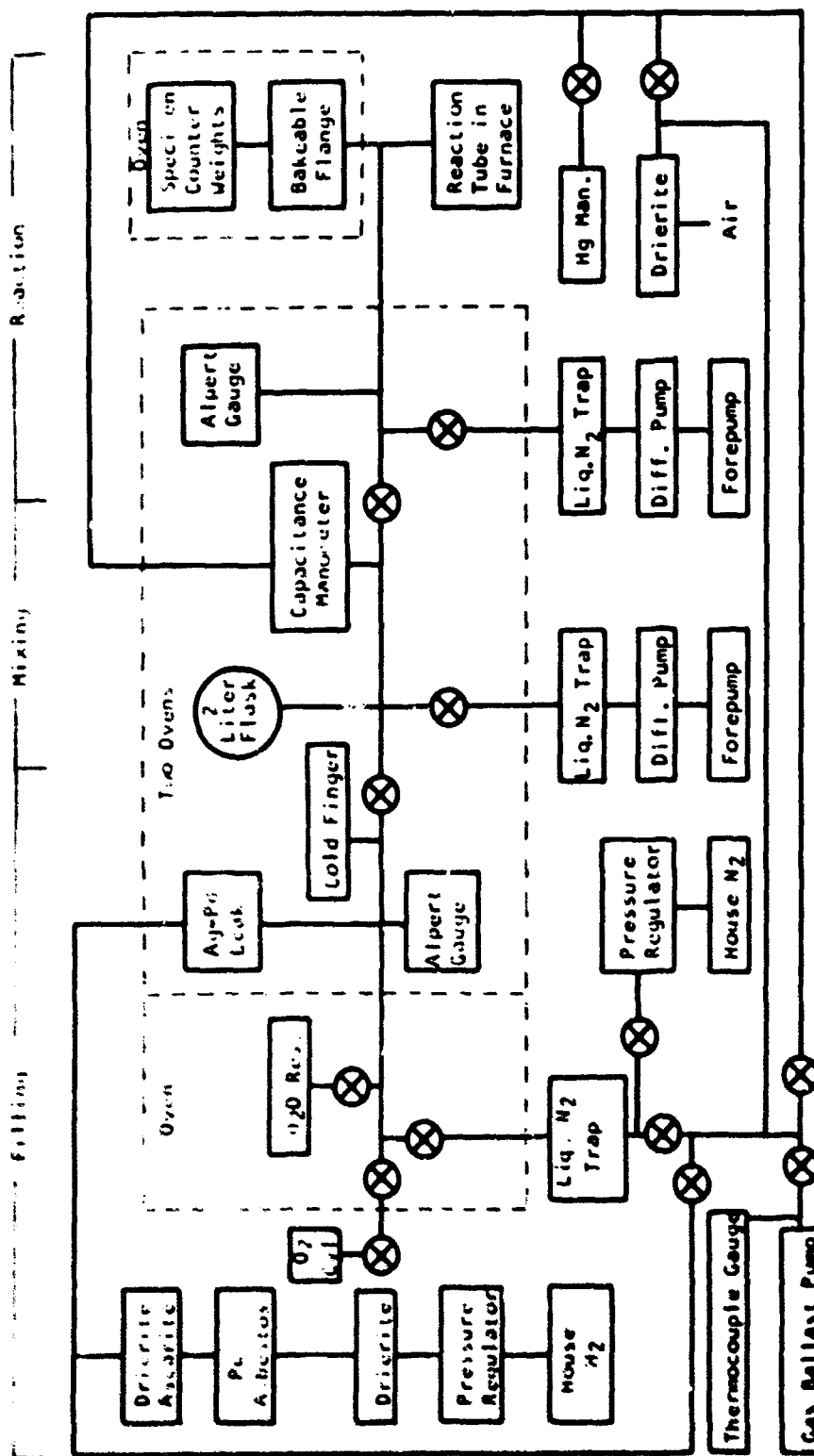


Fig. 19—High vacuum system for  $H_2O-O_2$  oxidation

## 9. REPLICA DEVELOPMENT

Attempts were made to dissolve the iron foil from one side in such a way as to leave the oxide and replica on the other side supported by a grid of iron. Some progress was made, but the advantages of such a specimen appear to be outweighed by the difficulties in specimen preparation.

Some success has been achieved with a stiff cellulose acetate replicating film. After platinum shadowing and carbon replica deposition on the oxidized surface, the specimen foil is cut into short sections for anodic stripping. Squares of film wet with a solution of cellulose acetate in chloroform (or any suitable solution) are pressed onto the specimen surfaces. Then a platinum wire loop is attached to a scraped edge of the foil with silver conducting paint. Anodic stripping of the oxide and replica in saturated potassium chloride solution<sup>35</sup> with such a specimen leaves the oxide and replica supported by the plastic film. The cellulose acetate pieces are placed, replica side down, on 200-mesh copper grids for electron microscopy. Acetone dissolves the cellulose acetate while the grids rest on a wire mesh support at the surface of the acetone. This leaves the replicas lying on the grids. Commercially available adhesive-coated tapes, such as "Scotch Brand Tapes", are not suitable because they cannot be subsequently dissolved together with their adhesives.

Oxide remains over much of the area, and may be dissolved away after optical microscopic examination. If the oxide is sufficiently thin, it can be examined by electron microscopy. Thinning of the oxide may be possible, but has not been attempted.

## 10. APPENDICES

### APPENDIX I

#### The Geometry of Whiskers on a Wire

This appendix presents a simple treatment of the unrealized ideal case of radial whiskers of equal length uniformly distributed on a cylindrical wire. The geometry of the electron micrograph with the beam normal to the wire is like that of a plan projection along the beam.

Fig. 20 shows the wire in cross section.  $G$  = wire radius,  $g$  = whisker length,  $h$  = whisker height as measured by its image (excluding the magnification change resulting from removal from the specimen focal plane).

$\theta$  = absolute value of the angular position about the wire relative to the line at the wire horizon in the beam.

$\theta_0$  = value of  $\theta$  for whiskers whose ends project onto the wire horizon.

$F$  = distance from the horizon line on the wire to the tip of a whisker at  $\theta_0$  - half the upper limit on the specimen depth.

By Pythagoras' theorem, from Fig. 20, we have

$$F = g \cdot \frac{\sqrt{2G}}{R} + 1 \quad (1)$$

This equation is useful in estimating specimen depth. For example, if  $2G = 224 \mu$  and  $g = 1 \mu$ , we have  $F = 15 \mu$  and a specimen depth of less than  $30 \mu$  for 1  $\mu$  whiskers on a wire of approximate 0.009 in diameter.

From Fig. 20, one can see that

$$G + h = G \cos \theta + g \cos \theta \quad (2)$$

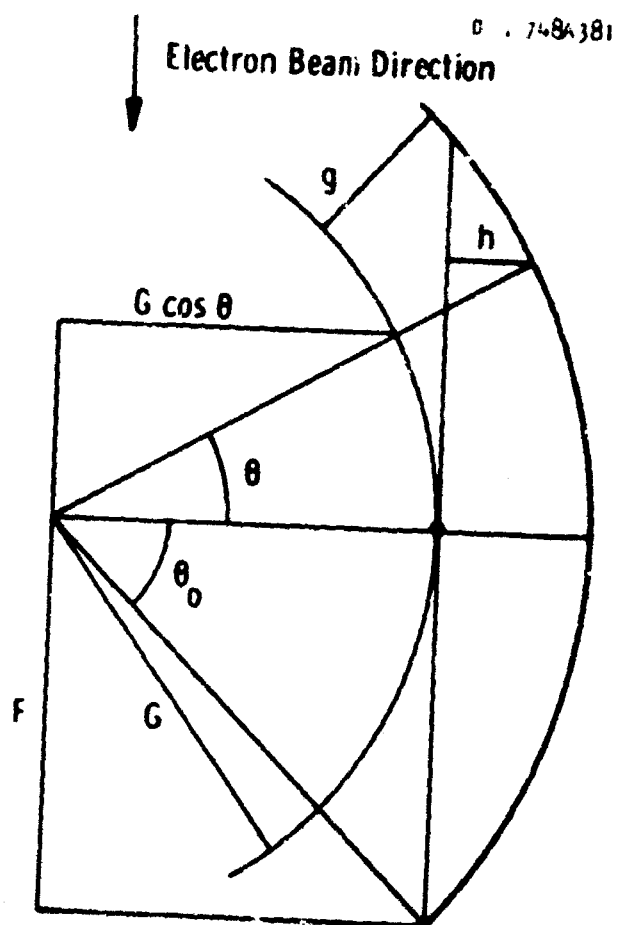


Fig 20-Whiskers on a wire



Rearranging gives a convenient equation for h,

$$h = g \left( \frac{G}{g} + 1 \right) \cos \theta - G \quad (3)$$

From this we can write an equation for d, the relative diminution in whisker length in the image,

$$d = 1 - \frac{h}{g} = \left( \frac{G}{g} + 1 \right) (1 - \cos \theta) , \quad (4)$$

where  $0 \leq d \leq 1$ .

It would be useful to know how the distribution of whiskers with respect to lengths measured on electron micrographs is related to the distribution of whiskers with respect to length. We make a first step here toward such an understanding by calculating the distribution to be found in the micrograph for this case of radial whiskers of equal length uniformly distributed on a cylindrical wire.

If the number of whiskers per unit area is D, then

$$\int_0^\theta D G d\theta = D G \theta \quad (5)$$

Since d is a function of  $\theta$ , we can rewrite (5) as follows:

$$D G \theta = D G \int_0^\theta d\theta = D G \int_0^d \left( \frac{d\theta}{dd} \right) \quad (6)$$

Thus the distribution can be shown by plotting  $\theta$  vs. d. For this purpose equation (4) is approximated using the series expansion of  $\cos \theta$  as follows:

$$d = 1 - \frac{h}{g} = \left( \frac{G}{g} + 1 \right) \frac{\theta^2}{2} ,$$

or

$$\theta = \frac{\sqrt{2d}}{\sqrt{\frac{G}{g} + 1}} \quad (7)$$

The upper limit on the number of whiskers to be counted on a micrograph is  $2 DG\theta_0$ , where by definition,  $\theta = \theta_0$  for  $d = 1$ . Thus  $\theta_0$  (in radians) is given by putting  $d = 1$  in (7).

The distribution to be found on the micrograph is given by

$$\frac{2 DG\theta}{2 DG\theta_0} = \frac{\theta}{\theta_0} = \sqrt{d} = \sqrt{1 - \frac{h}{g}}, \quad (8)$$

which follows from (7).

The ratio  $\theta/\theta_0$  is the fraction of whiskers whose image lengths are not less than  $h$ , or are not diminished by more than the fraction  $d$ . For  $d = 1/4$ , it follows from (8) that  $\theta/\theta_0 = 1/2$ ; and so we can say that half of the whiskers on the micrograph will show lengths within 25% of the maximum. Similarly, one third will be within one ninth of the maximum.

The distributions with respect to length on real micrographs of whiskers and other growths will be shifted toward shorter lengths because of the generally non-radial character. Surface irregularities could affect the distribution significantly in individual micrographs. Quantitative consideration of these effects has not been attempted.

## APPENDIX II

### $\alpha\text{-Fe}_2\text{O}_3$ Crystal Structure

Pauling and Hendricks<sup>36</sup> determined the crystal structure of  $\alpha\text{-Fe}_2\text{O}_3$  in 1925. The structure is trigonal, or rhombohedral, space group  $R\bar{3}c$ .<sup>37</sup>

In hexagonal coordinates, with the origin at the center ( $\bar{3}$ ), the iron atoms occupy the c positions:  $0,0,z$ ;  $0,0,\bar{z}$ ;  $0,0,1/2+z$ ;  $0,0,1/2-z$ . The oxygen atoms occupy the e positions:  $x,0,1/2$ ;  $0,x,1/4$ ;  $\bar{x},\bar{x},1/4$ ;  $\bar{x},0,3/4$ ;  $0,\bar{x},3/4$ ;  $x,x,3/4$ .

The crystal structure has been confirmed recently by Blake et al.<sup>38</sup> In this later work, the natural hematite used contained, with lesser impurities,  $1.0 \pm 0.2\%$  aluminum, or about  $2.8 \pm 0.6\%$  of the iron positions were filled by aluminum ions. Pauling and Hendricks give no analysis for their natural hematite crystal. Table 10 gives some literature values for the lattice parameters of  $\alpha\text{-Fe}_2\text{O}_3$ . The values in parentheses have been calculated for this data.

Willis and Rooksby<sup>39</sup> have measured the lattice constants of hematite as a function of temperature between  $20^\circ$  and  $950^\circ\text{C}$ . The axial ratio decreases rapidly between  $200^\circ$  and  $700^\circ\text{C}$  as shown in Table 10. The values at  $20^\circ$  and  $750^\circ\text{C}$ , respectively, are 2.7311 and 2.7223. The thermal expansion coefficients of c and a change sharply with temperature. They average about  $1.0 \times 10^{-5} \text{ }^\circ\text{C}^{-1}$  and  $1.4 \times 10^{-5} \text{ }^\circ\text{C}^{-1}$ , respectively. This anisotropic relative increase in a results from the decrease in antiferromagnetic interaction with increasing temperature, corresponding to decreasing order in the orientation of the spins and increasing paramagnetic susceptibility.

Willis and Rooksby<sup>39</sup> found for synthetic  $\alpha\text{-Fe}_2\text{O}_3$  prepared from precipitated  $\alpha\text{-FeOOH}$  and fired at a relatively low temperature a c/a value of 2.7305 at 20°C instead of 2.7311. This specimen was probably purer than the natural hematite crystals. Heating the synthetic oxide in air at 1300°C increased the c/a value to the reproducible room temperature value of 2.7311. A smaller value of c/a could result from a decreased antiferromagnetic interaction in the smaller  $\alpha\text{-Fe}_2\text{O}_3$  crystal from the low temperature firing.

Takada and Kawai<sup>40</sup> prepared  $\alpha\text{-Fe}_2\text{O}_3$  specimens by heating  $\alpha\text{-FeOOH}$ , goethite, to 250 and 900°C. They found the magnetic susceptibility to increase very significantly with decreasing particle size for particles of less than 320 Å diameter and, for such particles, to increase with decreasing temperature. This is a paramagnetic behavior called superparamagnetism by Neel.<sup>41</sup> Takada and Kawai found that "the antiferromagnetic transition of  $\alpha\text{-Fe}_2\text{O}_3$  at -19°C disappears when the diameter of the unit particles of the samples is smaller than about 320 Å."

The d-spacings and angles for  $\alpha\text{-Fe}_2\text{O}_3$  given in the present work are based on the dimensions given on ASTM Card 13-534.<sup>25</sup> The values of Willis and Rooksby may be better. The axial ratio 2.73009 compares with that for  $\alpha\text{-Al}_2\text{O}_3$ ,<sup>46</sup> 2.7298, so that the angles given in Appendix V for  $\alpha\text{-Fe}_2\text{O}_3$  approximate those for  $\alpha\text{-Al}_2\text{O}_3$ .

Drawings and descriptions of the structure have been given by Blake et al.,<sup>38</sup> Shirane et al.,<sup>42</sup> and especially by Kronberg.<sup>43</sup> The structure can be described as alternate layers of oxide and ferric ions, six layers of each per unit cell. The oxide ions are in approximate hexagonal close-packing and lie in planes parallel to the basal plane. The ferric ions fill two thirds of the octahedral holes and are at the corners of puckered hexagons about the remaining holes, which are at the center ( $\bar{3}$ ). These holes are in an approximate cubic close-packing arrangement--i.e., an ABCABC order, interleaving the 121212 order of the oxide ions to give 1A2B1C2A1B2C. There are two formula units,  $\text{Fe}_2\text{O}_3$  in the rhombohedral unit cell, six in the equivalent hexagonal unit cell.

**TABLE 10**  
Crystallographic Data for  $\alpha\text{-Fe}_2\text{O}_3$

Structural Hexagonal Dimensions			Rhombohedral Dimensions		Atom Parameters Hexagonal Coordinates			Reference
a	c	c/a	$\alpha$	a	X	Y	Z	
(5.029) $\text{\AA}$	(13.730) $\text{\AA}$	(2.7303)	55°17'	5.42 $\pm$ 0.0 $\text{\AA}$	0.292 $\pm$ 0.007	0.355 $\pm$ 0.001		36
5.038 $\pm$ 0.002	13.772 $\pm$ 0.012	2.733 $\pm$ 0.015 (2.7336 $\pm$ 0.0034)	(55°13.9')	(5.469)	0.3059 = 0.0001	0.3553 = 0.0001		42
5.0345	13.749	2.7311	55°15.8'	5.4271	--	--		38
5.0856	13.845	2.7223	55°24.3'	5.4698	--	--		39 20°C
5.0317	13.737	(2.73009)	(55°17.2')	5.4228				39 750°C
								25

### APPENDIX III

#### $\alpha$ -Fe<sub>2</sub>O<sub>3</sub> Unit Cells

Fig. 21 shows top and front views and dimensions for the unit cells useful for  $\alpha$ -Fe<sub>2</sub>O<sub>3</sub> and its isomorphs. The conventional structural and morphological hexagonal and rhombohedral unit cells are all four in common use. It is the rhombohedral angle  $\alpha$ , or the axial ratio, of the morphological unit cell which is important for morphological work, because it is this dimension which involves interfacial angles. The structural unit cells provide the lattice points necessary to predict the diffraction patterns. The face-centered rhombohedral unit cell indices are the same as those for the conventional morphological rhombohedral unit cell, but the centering is unnecessary for morphology. The rhombohedral F cell angle  $\alpha$  is nearly 90° because the rhombohedral P cell angle  $\alpha$  is nearly 60°. This follows from the fact that a 60° primitive rhombohedral cell is characteristic of the face-centered cubic lattice. It is this relationship to face-centered cubic which makes the use of the rhombohedral F cell convenient; this cell is used exclusively in indexing the selected area diffraction patterns presented in this report.

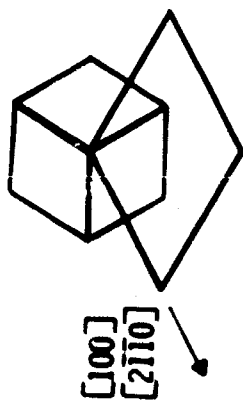
The rhombohedral F cell has the following advantages: Previous familiarity with cubic geometry provides ready understanding of this geometry as a distortion of cubic geometry. Directions are normal or nearly normal to lattice planes with the same indices. Directions in the basal plane (for which  $h + k + l = 0$ ) and  $[111]$  are normal to lattice planes with the same indices. Any other direction is at a smaller angle to  $[111]$  than in the cubic geometry, and the normal to

the lattice planes with the same indices (a row of reciprocal lattice points) is at a larger angle to  $[111]$  and in the plane of  $[111]$  and the direction. From this latter relationship, one can see that if  $[h_1 k_1 l_1] \perp [111]$  (i.e.,  $h_1 + k_1 + l_1 = 0$ ), for  $h_1 h_2 + k_1 k_2 + l_1 l_2 = 0$ , we have  $[h_1 k_1 l_1] \perp [h_2 k_2 l_2]$  and  $(h_1 k_1 l_1) \perp (h_2 k_2 l_2)$ .

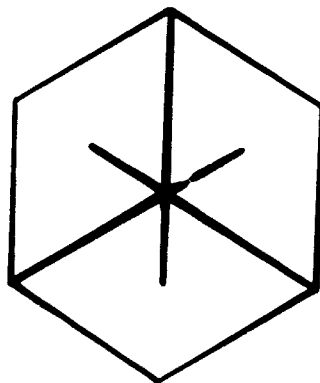
The directions are, by definition, for any lattice, parallel to rows of (real) lattice points, and are thus the intersections of lattice planes and are normal to the corresponding net of reciprocal lattice points. Thus, as a corollary to what has been said before, if not normal or parallel to the basal plane, a reciprocal net is at a smaller angle to the basal plane than in the cubic case, the lattice plane at a larger angle, and the intersection of the two is in the basal plane.

Fig. 21 -  $\alpha$ - $\text{Fe}_2\text{O}_3$  unit cells

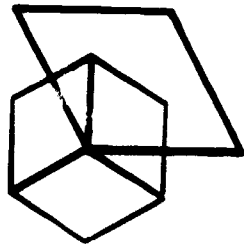
Orig. 747A56C



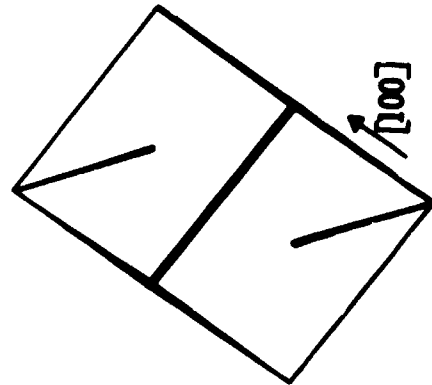
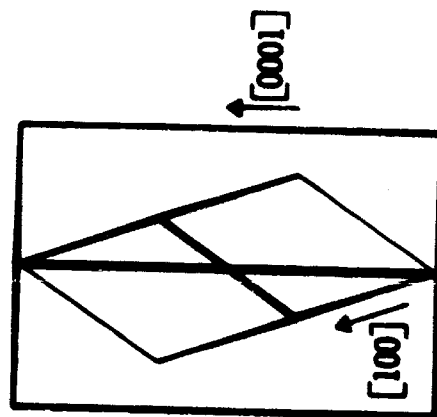
Conventional  
Structural  
 $a = 5.4228 \text{ \AA}$ ,  $\alpha = 55.273^\circ$   
 $a = 5.0317 \text{ \AA}$ ,  $c = 13.737 \text{ \AA}$



Rhombohedral F  
Structural  
 $a = 7.3976 \text{ \AA}$   
 $\alpha = 85.715^\circ$



Conventional  
Morphological  
 $a = 3.6988 \text{ \AA}$   
 $\alpha = 85.715^\circ$





#### APPENDIX IV

##### Transformation of Indices

We use the rhombohedral F (face-centered) indices to index the selected-area electron diffraction for the reasons given in Appendix III. It is essential to relate these indices to the more conventional indices. Table 3.4.2 of Volume II of the International Tables for X-Ray Crystallography<sup>44</sup> provides easy transformation from hexagonal to rhombohedral indices for lattice planes. This was used in preparing Table 11.

The transformation from rhombohedral F to morphological rhombohedral indices requires only division by the largest common factor. The rhombohedral P to hexagonal transformation provided in the table is independent of the rhombohedral angle and will do for both the morphological and structural unit cell.

Transformations to sets of planes equivalent in Laue group  $\bar{3}$  and to directions are provided for any set of planes or any direction by cyclic permutations in the same sense of all the sets of rhombohedral indices and of hki of the hexagonal indices hkil, and by multiplication of all sets by -1. Transformations between rhombohedral P sets hkl and hlk, equivalent in  $\bar{3}m$ , correspond to appropriate interchanges of indices in the other systems. The planes (LHK) and (ihkl) are at  $120^\circ$  about [111], or [0001], from (HKL) and (hkil), respectively (HKL are rhombohedral indices). The directions [LHK] and [ihkl] are at  $120^\circ$  to [HKL] and [hkil], respectively.

Since the use of three indices for the hexagonal system results in confusion and loss of convenience, four indices are used throughout this report. For completeness, and to facilitate comparison with three-index data in the literature, the transformations for directions are given as follows.<sup>45</sup>

$$[uvw] \rightarrow [UVW] : U = u-t, V = v-t, W = w$$

$$[UVW] \rightarrow [uvw]: 3u = 2U-V, 3v = 2V-U, t = -(U+V), w = W.$$

For planes, the third index is superfluous, as  $hkl \rightarrow hki$  requires only that  $i = -(h+k)$ . Note that  $[hki0]$  is perpendicular to  $(hki0)$ , whereas  $[hk0]$  is not perpendicular to  $(hk0)$  because  $i$  is not superfluous in  $[hki0]$ .

Table 11 is complete as far as it goes, including indices for all sets of planes non-equivalent in Laue group  $\bar{3}m$  in order of decreasing d-spacing in  $\alpha\text{-Fe}_2\text{O}_3$ . One can see in the rhombohedral F indices a relationship with face-centered cubic in that only the planes for  $h,k,l$  either all odd or all even are included (others are not indexed by the rhombohedral P unit cell), and non-equivalent sets of planes for which  $s = h^2 + k^2 + l^2$  is the same (for rhombohedral F indices) are listed separately when  $|h+k+l|$  varies. As in the face-centered cubic system,  $s$  takes the values, 3, 4, 8, 11, 12, 16, .... Thus the powder diffraction pattern of  $\alpha\text{-Fe}_2\text{O}_3$  is related to that of a face-centered cubic compound by a "splitting" of the lines resulting from the  $\alpha < 90^\circ$  for the rhombohedral F cell. Systematic absences for  $\alpha\text{-Fe}_2\text{O}_3$  are discussed in Appendix VI.

It should be noted that the hexagonal  $l$  value is the sum of each set of rhombohedral indices. Equivalent sets of planes have the same hexagonal  $l$  absolute value.

TABLE 11

## Transformation of Indices for Lattice Planes

Hexagonal Triple hkl	Rhombohedral P hkl	Rhombohedral F hkl	Hexagonal Triple hkl	Rhombohedral P hkl	Rhombohedral F hkl
0003	111	111	21 $\bar{3}$ 4	310	4 $\bar{2}$ 2
10 $\bar{1}$ 1	100	1 $\bar{1}$ 1	02 $\bar{2}$ 7	331	511
01 $\bar{1}$ 2	110	200	30 $\bar{3}$ 0	2 $\bar{1}$ $\bar{1}$	2 $\bar{4}$ 2
10 $\bar{1}$ 4	211	202	12 $\bar{3}$ 5	320	5 $\bar{1}$ 1
11 $\bar{2}$ 0	10 $\bar{1}$	2 $\bar{2}$ 0	03 $\bar{3}$ 3	22 $\bar{1}$	5 $\bar{1}$ $\bar{1}$
01 $\bar{1}$ 5	221	311	30 $\bar{3}$ 3	300	3 $\bar{3}$ 3
0006	222	222	20 $\bar{2}$ 8	422	404
11 $\bar{2}$ 3	210	3 $\bar{1}$ 1	10 $\bar{1}$ .10	433	424
02 $\bar{2}$ 1	11 $\bar{1}$	3 $\bar{1}$ $\bar{1}$	11 $\bar{2}$ 9	432	513
20 $\bar{2}$ 2	200	2 $\bar{2}$ 2	21 $\bar{3}$ 7	421	5 $\bar{1}$ 3
02 $\bar{2}$ 4	220	400	22 $\bar{4}$ 0	20 $\bar{2}$	4 $\bar{4}$ 0
10 $\bar{1}$ 7	322	313	03 $\bar{3}$ 6	330	600
20 $\bar{2}$ 5	311	3 $\bar{1}$ 3	30 $\bar{3}$ 6	411	4 $\bar{2}$ 4
11 $\bar{2}$ 6	321	402	22 $\bar{4}$ 3	31 $\bar{1}$	5 $\bar{3}$ 1
21 $\bar{3}$ 1	20 $\bar{1}$	3 $\bar{3}$ 1	13 $\bar{4}$ 1	21 $\bar{2}$	5 $\bar{3}$ $\bar{1}$
12 $\bar{3}$ 2	21 $\bar{1}$	4 $\bar{3}$ 0	31 $\bar{4}$ 2	30 $\bar{1}$	4 $\bar{4}$ 2
01 $\bar{1}$ 8	332	422	12 $\bar{3}$ 8	431	602
0009	333	333			

## APPENDIX V

### Interfacial and Other Angles in $\alpha\text{-Fe}_2\text{O}_3$

Table 12 lists angles for  $\alpha\text{-Fe}_2\text{O}_3$  which have been calculated to date. Formulae in section 3.9 of Vol. II of International Tables for X-Ray Crystallography<sup>44</sup> were used, together with the hexagonal dimensions  $a = 5.0317 \text{ \AA}$ ,  $c = 13.737 \text{ \AA}$ ,  $c/a = 2.73009$ . The angles in cubic geometry for the elements with indices (in the cubic system) the same as those given for the rhombohedral F cell are listed for comparison.

Note that the  $c/a$  value, 2.7298, for  $\alpha\text{-Al}_2\text{O}_3$ <sup>46</sup> indicates that the  $\alpha\text{-Fe}_2\text{O}_3$  angles differ only slightly from those for  $\alpha\text{-Al}_2\text{O}_3$ .

TABLE 12

 $\alpha\text{-Fe}_2\text{O}_3$  Angles

Hexagonal	Rhombohedral P	Rhombohedral F	$\alpha\text{-Fe}_2\text{O}_3$	Cubic
$[10\bar{1}1]$ , $[\bar{1}101]$	$[100]$ , $[010]$	$[101]$ , $[110]$	$55.287^\circ$	$60^\circ$
$(0003)$ , $(10\bar{1}1)$	$(111)$ , $(100)$	$(111)$ , $(1\bar{1}1)$	$72.400^\circ$	$70.529^\circ$
$(0003)$ , $(01\bar{1}2)$	$(111)$ , $(110)$	$(111)$ , $(200)$	$57.608^\circ$	$54.736^\circ$
$(10\bar{1}1)$ , $(\bar{1}101)$	$(100)$ , $(010)$	$(1\bar{1}1)$ , $(11\bar{1})$	$68.724^\circ$	$70.529^\circ$
$[02\bar{2}1]$ , $[\bar{2}021]$	$[11\bar{1}]$ , $[\bar{1}11]$	$[100]$ , $[010]$	$85.715^\circ$	$90^\circ$
$(0003)$ , $(\bar{1}104)$	$(111)$ , $(121)$	$(111)$ , $(220)$	$38.242^\circ$	$35.264^\circ$
$(01\bar{1}2)$ , $(\bar{1}012)$	$(110)$ , $(011)$	$(200)$ , $(020)$	$93.984^\circ$	$90^\circ$
$(\bar{1}01\bar{4})$ , $(\bar{1}012)$	$(\bar{2}\bar{1}\bar{1})$ , $(011)$	$(\bar{2}0\bar{2})$ , $(020)$	$84.150^\circ$	$90^\circ$
$(\bar{1}012)$ , $(\bar{1}104)$	$(011)$ , $(121)$	$(020)$ , $(220)$	$46.993^\circ$	$45^\circ$
$(0\bar{1}14)$ , $(\bar{1}014)$	$(112)$ , $(\bar{2}\bar{1}\bar{1})$	$(022)$ , $(\bar{2}0\bar{2})$	$64.831^\circ$	$60^\circ$
$(1\bar{1}04)$ , $(\bar{1}\bar{1}20)$	$(112)$ , $(\bar{1}01)$	$(022)$ , $(\bar{2}20)$	$57.584^\circ$	$60^\circ$
$(11\bar{2}0)$ , $(21\bar{3}4)$	$(10\bar{1})$ , $(310)$	$(2\bar{2}0)$ , $(4\bar{2}2)$	$27.697^\circ$	$30^\circ$
$(2\bar{1}\bar{1}0)$ , $(21\bar{3}4)$	$(1\bar{1}0)$ , $(310)$	$(0\bar{2}2)$ , $(4\bar{2}2)$	$53.823^\circ$	$54.736^\circ$
$(10\bar{1}4)$ , $(\bar{1}101)$	$(211)$ , $(010)$	$(202)$ , $(11\bar{1})$	$93.298^\circ$	$90^\circ$
$(0001)$ , $(10\bar{1}1)$	$(111)$ , $(100)$	$(111)$ , $(1\bar{1}1)$	$72.400^\circ$	$70.529^\circ$
$(\bar{1}101)$ , $[\bar{4}401]$	$(010)$ , $[\bar{1}3\bar{1}]$	$(11\bar{1})$ , $[11\bar{1}]$	$86.093^\circ$	$90^\circ$
$[0001]$ , $[\bar{4}401]$	$[111]$ , $[\bar{1}3\bar{1}]$	$[111]$ , $[11\bar{1}]$	$68.493^\circ$	$70.529^\circ$

## APPENDIX VI

### Systematic Absences in the Diffraction from $\alpha\text{-Fe}_2\text{O}_3$

Systematic absences in the  $\alpha\text{-Fe}_2\text{O}_3$  diffraction result only from the c-glide plane in the case of the primitive unit cell. In the case of the non-primitive unit cells, those lattice planes which are not indexed by the primitive unit cell do not diffract. The rules for these absences are given in International Tables for X-Ray Crystallography, Vol. I.<sup>37</sup> Only those planes diffract for which the following conditions are satisfied:

	Non-Primitive Condition	c-Glide Condition
Rhombohedral P	No restrictions	hhl: $l = 2n$
Hexagonal (obverse orientation)	hkil: $-h+k+l = 3n$ , and thus, hh $\bar{2}$ hl: ( $l = 3n$ ) hh0l: ( $h+l = 3n$ )	hh0l: $l = 2n$
Rhombohedral F	$h+k, k+l, (l+h) = 2n$ , or h,k,l all odd or all even	hhl: $l = 2n$

The rhombohedral F reciprocal lattice is thus body-centered with the body centers (i.e., h,k,l. all odd) absent for nets hhl. The iron atom positions are such that they contribute to the diffraction with hexagonal indices  $hkil_H$  only for  $l_H = 2n$ , thus not to the diffraction for rhombohedral F with h,k,l. all odd (because  $h+k+l = l_H$ ).

In the x-ray powder diffraction pattern, the one intense diffraction ring ( $I/I_0 = 30$ ) from the oxygen atoms only is indexed  $11\bar{2}3$  (Appendix VIII). The same set of planes would be indexed  $10\bar{1}1$  in the (idealized) hexagonal close-packed oxygen lattice of  $\alpha\text{-Fe}_2\text{O}_3$ , the set of planes giving the highest x-ray diffraction intensity in the hexagonal close-packed elements.

## APPENDIX VII

### List of Interplanar Spacings $d$ , and of $d^{-1}$ and $d^{-2}$ for $\alpha\text{-Fe}_2\text{O}_3$

The accompanying table, Table 13, lists values calculated using  $a = 5.0317 \text{ \AA}$ ,  $c = 13.737 \text{ \AA}$ ,  $c/a = 2.73009113$  (cf. Appendix II). To calculate  $d^{-2}$ ,

$$c^*^2 = c^{-2} = 52.99272 \times 10^{-4} \quad \text{and} \quad a^*^2 = 4/(3a^2) = 526.63444 \times 10^{-4}$$

were substituted into the equation,

$$d_{hkl}^{-2} = (h^2 + hk + l^2) a^*^2 + l^2 c^*^2 .$$

Table 13 lists all values for which there are primitive rhombohedral indices (i.e., excluding hexagonal  $-h+k+l = 3n$ ) in order of decreasing  $d$ -spacing, to an arbitrary limit.

Table 14 lists all values for  $hki0$  and  $0001$  to arbitrary limits. The values of  $d^{-1}$  and  $d^{-2}$ , in both tables, are especially useful in constructing reciprocal lattice sections and in calculating trigonometric functions of interfacial angles.



TABLE 13

 $\alpha$ -Fe<sub>2</sub>O<sub>3</sub> Interplanar Spacings

Rhomb. F hkl	Structural Hexagonal hkil	$10^4 d^{-2}$	$10^4 d^{-1}$	$d$
111	0003	476.934	2183.883	4.579 Å
1 $\bar{1}$ 1	10 $\bar{1}$ 1	579.627	2407.545	4.1536
200	01 $\bar{1}$ 2	738.605	2717.729	3.6795
202	10 $\bar{1}$ 4	1374.518	3707.449	2.6973
2 $\bar{2}$ 0	11 $\bar{2}$ 0	1579.903	3974.800	2.5158
311	01 $\bar{1}$ 5	1851.452	4302.851	2.3240
222	0006	1907.738	4367.766	2.2895
3 $\bar{1}$ 1	11 $\bar{2}$ 3	2056.838	4535.237	2.2050
3 $\bar{1}$ $\bar{1}$	02 $\bar{2}$ 1	2159.530	4647.075	2.1519
2 $\bar{2}$ 2	20 $\bar{2}$ 2	2318.509	4815.089	2.0768
400	02 $\bar{2}$ 4	2954.421	5435.459	1.8398
313	10 $\bar{1}$ 7	3123.278	5588.629	1.7893
3 $\bar{1}$ 3	20 $\bar{2}$ 5	3431.356	5857.778	1.7071
402	11 $\bar{2}$ 6	3487.641	5905.625	1.6933
3 $\bar{3}$ 1	21 $\bar{3}$ 1	3739.434	6115.091	1.6353
4 $\bar{2}$ 0	12 $\bar{3}$ 2	3898.412	6243.726	1.6016
422	01 $\bar{1}$ 8	3918.169	6259.528	1.5976
333	0009	4292.410	6551.649	1.5263
4 $\bar{2}$ 2	21 $\bar{3}$ 4	4534.325	6733.739	1.4851

(Continued)

TABLE 13 (Continued)

Rhomb. F hkl	Structural Hexagonal hkil	$10^4 d^{-2}$	$10^4 d^{-1}$	d
511	02 $\bar{2}$ 7	4703.181	6857.974	1.4582 Å
2 $\bar{4}$ 2	30 $\bar{3}$ 0	4739.710	6884.555	1.4525
5 $\bar{1}$ 1	12 $\bar{3}$ 5	5011.259	7079.025	1.4126
5 $\bar{1}\bar{1}$	03 $\bar{3}$ 0	5216.644	7222.634	1.3845
3 $\bar{3}$ 3	30 $\bar{3}$ 3			
404	20 $\bar{2}$ 8	5498.072	7414.898	1.3486
424	10 $\bar{1}$ .10	5825.906	7632.762	1.3101
513	11 $\bar{2}$ 9	5872.314	7663.102	1.3050
5 $\bar{1}$ 3	21 $\bar{3}$ 7	6283.084	7926.591	1.2616
4 $\bar{4}$ 0	22 $\bar{4}$ 0	6319.613	7949.600	1.2580
600	03 $\bar{3}$ 6	6647.448	8153.188	1.2265
4 $\bar{2}$ 4	30 $\bar{3}$ 6			
5 $\bar{3}$ 1	22 $\bar{4}$ 3	6796.548	8244.118	1.2130
5 $\bar{3}\bar{1}$	13 $\bar{4}$ 1	6899.240	8306.167	1.2039
4 $\bar{4}$ 2	31 $\bar{4}$ 2	7058.219	8401.320	1.1903
602	12 $\bar{3}$ 8	7077.975	8413.070	1.1886

TABLE 14

 $\alpha\text{-Fe}_2\text{O}_3$  Useful Hexagonal Dimensions

$\frac{h^2 + hk + k^2}{+k^2}$	Hexagonal hkil	$10^4 d^{-2}$	$10^4 d^{-1}$	d
1	10 $\bar{1}$ 0	526.6344	2294.852	4.3576 Å
3	11 $\bar{2}$ 0	1579.903	3974.800	2.5158
4	20 $\bar{2}$ 0	2106.538	4589.703	2.1788
7	21 $\bar{3}$ 0	3686.441	6071.607	1.6470
9	30 $\bar{3}$ 0	4739.710	6884.555	1.4525
12	22 $\bar{4}$ 0	6319.613	7949.600	1.2579
13	31 $\bar{4}$ 0	6846.247	8274.205	1.2086
	0001	52.99272	727.970	13.7370
	0002	211.971	1455.922	6.8685
	0003	476.934	2183.883	4.5790
	0004	847.884	2911.844	3.4342
	0005	1324.818	3639.805	2.7474
	0006	1907.738	4367.766	2.2895
	0007	2596.643	5095.727	1.9624
	0008	3391.534	5823.688	1.7171
	0009	4292.410	6551.649	1.5263
	000.10	5299.272	7279.610	1.3737
	000.11	6412.119	8007.571	1.2488
	000.12	7630.952	8735.532	1.1447

## APPENDIX VIII

### Intensities and d-Spacings for Selected Iron Oxides

Table 15 lists indices and calculated d-spacings for useful unit cell dimensions for  $\text{FeO}$ ,  $\text{Fe}_3\text{O}_4$ ,  $\gamma\text{-Fe}_2\text{O}_3$ , and  $\alpha\text{-Fe}_2\text{O}_3$ , together with x-ray intensities from ASTM cards. The  $\alpha\text{-Fe}_2\text{O}_3$  d-spacings are listed near the  $\gamma\text{-Fe}_2\text{O}_3$  d-spacings of comparable value. The order listed-- $\text{FeO}$ ,  $\text{Fe}_3\text{O}_4$ ,  $\gamma\text{-Fe}_2\text{O}_3$ --is the order of decreasing dimension for the cubic close-packed oxygen lattice. Sets of planes with the same indices in this lattice are listed in a row.

The many coincidences between the  $\alpha\text{-Fe}_2\text{O}_3$  and  $\gamma\text{-Fe}_2\text{O}_3$  d-spacings do not in general result from similar orientations of these planes in the oxygen lattices. The idealized close-packed oxygen row in  $\alpha\text{-Fe}_2\text{O}_3$  has the interatomic spacing,  $2 d_{30\bar{3}0} = 2.9050 \text{ \AA}$ , less by 1.46% than that for the O-O distance in  $\gamma\text{-Fe}_2\text{O}_3$ ,  $d_{2\bar{2}0} = 2.9479 \text{ \AA}$ . It is of interest to note that the O-O distances in the basal plane of  $\alpha\text{-Fe}_2\text{O}_3$  given by Blake *et al.*,<sup>38</sup> corrected to the hexagonal  $a$  value in this report, are  $2.658 \text{ \AA}$  and  $3.022 \text{ \AA}$ , averaging  $2.840 \text{ \AA}$ .

The spacings of the planes  $\{440\}$  and  $\{30\bar{3}0\}$  of  $\gamma\text{-Fe}_2\text{O}_3$  and  $\alpha\text{-Fe}_2\text{O}_3$ , respectively, which are similarly related to the oxygen lattices, would be exactly equal if the cubic dimension  $a$  of  $\gamma\text{-Fe}_2\text{O}_3$  were exactly the hexagonal  $a$  of  $\alpha\text{-Fe}_2\text{O}_3$  multiplied by  $(2/3) \sqrt{6}$ .

The oxygen layers lie on  $\{222\}$  planes, with interplanar spacings of  $2.4070 \text{ \AA}$  in  $\gamma\text{-Fe}_2\text{O}_3$  and  $2.2895 \text{ \AA}$  in  $\alpha\text{-Fe}_2\text{O}_3$ , respectively. These spacings are smaller by 4.88% in  $\alpha\text{-Fe}_2\text{O}_3$ .

The many coincidences among d-spacings result in greater requirements on the quality of powder diffraction patterns for the recognition of the presence of  $\alpha\text{-Fe}_2\text{O}_3$  with  $\gamma\text{-Fe}_2\text{O}_3$ , or of the presence of  $\gamma\text{-Fe}_2\text{O}_3$  with a mixture of  $\alpha\text{-Fe}_2\text{O}_3$  and  $\text{Fe}_3\text{O}_4$ . The presence of  $\text{Fe}_3\text{O}_4$  in  $\gamma\text{-Fe}_2\text{O}_3$  may easily remain unrecognized.

TABLE 15

Diffraction Data for  $\text{FeO}$ ,  $\text{Fe}_3\text{O}_4$ ,  $\gamma\text{-Fe}_2\text{O}_3$ , and  $\alpha\text{-Fe}_2\text{O}_3$ 

hkl	$1/1_0^\circ$	$d_{hkl}^\circ$ $a=4.308\text{\AA}$	Both hkl	$\text{Fe}_3\text{O}_4$ and $\gamma\text{-Fe}_2\text{O}_3$		$\gamma\text{-Fe}_2\text{O}_3$		$\alpha\text{-Fe}_2\text{O}_3$		Indices	
				$1/1_0^\circ$	$d_{hkl}^\circ$ $a=4.394\text{\AA}$	$1/1_0^\circ$	$d_{hkl}^\circ$ $a=8.338\text{\AA}$	$1/1_0^\circ$	$d_{hkl}^\circ$ $a=5.0317\text{\AA}$ $c=13.737\text{\AA}$	Hexagonal hkl	Rhomb. hkl
100			-				8.3380 $\text{\AA}$				
-			-	10	7.91 $^\circ$						
-			-	20	6.934 $^\circ$						
-			-	10	6.328 $^\circ$						
110				40	5.8959						
-			-	10	5.326 $^\circ$						
111				40	4.8139					0003	111
200			-	-	4.1690 $^\circ$					1011	111
110				60	3.7289			25	3.6795	0112	110
211				60	3.4040						
-			-	30	3.198 $^\circ$						
220			70	2.9677							
300/221				30	2.7793						
-			-	10	2.708 $^\circ$			100	2.6973	1014	202

(Continued)

**TABLE 15 (Continued)**

FeO		Fe <sub>3</sub> O <sub>4</sub> and γ-Fe <sub>2</sub> O <sub>3</sub>				γ-Fe <sub>2</sub> O <sub>3</sub>		α-Fe <sub>2</sub> O <sub>3</sub>		Indices		
hkl	1/I <sub>o</sub> <sup>a</sup>	d <sub>hkl</sub> <sup>a</sup>	Both	Fe <sub>3</sub> O <sub>4</sub> 1/I <sub>o</sub> <sup>a</sup>	d <sub>hkl</sub> <sup>a</sup>	1/I <sub>o</sub> <sup>†</sup>	d <sub>hkl</sub> <sup>a</sup>	1/I <sub>o</sub> <sup>†</sup>	d <sub>hkl</sub> <sup>a</sup>	Hexagonal hkl	Rhomboh. P hkl	Rhomboh. F hkl
		a=4.101 Å	a=8.194 Å		a=8.338 Å		a=5.0317 Å		c=13.737 Å			
		d <sub>hkl</sub> <sup>a</sup>										
111	80	2.4477 Å	2.4711 Å	100	2.5140	50	2.5158 Å	1120	101	220		
				20	2.4070	-	2.3240 <sup>a</sup>	0115	221	311		
				20	2.3125	2	2.2895	0006	222	222		
				10	2.2284	30	2.2050	1123	210	311		
				10	2.167 <sup>+</sup>	-	2.1519 <sup>a</sup>	0221	111	311		
200	100	2.1544	2.1400	70	2.0985	2	2.0768	2022	200	222		
			410/322				2.0222					
			411/330				1.9635					
			311	-	1.9257	-	1.9129					
			420	-	1.8770 <sup>A</sup>	-	1.8644					
			421	80	1.8195	40	1.8398	0224	220	400		
			312	-	1.7777	-	1.7893 <sup>a</sup>	1017	322	313		
						-	1.7071 <sup>A</sup>	2025	311	313		
			422	60	1.7134	60	1.6933	1126	321	402		
			500/430	10	1.6676							

(Continued)

**TABLE 15 (Cont Inued)**

$\gamma\text{-Fe}_2\text{O}_3$			$\alpha\text{-Fe}_2\text{O}_3$			$\gamma\text{-Fe}_2\text{O}_3$			$\alpha\text{-Fe}_2\text{O}_3$		
$hkl$	$1/1_0$	$d_{hkl}$ $a=5.0317\text{\AA}$	$hkl$	$1/1_0$	$d_{hkl}$ $a=4.394\text{\AA}$	$hkl$	$1/1_0$	$d_{hkl}$ $a=5.0317\text{\AA}$	$hkl$	$1/1_0$	$d_{hkl}$ $a=5.0317\text{\AA}$
510/431	10	1.6352 $\text{\AA}$	2131	4	1.6353 $\text{\AA}$	201	331	201	331		
511/333	90	1.6046	1232	-	1.6016	211	420	211	420		
520/432	20	1.5483	0118	16	1.5976	312	422	312	422		
521	20	1.5223	0009	-	1.5263 <sup>a</sup>	333	333	333	333		
540	90	1.4740	2134	35	1.4851	310	422	310	422		
522/441	-	1.4515	0227	-	1.4582 <sup>a</sup>	331	511	331	511		
530/433	-	1.4300	3030	35	1.4525	211	242	211	242		
531	-	1.4186	1235		1.4126	320	511	320	511		
600/442	-	1.3990 <sup>A</sup>	0333/3033	-	1.3845 <sup>B</sup>	221/300	511/333	221/300	511/333		
610	-	1.3708									
611/332	-	1.3526	2028		1.3486	422	404	422	404		
620	30	1.3184	101.10	20	1.3101	433	424	433	424		
621/540/443	-	1.3022	1129	-	1.3050	432	513	432	513		
541	-	1.2866									
533	30	1.2801	1137	-	1.2616	421	513	421	513		

(Continued)

**TABLE 15 (Continued)**

[illegible]

• ASTM Card A-0413

ASTM Card 11-614

EX-11 (REV) KJ5V

216-11 P&W MJSV 3



## APPENDIX IX

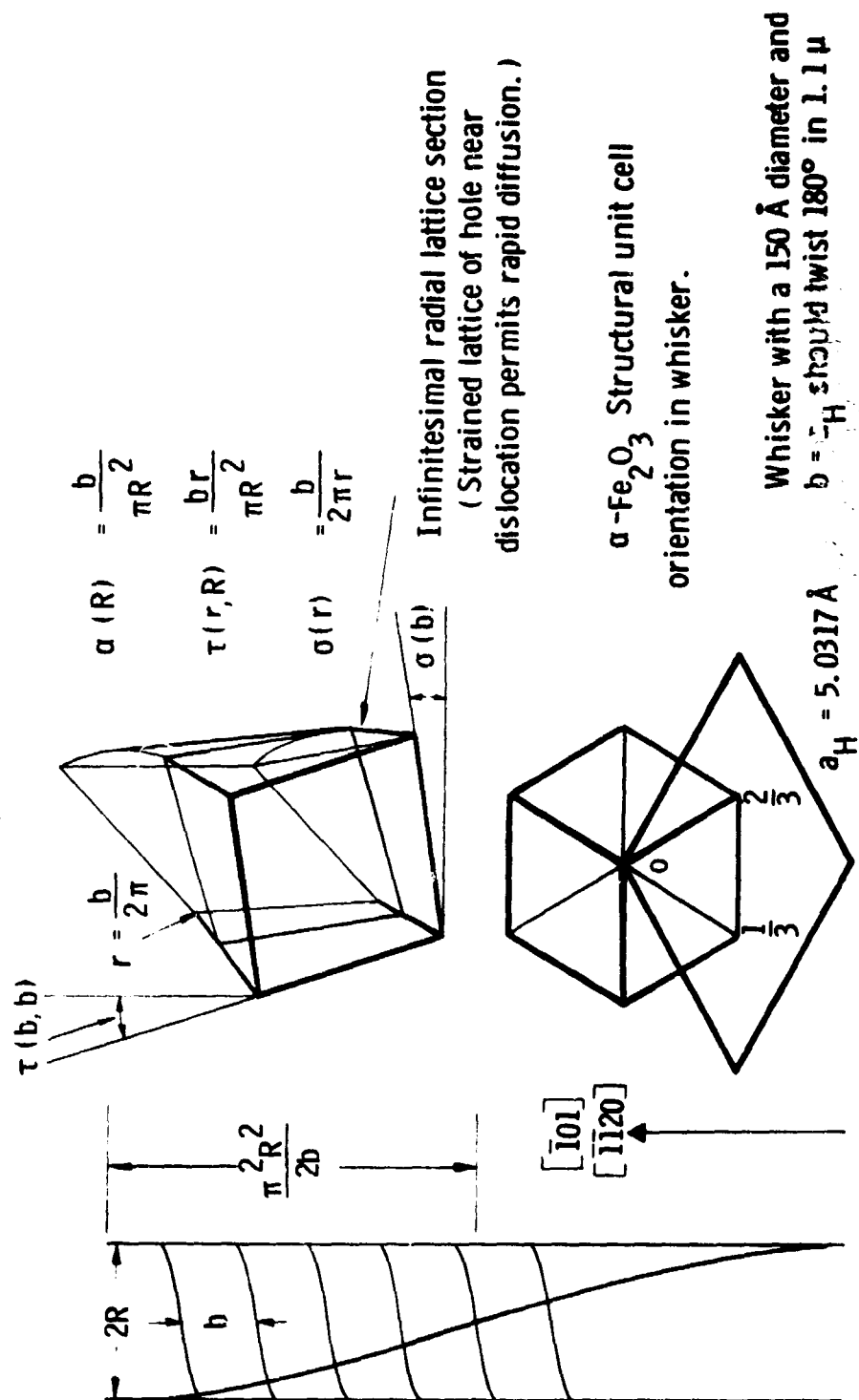
### Whisker Geometry--Screw Dislocation in a Rod

Figure 22 shows the features to be expected in a whisker with an axial screw dislocation. The case shown in Fig. 22 is that of a central screw dislocation in a rod with circular cross section.

The angle  $\sigma(r)$  results from the spiral climb of the lattice plane about the screw dislocation. The exact expression,  $\tan \sigma(r) = b/2\pi r$ , where  $r$  is the radius, results directly from this spiralling and is independent of the external shape of the crystal. It is this shear in the neighborhood of the dislocation which cannot correspond to some elastic deformation of the real structure. The structure of the real crystal in some region about the screw dislocation is undefined and remains to be described.

The angle  $\tau(r, R)$ , where  $R$  is the radius of the surface, is related to the axial twist,  $\alpha(R)$  by the equation,  $\tan \tau = r\alpha$ . Mann<sup>48</sup> and Eshelby<sup>49,18</sup> have derived theoretical equations for axial twist. These will be considered here. The case of a screw dislocation in the basal plane for rhombohedral symmetry was not considered.

Because the  $\alpha\text{-Fe}_2\text{O}_3$  structure does not suggest large anisotropy (cf. Appendix X) we assume that the axial twist for  $\alpha\text{-Fe}_2\text{O}_3$  will not be greatly different from that for an isotropic material of the same cross section. One difficulty occurs in applying the theoretical equations in that even if the correct equation were available it is unlikely that the cross section shape and area and the position of the dislocation in the whisker could be measured for whiskers  $150 \text{ \AA}$  in diameter.



For an isotropic material, Eshelby<sup>18</sup> gives the equation

$$\text{twist } \alpha = \frac{K \cdot b}{\Lambda}.$$

Here  $b$  is the length of the Burgers vector,  $A$  is the cross section area, and  $K$  is about 1.  $K$  decreases with the removal of the dislocation from the center.  $K$  depends also on the shape of the cross section. For a central dislocation,  $K = 1$  for any elliptical cross section, and decreases from 1.048 for a square to 0.75 for a rectangle with infinite ratio of edge lengths. Since Eshelby<sup>49,18</sup> has shown that the screw dislocation is at an energy minimum (in metastable equilibrium) at the center of the cross section and since a nearly elliptical cross section is likely, the approximation  $K = 1$  would appear justified. The value of  $K$  is slightly decreased when the screw dislocation is only a small distance from the center.

Eshelby<sup>50</sup> gives the equation  $\alpha = b/(A_0 + A_1)$  which he states is exact for the central dislocation in an isotropically elastic material. Here  $A_0$  and  $A_1$  are concentric elliptic areas enclosed by the inner and outer boundaries. This equation applied for the range  $0 \leq A_0/A_1 \leq 1$ .

According to the treatment by Frank<sup>51</sup>, also discussed by Cottrell<sup>20</sup>, an open core would not be stable relative to reasonable strained cores except for Burgers vectors considerably larger than  $5 \text{ \AA}$ . We can use Eshelby's equation as a lower limit on the axial twist by taking  $A_0$  to be an effective central area with zero rigidity.

Weertman and Weertman<sup>21</sup> assume an approximate stress level of  $\mu/30$  for a core of radius  $5b$ . Here  $\mu$  is the shear modulus. Thus, they would consider the discontinuous nature of the crystal to cause a decreased rigidity for strains greater than  $\frac{1}{10\pi}$ . This corresponds to the shear strain at radius  $5b$  with no twist. Frank considers strains  $> 0.1$ , or  $r < 5b/\pi$ , to limit Hooke's law. Thus, the radius of an effective hole for the calculation of the axial twist might be about  $10 \text{ \AA}$ . This hole reduces the axial twist by no more than a few percent.

From Figure 22 we see that  $\tau(R,R) = 2 \sigma R$ . The strain at the surface is large and is roughly normal to the strain near the center. The strain is zero where  $\sigma = \tau$  at  $r = R/\sqrt{2}$ . Except where  $\tau \ll \sigma$  at small  $r/R$ , the axial twist in a thin rod results in a strain pattern within the radius of the thin rod much different from that in a large crystal. This difference is reflected in the strain energy which is calculated in Appendix X.

## APPENDIX X

### Strain Energy of a Whisker

The strain energy expression given by Friedel<sup>19</sup> is derived here using the terminology of Figure 22 and Appendix IX.

The shears  $\tan \tau = br/\pi (R^2 + r_o^2)$  and  $\tan \sigma = b/2\pi r$  oppose one another so that the shear strain is given by

$$\tan (\tau - \sigma) = \frac{\tan \tau - \tan \sigma}{1 + \tan \tau \tan \sigma} = \frac{\frac{br}{R^2 + r_o^2} - \frac{b}{2\pi r}}{1 + \frac{1}{2} \left(\frac{b}{\pi R}\right)^2} = \frac{b}{\pi} \left( \frac{r}{R^2} - \frac{1}{2r} \right),$$

where we have neglected the effect on the axial twist of small  $r_o$ , the effective hole radius. The energy per unit length of screw dislocation is then, where  $\mu$  is the shear modulus,

$$\begin{aligned} W &= \frac{\mu}{2} \int_{r_o}^R \tan^2 (\tau - \sigma) 2\pi r dr \approx \\ &= \frac{\mu b^2}{4\pi} \left[ \ln \frac{R}{r_o} - 1 + 2 \left( \frac{r_o}{R} \right)^2 - \left( \frac{r_o}{R} \right)^4 \right] \approx \frac{\mu b^2}{4\pi} \left( \ln \frac{R}{r_o} - 1 \right), \end{aligned}$$

as given by Friedel. The axial twist introduces the term, -1, in the parentheses.

Taking into account the volume of a cylindrical whisker of  $\alpha\text{-Fe}_2\text{O}_3$ , with  $b = 5.0317 \text{ \AA}$ , the strain energy contribution to the molar free energy is given by

$$F(\text{strain}) = 1.066 \times 10^{-25} \frac{\mu}{R^2} \left( \log_{10} \frac{R}{r_o} - 0.4343 \right) \frac{\text{kcal}}{\text{mole}}.$$

For  $R = 100 \text{ \AA}$ ,  $r_0 = 5 \text{ \AA}$ ,  $\mu = 10^{12} \text{ dynes/cm}^2$ , we have  $F$  (strain)  $\approx 0.09 \text{ kcal/mole}$ . One can show that for a rod of these dimensions, about 95% of the strain energy is contained in the half of the volume of the crystal within the radius  $R/\sqrt{2}$ .

For the  $\alpha\text{-Fe}_2\text{O}_3$  whiskers, the stiffness constants involved most prominently in the strain are  $c_{55}$  and  $c_{66}$ . Values derived from the stiffness constants for  $\alpha\text{-Fe}_2\text{O}_3$  listed by Huntington<sup>52</sup> are:

$$c_{55} = 8.5 \times 10^{11} \text{ dynes cm}^2 \quad \text{and}$$

$$c_{66} = 9.35 \times 10^{11} \text{ dynes/cm}^2.$$

Taking  $[2\bar{1}\bar{1}0]$  to be the whisker axis,  $c_{55}$  and  $c_{66}$  are effectively values of  $\mu$  along  $[01\bar{1}0]$  and  $[0001]$ , respectively, both normal to  $[2\bar{1}\bar{1}0]$ . Thus  $\mu \sim 10^{12} \text{ dynes/cm}^2$ . Furthermore, since  $c_{55} \sim c_{66}$ ,  $\alpha\text{-Fe}_2\text{O}_3$  is only slightly anisotropic for the shears  $\sigma$  and  $\tau$ .

Huntington also lists  $c_{11} = c_{22} = 24.2 \times 10^{+11} \text{ dynes/cm}^2$ ,  $c_{33} = 22.8 \times 10^{+11} \text{ dynes/cm}^2$ ,  $s_{11} = s_{22} = 0.442 \times 10^{-12} \text{ cm}^2/\text{dyne}$ , and  $s_{33} = 0.444 \times 10^{-12} \text{ cm}^2/\text{dyne}$ . The near equality of these constants indicates only slight anisotropy in tension.

The linear compressibility,  $\beta$ , is defined by Nye<sup>53</sup> to be "the relative decrease in length of a line when the crystal is subjected to unit hydrostatic pressure." Substituting from Huntington's list into Nye's formula, we have

$$\beta = [0.317 + 0.081 \mathbf{l}_3^2] \times 10^{-3}/\text{kbar},$$

where  $\mathbf{l}$  is a unit vector along the line. Thus hydrostatic pressure results in about 26% more compression along  $[0001]$  than in the basal plane.

## APPENDIX XI

### Diffraction from a Rod with an Axial Screw Dislocation

The results of Wilson's treatment<sup>15,16,17</sup> of the diffraction from a cylindrical crystal with a screw dislocation but without axial twist are indicated here.

In the terminology of Appendix IX,  $\tau$  describes the distortion by the twist and  $\sigma$  describes the distortion by the screw dislocation. With a central screw dislocation in a cylindrical rod, for  $r = \frac{R}{\sqrt{2}}$ , we have  $\tau > \sigma$ . That is,  $\tau > \sigma$  for half the volume of the crystal. At the surface ( $r = R$ ) we have  $\tau = 2 \sigma$ . Where the beam does not penetrate and the diffraction is from crystal regions near the surface, the effects are primarily dependent on the distortion  $\tau$  resulting from the axial twist. However, this is not the case of greatest interest here.

As indicated in Appendix IX, the strain energy is much greater where  $\sigma > \tau$ . The strain energy is proportional to the integral of the strain over the volume; the diffraction amplitude also involves a sum over volume elements. On this basis the twist would be expected to have little effect on the diffraction. However, the twist results in a tilt of the lattice at  $r = R/\sqrt{2}$  without strain, and the tilt could affect the diffraction.

In this connection, Wilson's theory does not take into account the distortion or tilt of individual cells, but only their position. This is reflected in the predicted distribution of diffraction amplitude in planes normal to the rod axis. This feature would likely remain if the axial twist were taken into account in giving the cell positions. The twist is so small that no significant effect is to be expected.

However, introduction of distortion and tilt as well as the axial twist effect on the cell positions could provide a very different theoretical description of the diffraction.

In addition to the effects of the strain, refraction can affect the diffraction significantly.<sup>54,55</sup> That these effects alone would be sufficient to predict the anomalous diffraction by  $\alpha\text{-Fe}_2\text{O}_3$  whiskers seems unlikely, but the possibility cannot be eliminated without more complete theory.

Some idea of the nature of the results of Wilson's theory can be given here by indicating the interpretation by Frank: The amplitudes in reciprocal space are greatest in concentric rings about the index points. The first and most intense rings are approximately the intersections with the planes of the reciprocal nets normal to the rod, of cones with the same semi-angle,  $\frac{3b}{4\pi R}$ . This is the value of  $\sigma$  for  $r = 2R/3$ , so that the generators of the cones are normal at  $r = 2R/3$  to the lattice planes which would be normal to the axis of the undislocated rod. In the plane through the origin, the generators pass through the index points, and the amplitude distribution is the same as for an undislocated thin cylinder, with a maximum at the index point. For the other planes, the amplitude is zero at the index points.

A theory taking into account the cell distortion as well as position might spread the amplitude distribution of Wilson's theory out into regions of reciprocal space adjacent to the planes. The elongated diffraction spots, or streaks, are narrow, indicating no extreme deviation of this type from the diffraction character predicted by Wilson's theory.



## APPENDIX XII

### Driving Forces for Iron Diffusion in $\alpha$ -Fe<sub>2</sub>O<sub>3</sub> Growth

In order that the  $\alpha$ -Fe<sub>2</sub>O<sub>3</sub> whiskers and platelets grow at their tips, iron must be transported to the tips from the base. The oxidation of Fe<sub>3</sub>O<sub>4</sub> to Fe<sub>2</sub>O<sub>3</sub> can provide the driving force. A further force may result from the pressure on the Fe<sub>3</sub>O<sub>4</sub> developed in the oxidation, which is unknown. The surface free energy of the finest whiskers may introduce a further uncertainty in the driving force.

This appendix provides some simple considerations sufficient for rough approximations. Accurate calculations for local gradients in the driving forces for diffusion would be difficult for such a complex system and are impossible with our present lack of knowledge of the details of the whisker and platelet growth.

#### A. Surface Free Energy

The surface free energy is estimated by the relation given by Cottrell,<sup>10</sup>  $\gamma/\mu = 0.25 \times 10^{-8}$  cm, where  $\mu$  is the shear modulus, about  $1 \times 10^{12}$  dyne cm<sup>-2</sup> (cf. Appendix X). Thus,  $\gamma = 2.5 \times 10^3$  dyne cm<sup>-1</sup>. Relations by Eberhart<sup>50</sup> provide an estimate  $1.45 \times 10^3 \leq \gamma \leq 2.86 \times 10^3$  dyne cm<sup>-1</sup>.

For a whisker of circular cross section the surface free energy per ferric ion is given by  $2\gamma/Zn$ , where  $Z$  is the radius and  $n$  is the number density of ferric ions in  $\alpha$ -Fe<sub>2</sub>O<sub>3</sub>,  $3.984 \times 10^{22}$  cm<sup>-3</sup>. Thus, the surface free energy per mole for a  $10^{-6}$  cm radius (200 Å diameter) is  $1.25 \times 10^{-13}$  erg/Fe<sup>+++</sup> (3.6 kcal/mole Fe<sub>2</sub>O<sub>3</sub>).

Lennard-Jones and Taylor<sup>57</sup> estimated  $5.66 \times 10^{-11}$  ergs/atom excess energy for atoms on an edge of MgO, from which one can calculate a value of  $4.7 \times 10^{-3}$  ergs/cm of edge. If an  $\alpha$ -Fe<sub>2</sub>O<sub>3</sub> whisker has, effectively, four edges at  $5 \times 10^{-3}$  ergs/cm, for  $Z = 10^{-6}$  cm, one calculates  $1.6 \times 10^{-13}$  ergs/Fe<sup>+++</sup>. This may or may not approximate the real value.

#### 1. Chemical Reaction

Values of  $\log p_{O_2}$  for the equilibrium  $C_2$ ,  $2 Fe_3O_4 (s) + 1/2 O_2(g) \rightleftharpoons 3 Fe_2O_3 (s)$ , are given in Table 2 of the text. Values of  $\Delta F$  for this reaction can be calculated for various oxygen pressures from the equation  $\Delta F = RT \ln p_{O_2}^{1/2}$ . For the reaction in dry air (oxygen pressure 0.2099 atm.),  $\Delta F$  is calculated to be -33.1 kcal/mole at 700°K (426.85°C), and -29.6 kcal/mole at 800°K (526.85°C).

If one considers that this free energy provides a driving force for all the iron in the Fe<sub>3</sub>O<sub>4</sub>, then the difference in chemical potential between the iron in the 2 Fe<sub>3</sub>O<sub>4</sub> and that in the 3 Fe<sub>2</sub>O<sub>3</sub> is  $\Delta F/6$  per g-atom.

Alternatively, one may apply the Gibbs-Duhem equation,  $N_1 du_1 + N_2 du_2 = 0$ . Letting the subscripts, 1 and 2, refer to iron and oxygen (atoms), respectively, and assuming the activity  $a_2 = p_{O_2}^{1/2}$ , we have  $du_1 = -\frac{N_2}{N_1} du_2 = -\frac{n_2}{n_1} RT d \ln p_{O_2}^{1/2}$ . The equilibrium  $C_2$  determines the value of  $p_{O_2}$  at the interface between  $\alpha$ -Fe<sub>2</sub>O<sub>3</sub> and Fe<sub>3</sub>O<sub>4</sub>. It follows that  $\Delta u = -(n_2/n_1) RT \Delta \ln p_{O_2}^{1/2} = -(3/2) \Delta F$ , where because  $\alpha$ -Fe<sub>2</sub>O<sub>3</sub> is nearly stoichiometric everywhere,  $(n_2/n_1) = (3/2)$ .

If negligible oxygen diffuses in, one in nine iron atoms diffuse out, according to the reaction ( $C_2$  rewritten)  $3 Fe_3O_4 (s) + \frac{3}{4} O_2 \rightleftharpoons 4 Fe_2O_3 + \frac{1}{2} Fe_2O_3$ , where  $\frac{1}{2} Fe_2O_3$  is in the whisker and the 4 Fe<sub>2</sub>O<sub>3</sub> take the place of the 3 Fe<sub>3</sub>O<sub>4</sub>. If no oxygen rearrangement occurs,

this latter may be  $\gamma\text{-Fe}_2\text{O}_3$  rather than  $\alpha\text{-Fe}_2\text{O}_3$ , giving a smaller free energy change for the reaction. If  $\alpha\text{-Fe}_2\text{O}_3$  is formed, assuming all of the free energy is available as a driving force for only the iron diffusing to the whisker (or platelet), we have  $3 \Delta F/2$ , where  $\Delta F$  refers to  $C_2$ . Note that this is the energy given by the Gibbs-Duhem equation. Values of  $3 \Delta F/2N$ , where  $N$  is Avogadro's number, are  $-34.5 \times 10^{-13}$  ergs/Fe at  $700^\circ\text{K}$  and  $-30.9 \times 10^{-13}$  ergs/Fe at  $800^\circ\text{K}$ .

Since the  $\text{Fe}_2\text{O}_3$  formed in the film presumably has relatively negligible surface free energy, the surface free energy, say possibly  $3 \times 10^{-13}$  ergs/ $\text{Fe}^{+++}$ , in the whisker, is to be subtracted from the driving force,  $34.5 \times 10^{-13}$  ergs/ $\text{Fe}^{+++}$ , whether it be available for nine iron atoms or for one. Unless the surface free energy has been grossly underestimated, the chemical reaction alone can supply the driving force for whisker growth, even for whiskers of 100 Å diameter ( $9 \times 10^{-13}$  ergs/ $\text{Fe}^{+++}$  surface free energy), at  $800^\circ\text{K}$ .

Since the volume occupied by the oxygen ions of the  $3 \text{Fe}_3\text{O}_4$  is smaller in the  $4 \text{Fe}_2\text{O}_3$  ( $\gamma$  or  $\alpha$ ), this volume change under pressure may provide energy,  $p\Delta V$ , in addition to the free energy of reaction. The volume of the unit cells of  $\text{Fe}_3\text{O}_4$ ,  $\alpha\text{-Fe}_2\text{O}_3$ , and  $\gamma\text{-Fe}_2\text{O}_3$ , in  $\text{\AA}^3$ , are 591.435, 301.198, and 579.84, respectively. The volumes 221.7%, 200.80, and 217.44  $\text{\AA}^3$  are, respectively, the volumes of these compounds with the oxygen of the original  $3 \text{Fe}_3\text{O}_4$ . Thus volume changes of 21.0 and 4.35  $\text{\AA}^3$  result in the reactions to produce  $\alpha\text{-Fe}_2\text{O}_3$  and  $\gamma\text{-Fe}_2\text{O}_3$ , respectively.

A lower limit for the critical shear stress of  $\alpha\text{-Fe}_2\text{O}_3$  given by Mackenzie and Birchenall,  $\sim 160 \text{ kg cm}^{-2}$ , or  $1.6 \times 10^8 \text{ dyne cm}^{-2}$ , is less than compressive strengths for some similar materials, and will serve as a "large" value for the pressure. The value of  $p\Delta V$  calculated is  $3.36 \times 10^{-15}$  ergs/ $\text{Fe}^{+++}$ , which is insignificant in comparison to the effect of the chemical reaction. Pressure of the order of  $10^{10} \text{ dyne cm}^{-2}$  (10 kb) could provide a significant effect. Stress concentration might result in such pressures in small regions.

If a flow under pressure results, as of a liquid, with a uniform pressure gradient along a length,  $l$ , of whisker, the force is  $P l^{-1} n^{-1}$ . If  $l \approx 1 \mu$ ,  $P = 1.5 \times 10^8$  dyne  $\text{cm}^{-2}$ , we have  $P l^{-1} n^{-1} = 4 \times 10^{-11}$  dyne/ $\text{Fe}^{+++}$ , a relatively small force.

## APPENDIX XIII

### Relationship Between the Fick's Law Diffusion Coefficient and the Mobility

Following Crank,<sup>59</sup> we write the flux of atoms of the  $i^{\text{th}}$  species,

$$J_i = - \frac{B_i n_i}{N} \frac{\partial \mu_i}{\partial x}, \quad (1)$$

where  $J_i$  is the number of atoms crossing one square centimeter per second, and  $B_i$  is the mobility, the proportionality constant which is the ratio of velocity to force, in  $\text{cm}^2 \text{ dyne}^{-1} \text{ sec}^{-1}$ . The other constants have the usual significance:  $N$  is Avogadro's number and  $n_i$  is the number density of atoms. The chemical potential,  $\mu_i$ , is written

$$\mu_i = \text{constant} + RT \log \gamma_i N_i, \quad (2)$$

where  $\gamma_i$  is the activity coefficient and  $N_i$  is the mole fraction. Substituting  $(\partial \mu_i / \partial x)$  obtained by differentiating the above equation, we have

$$J_i = - \frac{B_i n_i}{N} \cdot \frac{RT}{N_i} \frac{\partial N_i}{\partial x} \left( 1 + \frac{\partial \log \gamma_i}{\partial \log N_i} \right).$$

According to Crank,<sup>52</sup>  $\Sigma n_j$  is assumed constant. It follows then, from the equality,  $N_i = n_i / \Sigma n_j$ , that  $\frac{dN_i}{N_i} = \frac{dn_i}{n_i}$ .  $J$  is then given by

$$J_i = -D_i \frac{\partial n_i}{\partial x}, \quad (3)$$

Fick's law, where

$$D_i = kTB_i \left( 1 + \frac{\partial \ln \gamma_i}{\partial \ln n_i} \right) \quad (4)$$

Substituting for  $B_i$  from (1), we have

$$D_i = - \frac{RTJ}{n_i \frac{\partial \mu_i}{\partial x}} \left( 1 + \frac{\partial \ln \gamma_i}{\partial \ln n_i} \right) \quad (5)$$

#### APPENDIX XIV

##### Radial Diffusion Through the Wall of an Infinitely Long Right Circular Cylindrical Pipe with a Constant Free Energy Difference and Radial Growth - Whisker Growth

Putting the driving force, in terms of chemical potential,  $\mu$ , of the diffusion species, we would consider the case where

$$\mu_r = \text{constant, for } \rho = r, \text{ and}$$

$$\mu_Z = \text{constant, for } \rho = Z, \text{ where } \rho \text{ is the radius.}$$

Put

$$\Delta\mu = (\mu_Z - \mu_r) < 0.$$

Consider  $r$  and  $Z_0$  to be chosen arbitrarily so that  $r < Z_0$ . We would derive an equation for  $Z$  as a function of time for  $Z > Z_0$ . For  $J(\rho)$ ,  $\mu(\rho)$  functions of  $\rho$  and time,  $t$ , only, we have

$$J = - \frac{Bn}{N} \frac{d\mu}{d\rho} \quad (1)$$

where  $n$  is the number density of diffusing species, taken to be nearly constant,  $\rho$  is the radius in this consideration,  $B$  is the mobility, and the flux  $J$  has units compatible with the concentration units of  $c$ . We assume an instantaneous development of the steady state chemical potential distribution.

In order to provide for the conservation of matter we put

$$f(Z, \Delta\mu, r) = \rho J(\rho). \quad (2)$$

where  $f$  is independent of  $\rho$ . For arbitrary  $\Delta\mu$  and  $r$ ,  $f = f(Z)$ .

For any  $Z = r$ , substituting from (1) into (2), we have

$$f(Z) = - \frac{Bn}{N} \rho \frac{d\mu}{d\rho}.$$

Assuming  $B$  constant

$$f(Z) \int_r^\rho \frac{d\rho}{\rho} = - \frac{Bn}{N} \int_{\mu_r}^{\mu_\rho} d\mu.$$

Integrating, we have

$$f(Z) = - \frac{Bn (\mu_\rho - \mu_r)}{N \ln(\rho/r)}. \quad (3)$$

Note that

$$\frac{\frac{dZ}{dt}}{J(Z)} = \frac{1}{n}. \quad (4)$$

Substituting from (2) into (4), we have

$$\frac{dZ}{dt} = \frac{f(Z)}{Zn}.$$

Substituting from (3), for  $\rho = Z$ , we have the radial growth rate,

$$\frac{dZ}{dt} = - \frac{B \Delta \mu}{ZN \ln(\frac{Z}{r})}. \quad (5)$$

Putting  $x = \frac{Z}{r}$ ,  $x_0 = \frac{Z_0}{r}$ , and substituting in (5), we have,

$$r \left(\frac{Z}{r}\right) \ln\left(\frac{Z}{r}\right) r \frac{d(Z/r)}{dt} = - BN^{-1} \Delta \mu.$$

$$x \ln x \frac{dx}{dt} = - Br^{-2} N^{-1} \Delta \mu.$$



Putting  $k = -2 Br^{-2} N^{-1} \Delta\mu$ , and integrating, we have

$$\int_{x_0}^x u \ln u \, du = -\frac{k}{2} \int_{t_0}^t dv .$$

Integrating, we have

$$\frac{x^2}{2} (\ln x - 1/2) - \frac{x_0^2}{2} (\ln x_0 - 1/2) = -\frac{k}{2} (t - t_0) . \quad (6)$$

For the case of iron diffusion in a ferric oxide whisker, we can substitute for  $\Delta\mu$ , from Appendix XII,  $\Delta\mu_1 = -(3/2) RT \Delta \ln p_{O_2}^{1/2}$ . Assuming  $\frac{\partial \ln \gamma_1}{\partial \ln n_1} = 0$ , we have, from Appendix XIII,  $B_1 = D_1/kT$ . We have assumed in the derivation that  $B_1$  and  $D_1$  are constant-- i.e., independent of  $a_1$  and  $a_2$ . Substituting for  $\Delta\mu$  and  $B_1$  from the above equations, we have  $k = D_1 r^{-2} (3/2) \Delta \ln p_{O_2}$ . Substituting into (6), we have

$$t - t_0 = \frac{2 r^2 [x^2 (\ln x - \frac{1}{2}) - x_0^2 (\ln x_0 - \frac{1}{2})]}{3 D_1 \Delta \ln p_{O_2}} . \quad (7)$$

## 11. REFERENCES

1. J. Bardolle and J. Bénard, *Mem. Sci. Rev. Met.* 49, 613 (1952).
2. E. Gulbransen, W. McMillan, and K. F. Andrew, *J. Metals* 200, 1027 (1954).
3. G. Pfefferkorn, *Naturwiss.* 40, 551 (1953); *Z. Metallkunde* 46, 204 (1955).
4. R. Takagi, *J. Phys. Soc. Japan* 12, 1212 (1957).
5. E. A. Gulbransen and T. P. Copan, *Faraday Society Discussions* 28, 229 (1959).
6. M. Hansen, *Constitution of Binary Alloys*, 2nd Ed., McGraw-Hill Book Company, Inc., New York (1958).
7. *JANAF Thermochemical Tables*, The Dow Chemical Company, Midland, Michigan, Wustite ( $\text{FeO}_{0.947}\text{O}$ ), Magnetite ( $\text{Fe}_3\text{O}_4$ ), Hematite ( $\text{Fe}_2\text{O}_3$ ) (June 30, 1965); Water ( $\text{H}_2\text{O}$ ) (March 31, 1961).
8. R. Phelps, E. A. Gulbransen, and J. Hickman, *Anal. Chem.* 18, 391 (1946).
9. J. Bénard, *Oxydation des Métaux*, Gauthier-Villars, Paris (1962).
10. E. Gulbransen and K. Andrew, *J. Electrochem. Soc.* 106, 551 (1959).
11. R. F. Mehl and E. L. McCandless, *Trans. A.I.M.E.* 125, 531 (1937).
12. E. A. Gulbransen and R. J. Ruka, *Industrial and Engineering Chemistry* 43, 697 (1951).
13. E. A. Gulbransen, Chapter in Book, *Advances in Catalysis*, Vol. V, Academic Press, New York, pp. 119-175 (1953).
14. E. A. Gulbransen and T. P. Copan, Chapter in Book, *Physical Metallurgy of Stress Corrosion Fracture*, Edited by T. Rhodin, Interscience Publishers, New York (1959), p. 155.
15. A.J.C. Wilson, *Research Supplement* 2-11, 541 (1949).

16. F. C. Frank, Research Supplement 2-11, 542 (1949).
17. A.J.C. Wilson, Acta Cryst. 5, 318 (1952).
18. J. D. Eshelby, Phil. Mag. 3, 440 (1958).
19. J. Friedel, Dislocations, Pergamon Press, New York (1964), p. 22.
20. A. H. Cottrell, Theory of Crystal Dislocations, Gordon and Breach, New York (1964), p. 56-57.
21. J. Weertman and J. Weertman, Elementary Dislocation Theory, The Macmillan Company, New York (1964).
22. S. Miyake, Inst. of Phys. and Chem. Res. (Japan) 31, 161 (1937).
23. J. Bigot, Mem. Sci. Rev. Met. 60, 5 (1963).
24. S. Talbot and J. Bigot, Mem. Sci. Rev. Met. 62, 261 (1965).
25. ASTM X-ray Powder Data File, Card 13-534 (1964), Aravindakshan and Ali.
26. C. Palache, H. Berman, and C. Frondel, The System of Mineralogy, Seventh Edition, Vol. I, John Wiley and Sons, Inc., New York, 519-534 (1944).
27. R.F.W. Pease and R. A. Ploc, Trans. Met. Soc. A.I.M.E. 233, 1949 (1965).
28. W. C. Hagel, Trans. Met. Soc. A.I.M.E. 236, 179 (1966).
29. R. Lindner, Arkiv Kemi 4, 381 (1952).
30. R. L. Coble, J. Am. Ceram. Soc. 41, 55 (1958).
31. K. Compaan and Y. Haven, Trans. Faraday Soc. 52, 786 (1956).
32. K. Hauffe, Oxidation of Metals, Plenum Press, New York (1965).
33. P. Grieveson and E. T. Turkdogan, J. of Metals 16, 123 (1964).
34. O. N. Salmon, J. Am. Chem. Soc. 65, 550 (1961).
35. U. R. Evans and J. Stockdale, J. Chem. Soc. 1929, 2651 (1929).
36. L. Pauling and S. B. Hendricks, J. Am. Chem. Soc. 47, 781 (1925).

37. International Tables for X-ray Crystallography, The Kynoch Press, Birmingham, England, Vol. I (1952), No. 167.
38. R. L. Blake and R. E. Hessevick, T. Zoltai and L. W. Finger, Am. Mineralogist 51, 123 (1966).
39. B.T.M. Willis and H. P. Rooksby, Proc. Phys. Soc. B65, 950 (1952).
40. T. Takada and N. Kawai, J. Phys. Soc. Japan 17, B-I, 691 (1962).
41. L. Neel, J. Phys. Soc. Japan 17, B-I, 676 (1962).
42. G. Shirane, S. J. Pickart, R. Nathans, and Y. Ishikawa, J. Phys. Chem. Solids 10, 35 (1959).
43. M. L. Kronberg, Acta Metallurgica 5, 507 (1957).
44. International Tables for X-ray Crystallography, The Kynoch Press, Birmingham, England, Vol. II (1959).
45. C. S. Barrett, Structure of Metals, 2nd Ed., McGraw-Hill Book Company, Inc., New York (1952), p. 11.
46. ASTM X-ray Powder Data File, Card 11-661.
47. W. B. Pearson, A Handbook of Lattice Spacings and Structures of Metals and Alloys, Pergamon Press, New York (1958).
48. E. H. Mann, Proc. Royal Soc. London V. A199, 376 (1949).
49. J. D. Eshelby, J. Appl. Phys. 24, 176 (1953).
50. J. D. Eshelby, Physica Status Solidi 2, 1021 (1962).
51. F. C. Frank, Acta Cryst. 4, 497 (1951).
52. H. B. Huntington, in Solid State Physics 7, F. Seitz and D. Turnbull, Eds., Academic Press, Inc., New York, 213 (1958).
53. J. F. Nye, Physical Properties of Crystals, Oxford, London (1960).
54. A.L.G. Rees and J. A. Spink, Acta Cryst. 3, 316 (1950).
55. J. Gjønnes, Acta Cryst. 15, 1045 (1962).
56. J. G. Eberhart, Trans. Met. Soc. A.I.M.E. 236, 1362 (1966).

- 57. J. E. Lennard-Jones and P. A. Taylor, Proc. Roy. Soc. A, 109, 476 (1925).
- 58. J. D. Mackenzie and C. E. Birchenall, Corrosion 13, 783 (1957).
- 59. J. Crank, Faraday Soc. Disc. 23, 99 (1957).

UNCLASSIFIED

Security Classification

DOCUMENT CONTROL DATA - R&D		
(Security classification of title, body of abstract and indexing annotation must be entered when the overall report is classified)		
1 ORIGINATING ACTIVITY (Corporate author) Westinghouse Research Laboratories Pittsburgh, Pennsylvania 15235		2a REPORT SECURITY CLASSIFICATION Unclassified
		2b GROUP
3 REPORT TITLE  CHEMICAL PHYSICS OF SURFACE REACTIONS OF METALS		
4 DESCRIPTIVE NOTES (Type of report and inclusive dates) Final Report - June 1, 1965 to May 31, 1967		
5 AUTHOR(S) (Last name, first name, initial) Gulbransen, Earl A. and Tallman, Richard L.		
6 REPORT DATE May 31, 1967	7a TOTAL NO OF PAGES 116	7b NO OF REFS 59
8a CONTRACT OR GRANT NO. Nonr-4949(00)	9a ORIGINATOR'S REPORT NUMBER(S)  67-9B6-SURFC-R1	
b. PROJECT NO. NR-036-0641	9b OTHER REPORT NO(S) (Any other numbers that may be assigned this report)	
c.		
d.		
10 AVAILABILITY/LIMITATION NOTICES		
11 SUPPLEMENTARY NOTES		12 SPONSORING MILITARY ACTIVITY Office of Naval Research Material Sciences Division Washington, D. C. 20360
13 ABSTRACT <p>A survey is made of studies at the Westinghouse Research Laboratories on the structure of oxide films and the formation of localized oxide growths on iron. Filamentary whisker growths are formed when iron is oxidized in dry oxygen at 400° to 500°C. Long, blade-like platelets are formed at 450°C in atmospheres containing both water vapor and a trace of oxygen.</p> <p>The oxide whiskers and the blade-like platelets produce fiber-texture patterns showing exclusively <math>\alpha</math>-Fe<sub>2</sub>O<sub>3</sub> diffraction and a [1120] fiber axis. Selected-area electron diffraction patterns of individual growths show the same fiber axis and indicate (1) that the most simple whiskers have a single axial screw dislocation and (2) that the blades are twinned on the blade-face plane, (1101).</p> <p>Growth mechanisms based on easy paths for diffusion along the axial dislocation in the oxide whisker and along the twin plane in the oxide blade-like platelet are proposed. Some calculations relevant to the internal diffusion mechanism in whiskers are presented.</p>		

DD FORM 1473

UNCLASSIFIED

Security Classification

RM 34034

14 KEY WORDS	LINK A		LINK B		LINK C	
	ROLE	WT	ROLE	WT	ROLE	WT
Iron Oxidation Crystal growth Blades Platelets Whiskers Twinning Corrosion Electron diffraction Electron microscopy Transport Diffusion Hematite Ferric oxide Mechanism						

**INSTRUCTIONS**

**1. ORIGINATING ACTIVITY.** Enter the name and address of the contractor, subcontractor, grantee, Department of Defense activity or other organization (corporate author) issuing the report.

**2a. REPORT SECURITY CLASSIFICATION.** Enter the overall security classification of the report. Indicate whether "Restricted Data" is included. Marking is to be in accordance with appropriate security regulations.

**2b. GROUP.** Automatic downgrading is specified in DoD Directive 5200.10 and Armed Forces Industrial Manual. Enter the group number. Also, when applicable, show that optional markings have been used for Group 3 and Group 4 as authorized.

**3. REPORT TITLE.** Enter the complete report title in all capital letters. Titles in all cases should be unclassified. If a meaningful title cannot be selected without classification, show title classification in all capitals in parentheses immediately following the title.

**4. DESCRIPTIVE NOTES.** If appropriate, enter the type of report, e.g., interim, progress, summary, annual, or final. Give the inclusive dates when a specific reporting period is covered.

**5. AUTHOR(S).** Enter the name(s) of author(s) as shown on or in the report. Enter last name, first name, middle initial. If military, show rank and branch of service. The name of the principal author is an absolute minimum requirement.

**6. REPORT DATE.** Enter the date of the report as day, month, year, or month, year. If more than one date appears on the report, use date of publication.

**7. TOTAL NUMBER OF PAGES.** The total page count should follow normal pagination procedures. i.e., enter the number of pages containing information.

**7a. NUMBER OF REFERENCES.** Enter the total number of references cited in the report.

**8a. CONTRACT OR GRANT NUMBER.** If appropriate, enter the applicable number of the contract or grant under which the report was written.

**8b, 4, & 6. PROJECT NUMBER.** Enter the appropriate military department identification, such as project number, subproject number, system numbers, test numbers, etc.

**9a. ORIGINATOR'S REPORT NUMBER(S).** Enter the official report number by which the document will be identified and controlled by the originating activity. This number must be unique to this report.

**9b. OTHER REPORT NUMBER(S).** If the report has been assigned any other report numbers, either by the originator or by the sponsor, also enter this number(s).

**10. AVAILABILITY LIMITATION NOTICES.** Enter any limitations on further dissemination of the report other than those imposed by security classification, using standard statements such as:

- (1) "Qualified requesters may obtain copies of this report from DDC."
- (2) "Foreign announcement and dissemination of this report by DDC is not authorized."
- (3) "U. S. Government agencies may obtain copies of this report directly from DDC. Other qualified DDC users shall request through \_\_\_\_\_."
- (4) "U. S. military agencies may obtain copies of this report directly from DDC. Other qualified users shall request through \_\_\_\_\_."
- (5) "All distribution of this report is controlled. Qualified DDC users shall request through \_\_\_\_\_."

If the report has been furnished to the Office of Technical Services, Department of Commerce, for sale to the public, indicate this fact and enter the price, if known.

**11. SUPPLEMENTARY NOTES.** Use for additional explanatory notes.

**12. SPONSORING MILITARY ACTIVITY.** Enter the name of the departmental project office or laboratory sponsoring (paying for) the research and development. Include address.

**13. ABSTRACT.** Enter an abstract giving a brief and factual summary of the document indicative of the report even though it may also appear elsewhere in the body of the technical report. If additional space is required, a continuation sheet shall be attached.

It is highly desirable that the abstract of classified reports be unclassified. Each paragraph of the abstract shall end with an indication of the military security classification of the information in the paragraph, representative as follows:

There is no limitation on the length of the abstract. However, the suggested length is from 150 to 225 words.

**14. KEY WORDS.** Key words are technically meaningful terms or short phrases that characterize a report and may be used as index entries for cataloging the report. Key words must be selected so that no security classification is required. Identifiers, such as equipment model designation, code name, location, project code name, geographic location, may be used as key words but will be followed by an indication of the security level. The assignment of key words is optional for unclassified reports.